Physics-based monitoring of subsurface processes using seismic ambient noise

Evert Barend Fokker

Utrecht Studies in Earth Sciences
No. 302

Members of the dissertation committee:

Prof. dr. Andrew Curtis
University of Edinburgh, Grant Institute – Edinburgh, United Kingdom

Prof. dr. Läslo Evers
Delft University of Technology – Delft, The Netherlands
Royal Netherlands Meteorological Institute – De Bilt, The Netherlands

Prof. dr. Laura Socco
Politecnico di Torino – Turin, Italy

Prof. dr. Jan Diederik van Wees
Utrecht University – Utrecht, The Netherlands
TNO Geological Survey of the Netherlands – Utrecht, The Netherlands

Prof. dr. Ulrich Wegler
Friedrich Schiller University Jena – Jena, Germany

ISBN: 978-90-6266-675-1
DOI: 10.33540/2171

Cover illustration: Four-dimensional visualization of the inferred pore pressure variations in the shallow subsurface of Groningen (Chapter 3, Figure 3.8c).

Physics-based monitoring of subsurface processes using seismic ambient noise

Op natuurkunde gebaseerde monitoring van ondergrondse processen gebruikmakend van seismische achtergrondruis

(met een samenvatting in het Nederlands)

Proefschrift

ter verkrijging van de graad van doctor aan de Universiteit Utrecht op gezag van de rector magnificus prof. dr. H.R.B.M. Kummeling, ingevolge het besluit van het college voor promoties in het openbaar te verdedigen op vrijdag 26 april 2024 des middags te 2.15 uur

door

Evert Barend Fokker

geboren op 20 november 1994
te Nieuwegein, Nederland

Promotor:
Prof. dr. Jeannot Trampert

Copromotor:
Dr. ir. Elmer Ruigrok

The research in this thesis is part of research programme DeepNL, financed by the Netherlands Organisation for Scientific Research (NWO) under project number DeepNL.2018.33.

Aan Janine

Sol Iustitiae Illustra Nos – May the Sun of Righteousness Enlighten Us
– Utrecht University motto after Malachi 4.2, Bible

Contents

Summary

Understanding subsurface processes is essential for resource management, hazard mitigation, and environmental protection. Passive seismic methods using ambient seismic noise have emerged as a promising tool for subsurface monitoring and imaging. These methods offer non-invasive, large-scale, and continuous measurements, providing valuable insights into geological structures, geophysical properties, and subsurface processes. However, these methods are often based on empirical relationships between seismic velocity variations and dynamic subsurface properties, and the physical mechanisms underlying these relationships have not yet been fully exploited.

This doctoral research contributes to advancing the understanding of seismic velocity changes and leverages this knowledge to enhance the monitoring of subsurface dynamics. It addresses the physical mechanisms behind seismic velocity variations, offering a fundamental understanding that goes beyond empirical relationships. Physics-based approaches allow for more accurate and comprehensive interpretations, predictive modeling, and technological advancements in subsurface monitoring and imaging.

The research begins by constructing a physics-based model that connects seismic velocity changes to variations in pore pressure and vertical stress, related to fluctuations in groundwater level. The model utilizes established relationships between seismic velocities and induced stress, coupled with wave propagation theory, basic hydrology and geomechanics, to establish direct links between seismic velocity variations and specific dynamic subsurface properties, namely fluctuations in pore pressure and vertical compressional stress. For pore pressure fluctuations, the model's validity is confirmed using passive image interferometry on seismic ambient noise data from Groningen, the Netherlands, demonstrating its ability to explain surface-wave phase-velocity variations caused by pore pressure fluctuations.

The direct link between seismic velocity variations and pore pressure is subsequently exploited for four-dimensional space-time pore pressure monitoring using surface-wave phase-velocity changes. As such, I introduce pore pressure sensitivity kernels as a direct connection between depth-dependent pore pressure variations and frequency-dependent changes in surface-wave phase velocities, showcasing their utility in inferring pore pressure variations in the Groningen subsurface. The inferred pore pressure models align closely with independent pressure head measurements, highlighting the potential for quantitative pore pressure inferences. The sensitivity of surface-wave phase velocities to pore pressure changes was found to decrease much faster with depth than the sensitivity to changes in elastic parameters, limiting the monitoring approach in the Groningen subsurface to the shallowest 200 m for natural pore pressure variations.

In contrast, pore pressure variations caused by human activities are significantly larger. Therefore, this research continues with a feasibility assessment of utilizing surface-wave phase-velocity changes to monitor anthropogenic pore pressure developments in deeper reservoirs, particularly in the Harlingen and Groningen gas reservoirs. It expands pore pressure sensitivity kernels to deeper depths and models surface-wave phase-velocity changes in response to hypothetical production scenarios. While monitoring the shallow (~ 1 km) Harlingen reservoir appears feasible, monitoring the deeper (~ 3 km) Groningen reservoir presents substantial challenges, as the existing measurement uncertainties for velocity changes must be significantly reduced.

Finally, the research delves into the physics of temperature-induced seismic velocity changes in the shallow unconsolidated subsurface. It reconciles field and laboratory experiments by considering intrinsic temperature dependencies, thermally induced stress, and thermally induced strain. The study predicts seasonal temperature-induced seismic velocity variations and their implications for site amplification. The site-specific material properties determine whether site amplification is more pronounced during summer or winter.

Overall, this research enhances our understanding of seismic velocity changes and benefits their utility in subsurface monitoring, thereby contributing to resource management, hazard assessment, and a sustainable environment. The physics-based approach facilitates a more comprehensive understanding of subsurface dynamics and supports the development of innovative monitoring and imaging techniques.

Samenvatting

Het begrijpen van processen in de ondergrond is van essentieel belang voor de winning en het beheer van grondstoffen, de beperking van gevaren en de bescherming van het milieu. Passieve seismische methoden die gebruik maken van achtergrondruis zijn veelbelovend voor monitoring en beeldvorming van de ondergrond. Deze methoden bieden de mogelijkheid van niet-invasieve en continue metingen, en kunnen waardevolle inzichten opleveren in geologische structuren, geofysische eigenschappen en ondergrondse processen. Meestal zijn deze methoden echter gebaseerd op empirische relaties tussen seismische snelheden en dynamische eigenschappen van de ondergrond. De fysische mechanismen die aan deze relaties ten grondslag liggen zijn nog niet volledig begrepen en benut.

Dit proefschrift draagt bij aan de kennis van de natuurkunde achter seismische snelheidsveranderingen en gebruikt deze bij het monitoren van fysische processen in de ondergrond. Het behandelt fysische mechanismen achter seismische snelheidsveranderingen en biedt een fundamenteel begrip dat empirische relaties overstijgt. De op natuurkunde gebaseerde aanpak maakt nauwkeurigere en uitgebreidere interpretaties mogelijk, en voorspellende modellen en technologische ontwikkeling op het gebied van ondergrondse monitoring en beeldvorming.

Het onderzoek begint met de ontwikkeling van een model dat veranderingen in seismische snelheid koppelt aan variaties in poriëndruk en verticale spanning door veranderingen in de grondwaterspiegel. Het model is gebaseerd op reeds bekende relaties tussen seismische snelheden en spanningen, in combinatie met golfvoortplantingstheorie, hydrologie en geomechanica. Dit resulteert in directe verbanden tussen de seismische snelheid en specifieke dynamische eigenschappen van de ondergrond, namelijk poriëndruk en verticale spanning. Het model is voor fluctuaties in poriëndruk gevalideerd met metingen van seismische achtergrondruis in de provincie Groningen. Door hier herhaaldelijk seismische interferometrie op toe te passen en tijdsverschillen van aankomsten te detecteren zijn veranderingen in de voortplantingssnelheid van seismische golven gemeten. De snelheidsveranderingen van oppervlaktegolven kunnen in Groningen worden verklaard door fluctuaties in poriëndruk.

Het directe verband tussen poriëndruk en de seismische snelheid wordt hierna benut voor vierdimensionale monitoring van poriëndruk met behulp van oppervlaktegolven. Hiervoor introduceer ik poriëndrukgevoeligheidskernels als directe verbinding tussen diepteafhankelijke variaties in poriëndruk en frequentieafhankelijke veranderingen in fasesnelheden van oppervlaktegolven. Deze gevoeligheidskernels worden vervolgens gebruikt voor het afleiden van poriëndrukveranderingen in de Groningse ondergrond. De afgeleide poriëndrukmodellen komen goed overeen met onafhankelijke stijghoogtemetingen. Dit demonstreert het potentieel voor kwantitatieve afleidingen van poriëndruk. Het is opmerkelijk dat de

gevoeligheid van oppervlaktegolfsnelheden voor veranderingen in poriëndruk veel sneller afneemt met diepte dan de gevoeligheid voor veranderingen in elastische parameters. Daardoor is de methode alleen toepasbaar in de bovenste 200 m van de Groningse ondergrond voor natuurlijke variaties in poriëndruk.

Door de mens veroorzaakte veranderingen in poriëndruk kunnen echter vele malen groter zijn. Daarom gaat het onderzoek verder met een haalbaarheidsstudie voor het gebruik van oppervlaktegolven voor het monitoren van antropogene fluctuaties in poriëndruk in diepere reservoirs, specifiek in de Harlingen en Groningen gasreservoirs. Ik breid de poriëndrukgevoeligheidskernels uit naar grotere diepten en modelleer snelheidsveranderingen van oppervlaktegolven ten gevolge van realistische productiescenario's. Terwijl monitoring in het ondiepe (~ 1 km) Harlingen reservoir haalbaar lijkt, brengt monitoring in het diepere (~ 3 km) Groningen reservoir grote uitdagingen met zich mee, aangezien de bestaande meetonzekerheden voor snelheidsveranderingen aanzienlijk moeten worden verminderd.

Tot slot duik ik in dit onderzoek in de natuurkunde achter seismische snelheidsveranderingen gerelateerd aan temperatuurveranderingen in de ondiepe ondergrond van ongeconsolideerde sedimenten. Schijnbare tegenstrijdigheden tussen veld- en laboratoriumexperimenten worden verklaard door meerdere mechanismen te overwegen: intrinsieke temperatuurafhankelijkheden, thermisch geïnduceerde spanning en thermisch geïnduceerde vervorming. De studie voorspelt seizoensafhankelijke, door temperatuurschommelingen veroorzaakte seismische snelheidsveranderingen en kwantificeert hun uitwerking op het opslingereffect. De lokale materiaaleigenschappen van de ondiepe ondergrond bepalen of het opslingereffect groter is tijdens de zomer of tijdens de winter.

Dit onderzoek draagt bij aan het begrip van seismische snelheidsveranderingen en vergroot de bruikbaarheid van passieve seismische methoden bij het monitoren van ondergrondse processen. Op deze manier kan het een bijdrage leveren aan grondstofbeheer, gevaarbeperking en een duurzaam milieu. De op natuurkunde gebaseerde benadering leidt tot een nieuw begrip van ondergrondse dynamica en ondersteunt de ontwikkeling van innovatieve monitoring- en beeldvormingstechnieken.

1

Introduction

1

1.1. The Importance of Passive Subsurface Measurements

Understanding subsurface processes is of utmost importance for a safe living environment. The interior of the Earth holds valuable resources such as groundwater, geothermal energy and hydrocarbons. Knowledge of reservoir properties and subsurface dynamics is essential for efficient resource exploitation and environmental management. Furthermore, subsurface processes directly impact human safety via potential geological hazards manifested in earthquakes, landslides, and volcanic eruptions. By comprehending such processes, we can improve hazard forecasting and mitigation strategies, ultimately saving lives and minimizing economic losses.

However, directly measuring most relevant subsurface properties presents significant difficulties. Direct measurements are challenging due to the subsurface's relative inaccessibility, depth, and spatial heterogeneity. Traditional subsurface measurement techniques, involving drilling, can be expensive and time-consuming, and can only provide localized information. This makes it difficult to gain a comprehensive understanding of subsurface processes at larger scales. Moreover, these methods require physical alteration of the subsurface, which can be impractical or undesirable.

Active seismic surveys use controlled seismic sources, such as explosions or airguns, to image the subsurface. By recording and analyzing the reflections of seismic waves propagating through the medium, one can assess the subsurface without drilling (e.g., Angelov, 2009; Landrø & Stammeijer, 2004). Active seismic surveys have been successful especially in providing insights into geological structures and hydrocarbon reservoirs. However, these surveys require significant planning, resources, and logistical arrangements, they can be disruptive to the environment (e.g., Nowacek et al., 2015) and they are often limited by safety regulations in densely populated areas.

Passive seismic methods (e.g., Clarke et al., 2011; Curtis et al., 2006; James et al., 2017; Lobkis & Weaver, 2003; Mao et al., 2020; Mikesell et al., 2015; Snieder et al., 2002; Stehly et al., 2008; Wapenaar et al., 2010a) have emerged as a promising solution to complement active seismic surveys (e.g., Maxwell & Urbancic, 2005). Instead of active sources, they use the ambient seismic wave field, originating from sources as ocean waves and human activities (e.g., Brenguier et al., 2019; Cessaro, 1994; Díaz et al., 2017; Kimman et al., 2012; Lecocq et al., 2020; Nakata et al., 2011). By analysing the subtle variations in the seismic wave field over time, we can infer valuable information about geological structures (e.g., Brenguier et al., 2007; Mordret et al., 2013; Toledo et al., 2022), geophysical properties (e.g., Hofman et al., 2017; Martins et al., 2020; van Ginkel et al., 2020; Zhou & Paulssen, 2017, 2020), and subsurface processes (e.g., Bièvre et al., 2018; Brenguier et al., 2008a; Brenguier et al., 2008b; Colombero et al., 2018; James et al., 2019; Planès et al., 2017; Wegler et al., 2009; Wegler & Sens-Schönfelder, 2007; Zhou & Paulssen, 2022).

Passive seismic methods offer several advantages over active surveys. First, they are non-invasive and do not require artificial seismic sources. This reduces the

environmental impact drastically. Second, passive seismic methods enable large-scale continuous measurements over extended periods. This facilitates the detection of subtle variations in subsurface properties. Passive image interferometry (Sens-Schönfelder & Wegler, 2006) is such a technique to utilize passive seismic measurements. It allows us to estimate seismic velocity variations using recordings of seismic ambient noise. By studying seismic velocity variations, we can gain a deeper understanding of geological, hydrological, and geophysical processes, ultimately contributing to our understanding of natural hazards, and the sustainable management of subsurface resources.

1.2. Seismic Velocity Measurements as Indicators of Subsurface Processes

Seismic velocity variations enable us, amongst others, to monitor groundwater levels (e.g., Andajani et al., 2020; Clements & Denolle, 2023; Clements & Denolle, 2018; Mao et al., 2022; Roumelioti et al., 2020; Sens-Schönfelder & Wegler, 2006, 2011; Yang et al., 2018) and temperature variations (e.g., Colombero et al., 2018; Richter et al., 2014; Sánchez-Pastor et al., 2021; Sánchez-Pastor et al., 2019), examine tailing-dam stabilities (e.g., Olivier et al., 2017; Ouellet et al., 2022), study earthquake stress releases (e.g., Brenguier et al., 2008a; Madley et al., 2022; Minato et al., 2012; Wang et al., 2019; Wegler et al., 2009), investigate volcanic activity (e.g., Brenguier et al., 2011; Brenguier et al., 2008b; Duputel et al., 2009; Makus et al., 2023; Mordret et al., 2010; Obermann et al., 2013a; Olivier et al., 2019; Ratdomopurbo & Poupinet, 1995; Rivet et al., 2015; Sánchez-Pastor et al., 2018; Yates et al., 2019), track fluid migration over time (e.g., Illien et al., 2022; Li et al., 2022; Wang et al., 2021), monitor landslides (e.g., Bièvre et al., 2018; Hussain et al., 2019; Mainsant et al., 2012; Voisin et al., 2016) and analyse thawing of the permafrost (e.g., James et al., 2019; Lindner et al., 2021). However, most of the above mentioned studies are based on empirical relationships, and the physical mechanisms underlying these relationships have not yet been fully exploited.

One such relationship is the correlation between the seismic velocity and the groundwater level. By monitoring seismic velocity variations and correlating them with fluctuations in the groundwater level, we can study the dynamics of subsurface water storage and movement. However, such empirical relationships cannot be generalised, since some studies have found a positive correlation between groundwater fluctuations and velocity changes (Liu et al., 2020; Voisin et al., 2017), while others have found an anti-correlation (Clements & Denolle, 2018; Hillers et al., 2014; Nakata & Snieder, 2012; Sens-Schönfelder & Wegler, 2006; Tsai, 2011). Furthermore, without a physical theory, correlations cannot provide understanding on how seismic velocity changes are produced.

Similarly, seismic velocities have been found to correlate with temperature variations in the subsurface. Temperature influences the elastic properties of rocks, which, in turn, affect seismic velocities. Variations in subsurface temperature can arise due to various processes, including geothermal activity and seasonal changes.

By measuring seismic velocities and analyzing their relationship with temperature variations, we can infer information about geothermal resources and subsurface thermal processes. However, field and laboratory experiments have seemingly provided contradictory results. Most field studies have reported positive correlations between temperature and seismic velocities (e.g., Ermert et al., 2023; Lecocq et al., 2017; Richter et al., 2014; Sleeman & de Zeeuw-van Dalfsen, 2020), while most laboratory experiments have shown anti-correlations (e.g., Birch, 1943; Christensen, 1979; Jaya et al., 2010; Kern, 1978; Kohnen, 1974). Laboratory experiments have thus not yet captured the complicated field response of seismic velocities to temperature variations. Likely, not all mechanisms for temperature-induced velocity change have been considered together.

Despite the observed empirical relationships between seismic velocities and subsurface processes, a complete physical understanding of these relationships is still missing. While empirical correlations provide valuable insights and practical applications, they lack a detailed understanding of the underlying mechanisms. The complex interplay of various geophysical processes contributes to the observed correlations but requires further investigation for a comprehensive understanding.

1.3. Motivation

The purpose of my doctoral research is to gain a deeper understanding on the physics behind seismic velocity changes and their applications. The physical argument is crucial, as it provides a fundamental understanding of the underlying processes governing subsurface dynamics. Moreover, by unraveling the physical mechanisms driving seismic velocity variations, one can exploit seismic velocity measurements to their fullest extent and achieve quantitative inferences without relying on empirical relationships.

Quantitative inferences offer several advantages compared to empirical studies. First, they provide a deeper level of insight into subsurface processes, as empirical relationships often lack the ability to fully capture the underlying mechanisms. Second, by establishing a physics-based understanding, we can directly relate seismic velocity variations to specific subsurface properties and processes, leading to more accurate and comprehensive interpretations.

A physics-based approach also allows for the development of predictive models that can be used to simulate seismic velocity changes under different subsurface conditions. These models provide a powerful tool for exploring hypothetical scenarios.

Furthermore, a physics-based understanding of seismic velocity changes promotes technological advancements in data acquisition and processing. By leveraging the knowledge of underlying physical mechanisms, we can develop innovative measurement techniques and processing algorithms, opening up new possibilities for improved subsurface imaging and monitoring.

1.4. Outline

The objectives of this study cover multiple aspects of seismic velocity variations, including the acquisition and interpretation of passive seismic velocity measurements, as well as physics-based velocity modeling and the exploitation of velocity data. In this section, I provide an overview of the different chapters that contribute to the research objectives of this doctoral work.

Chapter 2 relates seismic velocity changes through effective stress to fluctuations in the pore pressure and vertical compressional stress. By combining the theoretical relation between induced stress and velocity change derived by Tromp and Trampert (2018) with wave propagation theory, basic hydrology and geomechanics, I develop a physics-based model for seismic velocity change. Using data collected in Groningen, the Netherlands, I validate this model, and show that it enables us to explain surface-wave phase-velocity variations by fluctuations in pore pressure. The derived relationships form the basis for physics-based pore pressure monitoring using passive image interferometry.

Chapter 3 shows that measured velocity changes can be inverted for pore pressure variations as a function of time and space. I introduce pore pressure sensitivity kernels for surface-wave phase-velocity changes, and compute velocity variations by applying passive image interferometry to seismic ambient noise measurements in Groningen, the Netherlands. An inversion of these velocity changes results in models of pore pressure variation as a function of time, depth and region. Different regions of Groningen show a different temporal behavior that coincide with the jurisdictions of two independent water boards and corresponds with existing piezometric measurements. Pore pressure sensitivity kernels were found to decrease rapidly with depth, limiting this approach to the depth range of 0-200 m for hydrological pore pressure variations.

Chapter 4 assesses the feasibility of using surface-wave phase-velocity changes for pore pressure monitoring in deeper reservoirs. I expand the pore pressure sensitivity kernels to include the depth range of the Harlingen and Groningen gas reservoirs, and develop forward models of surface-wave velocity variations for hypothetical production scenarios. For the Groningen reservoir, the pore pressure sensitivity decreased to the extent that the resulting surface-wave velocity changes lie within the range of measurement uncertainty. Pore pressure monitoring in the Groningen gas reservoir is therefore not feasible using surface-wave velocity changes. For the Harlingen reservoir, the modeled surface-wave velocity variations are larger than the measurement uncertainty. To assess the feasibility of pore pressure monitoring related to production, I perturb the forward model by shallow-origin velocity variations observed in Groningen, and invert for pore pressure variations in the gas reservoir. The decreasing pore pressure sensitivity with depth increases the uncertainties of the inferred pore pressure models to 0.2 MPa at the reservoir depth, which is nevertheless sufficiently small to be able to capture production-related pore pressure developments.

Chapter 5 explores the physics connecting temperature and seismic properties. To reconcile seemingly contradictory field and laboratory experiments, I ex-

amine three mechanisms for temperature-induced seismic velocity change: (1) the intrinsic temperature dependency of the elastic constants, (2) thermally induced stress, and (3) thermally induced strain. A series of physics-based models reveals that thermal strain is negligible, while the other mechanisms compete. I predict seasonal temperature-induced changes in body-wave velocities up to 8%, surface-wave phase-velocity variations of $1-2$%, and changes in site amplification of about 4%. The competition between the two dominant mechanisms for velocity change determines whether site amplification is more pronounced during summer or winter.

Throughout this study, I consider various physical properties and employ multiple mathematical definitions. To ensure clarity and for convenience, I present in the Glossary all the notations and mathematical symbols used in this study. Given the numerous parameters involved, it is important to note that symbols may differ from those used in the published articles upon which the chapters of this study are based.

2

Physics-Based Relationship for Pore Pressure and Vertical Stress Monitoring Using Seismic Velocity Variations

Abstract

Previous studies examining the relationship between the groundwater table and seismic velocities have been guided by empirical relationships only. Here, we develop a physics-based model relating fluctuations in groundwater table and pore pressure with seismic velocity variations through changes in effective stress. This model justifies the use of seismic velocity variations for monitoring of the pore pressure. Using a subset of the Groningen seismic network, near-surface velocity changes are estimated over a four-year period, using passive image interferometry. The same velocity changes are predicted by applying the newly derived theory to pressure-head recordings. It is demonstrated that the theory provides a close match of the observed seismic velocity changes.

The content of this chapter was published as: Fokker, E., Ruigrok, E., Hawkins, R., & Trampert, J. (2021). Physics-based relationship for pore pressure and vertical stress monitoring using seismic velocity variations. *Remote Sensing*, *13*(14), 2684.

2.1. Introduction

Seismic waves contain information about the subsurface; for instance, subsurface seismic properties such as shear modulus and density can be derived from observations of wave propagation. In Earth sciences, seismic data are therefore an important source of information. Relevant physical and chemical information can be found in seismic properties and especially in their variations. We distinguish two types of variations: spatial and time-lapse ones. Spatial variations in seismic velocity can indicate layer boundaries, faults or more subtle subsurface heterogeneity (e.g., Rawlinson et al., 2014). Time-lapse variations in seismic velocity can be caused by changes in stress, temperature or composition.

A technique to retrieve time-lapse velocity variations is passive image interferometry (Sens-Schönfelder & Wegler, 2006). This technique consists of two steps. First, the Green's function is estimated using cross-correlations of seismic noise recorded at two receivers. Secondly, the cross-correlation result using, e.g., a day's worth of data, is compared with a reference Green's function to obtain the relative change in seismic velocity. This technique has been applied to find volcanic precursors (Brenguier et al., 2008b), to monitor stress changes (Wegler et al., 2009), ensure the safety of civil structures (Salvermoser et al., 2015), and to monitor groundwater tables (Voisin et al., 2017).

A groundwater table is the depth in the subsurface where the soil or rock is fully saturated with water. It is the border between the unsaturated upper part (vadose zone) and the lower phreatic zone. Over the seasons, the soil moisture in the vadose zone varies due to precipitation and evaporation. At the same time, the groundwater table fluctuates due to drainage and inundation. Changes in both zones affect the loading and pore pressure of the deeper subsurface. Locally, the pore pressure at depth can be measured with a piezometric well. For measurement over a larger region and depth range, recent developments in seismic methods are promising.

In many monitoring studies, the seismic velocity change is empirically linked to other observations, for which the velocity change is used as a measurement. For instance, Clements and Denolle (2018) fitted seismic velocity changes linearly to changes in the groundwater table. This is also the case for other groundwater and pore pressure monitoring studies (Andajani et al., 2020; Clements & Denolle, 2018; Liu et al., 2020; Nakata & Snieder, 2012; Rivet et al., 2015; Sens-Schönfelder & Wegler, 2006; Voisin et al., 2017; Wang et al., 2017). An empirical relationship between seismic velocity and the groundwater table or pore pressure can be useful, but without theory it cannot provide understanding on how seismic velocity changes are caused.

The Groningen region in the Netherlands has been a test bed for monitoring studies, both due to presence of a large seismic network (Dost et al., 2017) and pronounced changes in the subsurface due to gas extraction (van Eijs & van der Wal, 2017) and a thick layer of unconsolidated sediments (van Ginkel et al., 2020). The large azimuthal coverage of the network was used to test different quality parameters for passive image interferometry (Fokker & Ruigrok, 2019). Moreover, seismic interferometry was applied to a string of geophones in the reservoir to measure compaction (Zhou & Paulssen, 2020). In another study, a dense surface network of

stations was used to detect velocity changes in refracted waves over a one-month period (Brenguier et al., 2020). Using the same dense array of 417 stations, a novel implementation of passive image interferometry was tested (Mordret et al., 2020). Following heavy rain, they found a velocity reduction that propagates downward with time. This they explained with effective-pressure diffusion.

This study provides a physics-based model connecting fluctuations in the pore pres-sure and vertical compressional stress to seismic velocity variations through changes in effective stress. We combine the relationship between induced stress and velocity change, derived from first principles byT Tromp and Trampert (2018), with wave propagation theory, basic hydrology and geomechanics to relate velocity change directly to fluctuations in the pore pressure and vertical compressional stress. Using data collected in Groningen, the Netherlands, we validate this relationship, and show that it enables us to monitor near surface (i.e., top 500 m) changes in pore pressure using passive image interferometry.

2.2. Theory

We derive a physics-based relationship between shear-wave velocity change and fluctuations in the groundwater table and pore pressure. First, we rewrite the existing relationship between seismic velocity and induced stress by Tromp and Trampert (2018). Then, we use basic hydrology and geomechanics to model the induced stress. Last, we study the relative contribution of different terms in the final equation. A similar derivation for compressional-wave velocity change can be found in Appendix 2.A.

2.2.1. Velocity Change Due to Induced Stress

Relationships between seismic velocity and induced stress were derived from first principles by Tromp and Trampert (2018, Equation 38). They showed that for an induced stress $d\boldsymbol{\sigma}$ (defined negative for compression), written in terms of an induced pressure $dp = -\frac{1}{3}tr(d\boldsymbol{\sigma})$ and a symmetric trace-free induced deviatoric stress $d\boldsymbol{\tau} = d\boldsymbol{\sigma} - \frac{1}{3}tr(d\boldsymbol{\sigma})\boldsymbol{I}$, the shear-wave velocity can be written as

$$\begin{aligned}\rho\tilde{v}_s^2 = \left(\mu + \mu'_p dp\right) \quad &+ \quad \frac{1}{2}\left(1-\mu'_p\right)\hat{\boldsymbol{k}}\cdot d\boldsymbol{\tau}\cdot\hat{\boldsymbol{k}} \\ &- \quad \frac{1}{2}\left(1+\mu'_p\right)\hat{\boldsymbol{a}}\cdot d\boldsymbol{\tau}\cdot\hat{\boldsymbol{a}},\end{aligned} \tag{2.1}$$

with mass density ρ, shear-wave velocity $v_s = \sqrt{\mu/\rho}$ without induced stress, its perturbation $dv_s = \tilde{v}_s - v_s$ due to induced stress, shear modulus μ, its pressure derivative $\mu'_p = \partial\mu/\partial p$, direction of propagation $\hat{\boldsymbol{k}}$, and direction of motion $\hat{\boldsymbol{a}}$. We rewrite this equation to find relative velocity change dv_s/v_s by subtracting $\mu = \rho v_s^2$ from both sides of the equation,

$$\rho\left((v_s+dv_s)^2-v_s^2\right)=\mu'_p dp \quad + \quad \frac{1}{2}\left(1-\mu'_p\right)\hat{\boldsymbol{k}}\cdot d\boldsymbol{\tau}\cdot\hat{\boldsymbol{k}} \quad - \quad \frac{1}{2}\left(1+\mu'_p\right)\hat{\boldsymbol{a}}\cdot d\boldsymbol{\tau}\cdot\hat{\boldsymbol{a}}, \tag{2.2}$$

and dividing by μ:

$$\frac{dv_s}{v_s}\left(2+\frac{dv_s}{v_s}\right)=\frac{\mu'_p dp}{\mu} \quad + \quad \frac{1-\mu'_p}{2\mu}\hat{\boldsymbol{k}}\cdot d\boldsymbol{\tau}\cdot\hat{\boldsymbol{k}} \quad - \quad \frac{1+\mu'_p}{2\mu}\hat{\boldsymbol{a}}\cdot d\boldsymbol{\tau}\cdot\hat{\boldsymbol{a}}. \tag{2.3}$$

Since velocity changes are usually small $\left(\left|\frac{dv_s}{v_s}\right| \ll 2\right)$, this relationship can be approximated as

$$\frac{dv_s}{v_s}=\frac{\mu'_p dp}{2\mu}+\frac{1-\mu'_p}{4\mu}\hat{\boldsymbol{k}}\cdot d\boldsymbol{\tau}\cdot\hat{\boldsymbol{k}}-\frac{1+\mu'_p}{4\mu}\hat{\boldsymbol{a}}\cdot d\boldsymbol{\tau}\cdot\hat{\boldsymbol{a}}. \tag{2.4}$$

2.2.2. Velocity Change Due to Surface Load and Pore Pressure

Wherever pore pressure plays a role, poroelastic theory states that deformation is proportional to the effective stress, defined by $\tilde{\boldsymbol{\sigma}}=\boldsymbol{\sigma}+\alpha_B u\boldsymbol{I}$ (Fjær et al., 2008, p. 32), where α_B represents the Biot constant and u is the pore pressure. The solid framework carries the part $\tilde{\boldsymbol{\sigma}}$ of the total external stress $\boldsymbol{\sigma}$, while the remaining part, $\alpha_B u$, is carried by the fluid. An increase in pore pressure essentially reduces the forces on the contact surfaces between the grains (i.e., $\tilde{\boldsymbol{\sigma}}$ becomes less negative, since (effective) stress is defined negative for compression). The remaining pore pressure, $(1-\alpha_B)\,u$, is counteracted by internal stresses in the solid. In unconsolidated or weak material, α_B is close to 1. We therefore need to formulate Equations 2.1–2.4 in terms of the effective stresses and the pore pressures that affect them.

We examine changes in effective stress that are induced by (near) surface processes such as fluctuation of the groundwater table or the atmospheric pressure. Such processes cause almost instant changes in the stress, while pore pressure diffusion is highly dependent on the permeability of the layers and viscosity of water. Therefore, we assume induced stress $d\boldsymbol{\sigma}(t)$ from surface processes to be independent of depth, while we allow induced pore pressure $du(z,t)$ to vary with depth. In a one-dimensional model, this automatically satisfies the zero divergence condition $\nabla\cdot d\boldsymbol{\sigma}=0$. For the loading effect, we only consider changes in vertical stress $d\sigma_{zz}(t)$.

We write the induced effective stress as

$$d\tilde{\boldsymbol{\sigma}}=d\boldsymbol{\sigma}+du\boldsymbol{I}=\begin{pmatrix} du & 0 & 0\\ 0 & du & 0\\ 0 & 0 & du+d\sigma_{zz}\end{pmatrix}, \tag{2.5}$$

with corresponding induced effective pressure

$$d\tilde{p} = -\frac{1}{3} tr\,(d\tilde{\boldsymbol{\sigma}}) = -du - \frac{1}{3} d\sigma_{zz}, \tag{2.6}$$

and induced effective deviatoric stress

$$d\tilde{\boldsymbol{\tau}} = d\tilde{\boldsymbol{\sigma}} - \frac{1}{3} tr\,(d\tilde{\boldsymbol{\sigma}})\,\boldsymbol{I} = -\frac{1}{3} d\sigma_{zz} \begin{pmatrix} 1 & 0 & 0 \\ 0 & 1 & 0 \\ 0 & 0 & -2 \end{pmatrix}. \tag{2.7}$$

We combine Equations 2.4, 2.6 and 2.7 to write the velocity change as

$$\begin{aligned} \frac{dv_s}{v_s} &= \frac{\mu'_p}{2\mu}\left(-du - \frac{1}{3} d\sigma_{zz}\right) \\ &- \frac{1}{3}\frac{1-\mu'_p}{4\mu} d\sigma_{zz}\left(\hat{k}_x^2 + \hat{k}_y^2 - 2\hat{k}_z^2\right) \\ &+ \frac{1}{3}\frac{1+\mu'_p}{4\mu} d\sigma_{zz}\left(\hat{a}_x^2 + \hat{a}_y^2 - 2\hat{a}_z^2\right). \end{aligned} \tag{2.8}$$

We distinguish three types of shear-waves: shear-waves with vertical propagation and horizontal motion ($\hat{k}_x = \hat{k}_y = 0$; $\hat{k}_z = 1$; $\hat{a}_x^2 + \hat{a}_y^2 = 1$; $\hat{a}_z = 0$), shear-waves with horizontal propagation and horizontal motion ($\hat{k}_x^2 + \hat{k}_y^2 = 1$; $\hat{k}_z = 0$; $\hat{a}_x^2 + \hat{a}_y^2 = 1$; $\hat{a}_z = 0$), and shear-waves with horizontal propagation and vertical motion ($\hat{k}_x^2 + \hat{k}_y^2 = 1$; $\hat{k}_z = 0$; $\hat{a}_x = \hat{a}_y = 0$; $\hat{a}_z = 1$). Respectively, this simplifies Equation 2.8 to

$$\left(\frac{dv_s}{v_s}\right)^{Vertical} = -\frac{\mu'_p}{2\mu} du - \frac{\mu'_p - 1}{4\mu} d\sigma_{zz}, \tag{2.9}$$

$$\left(\frac{dv_s}{v_s}\right)_{SH}^{Horizontal} = -\frac{\mu'_p}{2\mu} du, \tag{2.10}$$

and

$$\left(\frac{dv_s}{v_s}\right)_{SV}^{Horizontal} = -\frac{\mu'_p}{2\mu} du - \frac{\mu'_p + 1}{4\mu} d\sigma_{zz}. \tag{2.11}$$

2.3. Validation

To validate the relationships derived in the previous section, we model surface-wave velocity changes based on pressure-head measurements and compare their results to independent measurements obtained with passive image interferometry. From pressure-head measurements, recorded by piezometer *B08C0952* (Dinoloket, 2022) in Groningen, the Netherlands (Figure 2.1), we estimated changes in pore pressure and vertical stress, which are used as inputs to Equations 2.9-2.11 to model shear-wave velocity changes. Corresponding surface-wave velocity changes were then obtained through surface-wave dispersion modeling. To obtain independent

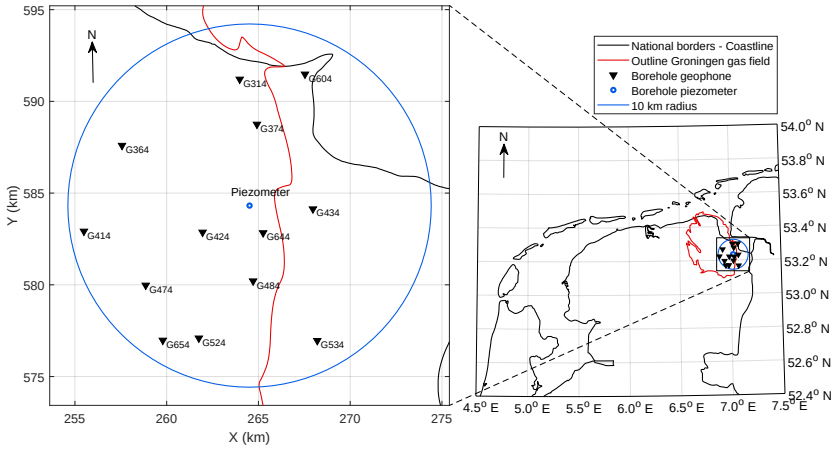

Figure 2.1: Map view of the locations of the measurement equipment employed in this study. The location of the piezometer *B08C0952* (Dinoloket, 2022) is plotted as a blue point, around which the blue circle indicates a 10 km radius. All geophones within this radius at 200 m depth (KNMI, 1993) are shown as black triangles. The outline of the Netherlands and the Groningen gas field are shown as black and red lines.

measurements of surface-wave phase-velocity changes, we applied passive image interferometry to seismic noise. To this end, we used seismic data from borehole geophones (KNMI, 1993) at 200 m depth, located within a 10 km radius from the piezometer (Figure 2.1).

2.3.1. Static Model

The static parameters in Equations 2.9-2.11 are μ and μ'_p. They are estimated from detailed subsurface models available in the Groningen area. As a starting point, we used a local shear-wave velocity and density model from Kruiver et al. (2017a) and a compressional-wave velocity model from Romijn (2017) at $[X_{RD}, Y_{RD}]$ = [261.96 km, 582.86 km], visualized in Figure 2.2a-c. Note that the chosen model location below receiver G424 very close to the piezometer is a point location, whereas the used surface waves sample the entire region. Using compressional-wave (a), shear-wave (b) and density models (c) we computed the bulk modulus (d), the shear modulus (e), and the confining pressure (f). A smoothed derivative of the shear modulus with respect to the confining pressure μ'_p is shown in Figure 2.2g. Note that μ increases with depth, whereas μ'_p decreases with depth. μ'_p has values above 50 for most of the unconsolidated-sediment depth range (upper 800 m) and much smaller values for the underlying chalk rock.

2.3.2. Stress Model

The borehole piezometer shown in Figure 2.1 (Dinoloket, 2022) has registered pressure heads (i.e., the levels to which groundwater rises in a frictionless tube due to pore pressure) at depths z_i = 7.3, 27.3, 105.3, 132.3, and 170.8 m. Figure 2.3a shows

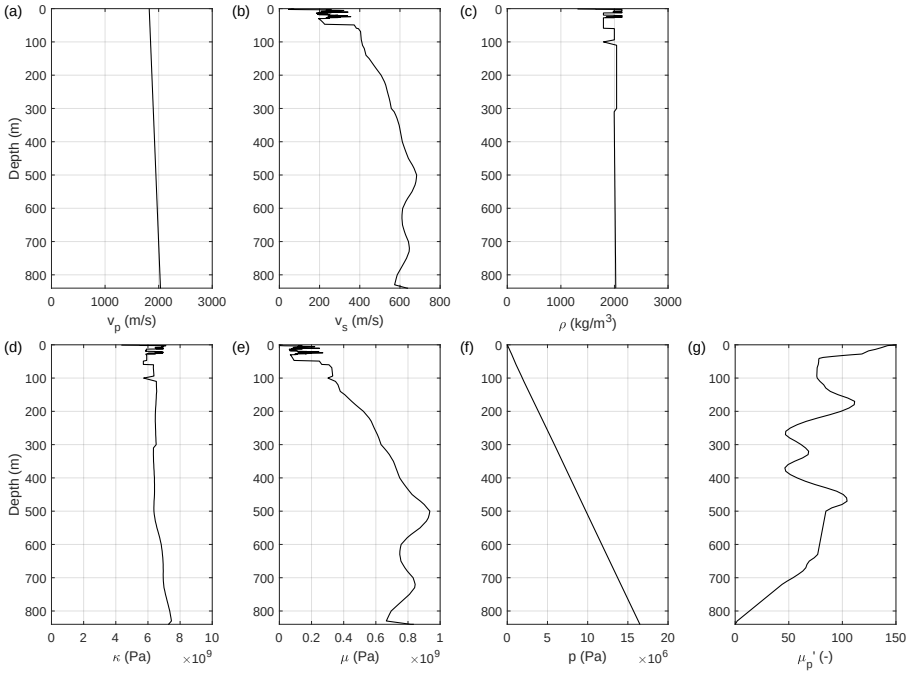

Figure 2.2: Static models: (a) Compressional-wave velocity v_p, (b) shear-wave velocity v_s, (c) mass density ρ, (d) bulk modulus $\kappa = \rho v_p^2 - \frac{4}{3}\rho v_s^2$, (e) shear modulus $\mu = \rho v_s^2$, (f) confining pressure $P = \int_0^z \rho(z) g \, dz$, with g the gravitational acceleration and z the depth below surface, (g) the shear-modulus pressure derivative $\mu_p' = d\mu/dP$, based on the smoothed derivative of the shear modulus with respect to confining pressure.

the change in pressure head $dh(z_i,t)$ with respect to the average pressure head between 01 January 2017 and 31 December 2019. If there were a high permeability between the measurement depths z_i, all measurements $dh(z_i,t)$ should be identical. Figure 2.3a shows this is not the case for depths $z < 105.3$ m. This corresponds with the presence of low-permeability clay layers in this depth range.

From a linear interpolation of the pressure head, we obtained changes in pore pressure $du(z,t) = \rho_w g\ dh(z,t)$ as a function of depth and time. $dh(z_i,t)$ values at the deepest three measurement levels are nearly identical. For that reason, we extrapolated $dh(z,t)$ below depths of 170.8 m as a constant with depth down to 840 m and set dh to zero for $z > 840$ m, from where the sediments become consolidated. The resulting $du(z,t)$ field is shown in Figure 2.3b for parameters $\rho_w = 1000$ kg/m^3 and $g = 9.8$ m/s^2.

To estimate the order of magnitude of the induced vertical compressional stress, we assumed that changes in pressure head at the shallowest level are similar to changes in the groundwater table. Hence, we used $d\sigma_{zz}(t) \approx -\phi\rho_w g\ dh$ ($z = 7.3$ m, t). Figure 2.3c shows the result for porosity $\phi \sim 0.25$.

2.3.3. Shear-Wave Velocity Change

To compare the effects of groundwater table loading $d\sigma_{zz}$ and induced pore pressure du on the seismic velocity, we studied the orders of magnitude that can be predicted using Equations 2.9-2.11. Typical values for stress and pore pressure can be found on 01 Jan 2018, when the (induced) compressional stress is estimated at $d\sigma_{zz} \approx -1000$ Pa, and the average pore pressure is $du \approx 2000$ Pa. Using the information of Figures 2.2e,g ($\mu_p' \approx 80$ and $\mu \approx 5\times10^8$ Pa) in Equations 2.9 and 2.11, we found, for the groundwater loading, a relative increase in shear-wave velocity $dv_s/v_s = -\frac{\mu_p'\mp1}{4\mu}d\sigma_{zz} \approx 0.004\%$, and for the induced pore pressure, we found a relative decrease in shear-wave velocity $dv_s/v_s = -\frac{\mu_p'}{2\mu}du \approx -0.02\%$. Since the effect of vertical compressional stress is considerably smaller than the pore pressure effect in our Groningen setting, and we have no accurate measurements of $d\sigma_{zz}$, we chose to neglect the effect of the vertical compressional stress. Hence, we simplify Equations 2.9-2.11 to

$$\left(\frac{dv_s}{v_s}\right) \approx -\frac{\mu_p'}{2\mu}du. \tag{2.12}$$

In accordance with Equation 2.12 we used the information from Figures 2.2e, 2.2g and 2.3b to construct shear-wave velocity changes as a function of time and depth. The result in Figure 2.4 forms the basis in the forward modeling of surface-wave velocity changes. The effects of the pore pressure du are mainly responsible for the time-lapse variations, while the shear modulus μ and its pressure derivative μ_p' regulate the amplification of shear-wave velocity changes as a function of depth. For instance, at the interface at 50 m depth, the amplitude of velocity change rapidly decreases due to an increase in the shear modulus (Figure 2.2e), and a decrease in the pressure derivative of the shear modulus (Figure 2.2g).

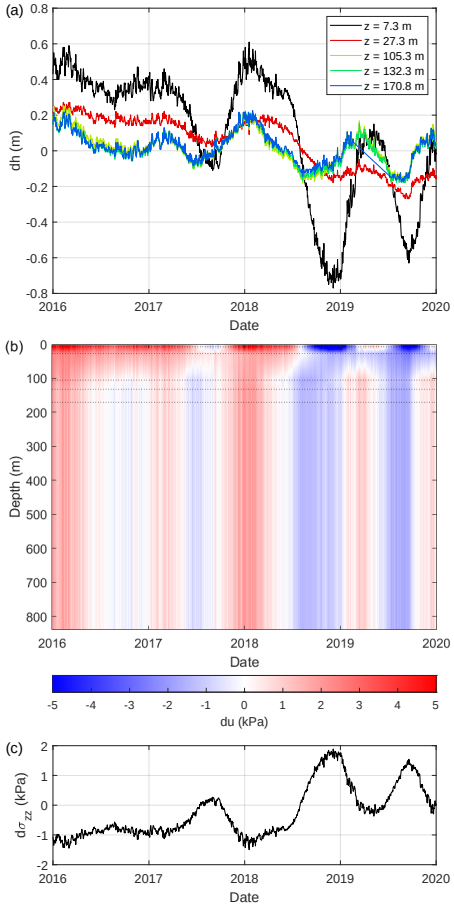

Figure 2.3: (a) Time-lapse changes in pressure head $dh(z_i, t)$, with respect to the average pressure head between 01 Jan 2017 and 31 Dec 2019, for z_i = 7.3, 27.3, 105.3, 132.3, and 170.8 m depth. (b) Induced pore pressure $du(z,t) = \rho_w g\ dh(z,t)$ for parameters ρ_w = 1000 kg/m^3 and g = 9.8 m/s^2, obtained from linear interpolation of $dh(z_i, t)$. The dashed lines indicate the measurement depths of the pressure head. (c) Estimate of induced vertical compressional stress $d\sigma_{zz} = -\phi\rho_w g\ dh(z = 7.3\text{ m}, t)$ for $\phi \approx 0.25$.

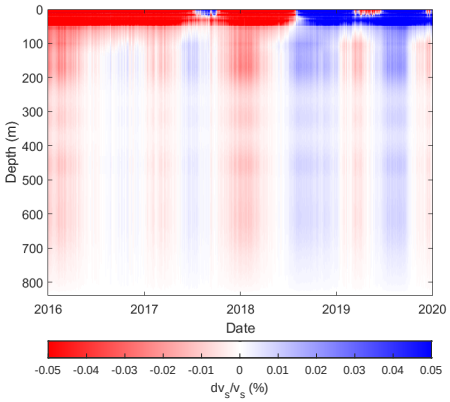

Figure 2.4: Modeled shear-wave velocity change in accordance with Equation 2.12 and Figures 2.2e, 2.2g and 2.3b.

2.3.4. Surface-Wave Dispersion Forward Modeling

Given our physics-based relationship regarding shear-wave velocity change as a function of depth (simplified as Equation 2.12), and our observations of surface-wave phase velocity changes as a function of frequency (Section 2.3.5), we can relate them through surface-wave dispersion modeling. Assuming that the lateral variations in our region of interest are small, we can use a one-dimensional average static model of the subsurface and use the adjoint technique of Hawkins (2018) to compute sensitivity kernels which relate partial derivatives of the change in surface-wave phase velocities (Love and Rayleigh) to the small stress-induced changes in shear-wave velocities. These partial derivatives can be used to estimate the effect on relative changes in surface-wave phase velocities using

$$\frac{dc}{c}(\omega_i) = \frac{1}{c(\omega_i)} \sum_j \frac{\partial c}{\partial v_{sj}}(\omega_i) v_{sj} \frac{dv_{sj}}{v_{sj}}, \tag{2.13}$$

where $\partial c/\partial v_{sj}\ (\omega_i)$ is the partial derivative of the surface-wave phase velocity with respect to v_{sj} at frequency ω_i, dv_{sj} is the small perturbation to v_{sj}, and $c(\omega_i)$ is the actual surface-wave phase velocity. While this approach is approximate and discounts the impact of anelasticity and lateral heterogeneity, it is sufficient to demonstrate that the stress-induced changes in shear-wave phase velocities give the correct changes in observed surface-wave velocities.

For the static models introduced in Section 2.3.1, we computed the sensitivity kernels of fundamental Rayleigh and Love waves for density, compressional-wave velocity and shear-wave velocity. Figure 2.5 shows the kernels at a frequency of 1 Hz. This figure shows that, in the Groningen setting, fundamental mode Love waves are more sensitive to shallower changes than Rayleigh waves, which peak around 200 m depth.

Figure 2.6 shows several eigen modes for Love and Rayleigh waves at 1 Hz, indicating that there should be reasonable amounts of Rayleigh-wave energy recorded

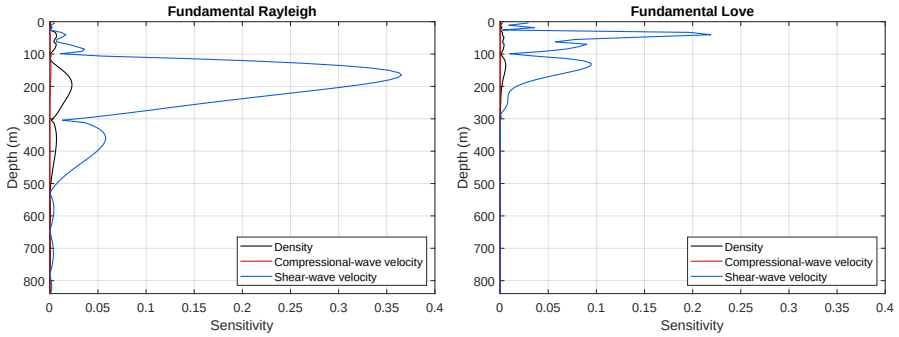

Figure 2.5: Absolute value of the sensitivity kernels for fundamental Rayleigh and Love waves for density, compressional-wave velocity and shear-wave velocity at a frequency of 1 Hz.

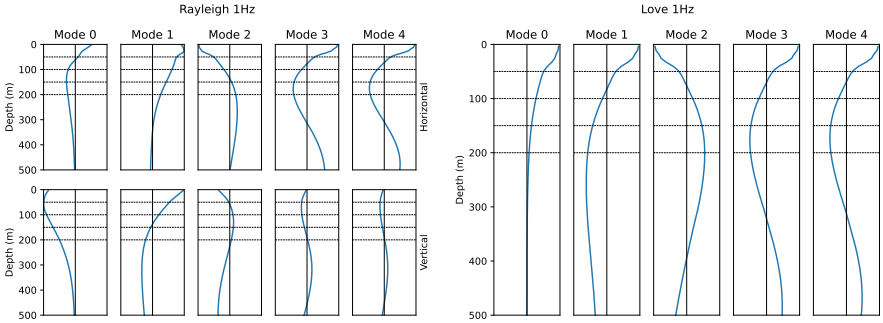

Figure 2.6: Eigen-mode amplitudes as function of depth for Rayleigh waves (amplitudes of both the horizontal and vertical components normalized to preserve amplitude ratios) and Love waves at 1 Hz.

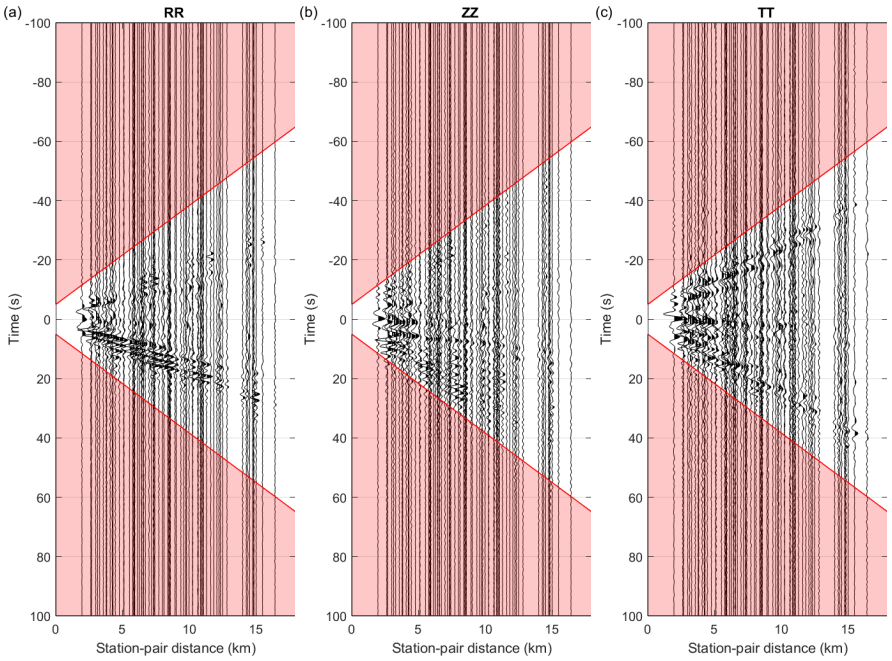

Figure 2.7: Reference cross-coherence H_{ref} (i.e., average cross-coherence between 01 Jan 2017 and 31 Jan 2019) for all combinations of receivers shown in Figure 2.1 as a function of receiver-pair distance for components RR, ZZ and TT. The red lines indicate the arrival times $|t| = x/300 + 5$, between which we can expect all arrivals of direct surface waves, while the red area indicates the coda time windows $(x/300 + 5)$ s $< |t| \leq 100$ s, used in Equation 2.15 to retrieve relative velocity change.

at a depth of 200 m (depth of the borehole geophones we are going to use below), but little fundamental Love-wave energy. Overtones of both Love and Rayleigh will be recorded if excited by the seismic noise; however, our analysis suggests that the fundamental mode is dominant, at least in ZZ and TT cross-coherence's (Figure 2.7), as shown in Figure 2.8.

Using the adjoint method (Hawkins, 2018), we modeled surface-wave velocity changes corresponding to the shear-wave velocity changes shown in Figure 2.4. Figure 2.9 shows the relative velocity changes for the example frequency of 1 Hz as a function of date (a) and for the example date 31 Aug 2019 as a function of frequency (b). We show relative velocity change of Love waves (black), Rayleigh waves (red), and its Voigt average $(dc/c)_{Voigt} = \frac{2}{3}(dc/c)_{Rayleigh} + \frac{1}{3}(dc/c)_{Love}$. Love waves show a larger induced velocity change than Rayleigh waves. This can be understood from their higher sensitivity to shallow depths (Figure 2.5), where the largest shear-wave velocity changes occur (Figure 2.4). For low frequencies, we used the Voigt average of Rayleigh and Love waves, but higher frequencies (Figure 2.8) show less energy for Love waves than for Rayleigh waves. Therefore, we used Rayleigh wave velocity change for frequencies $f \geq 1$ Hz, which has a much lower amplitude than the Voigt average.

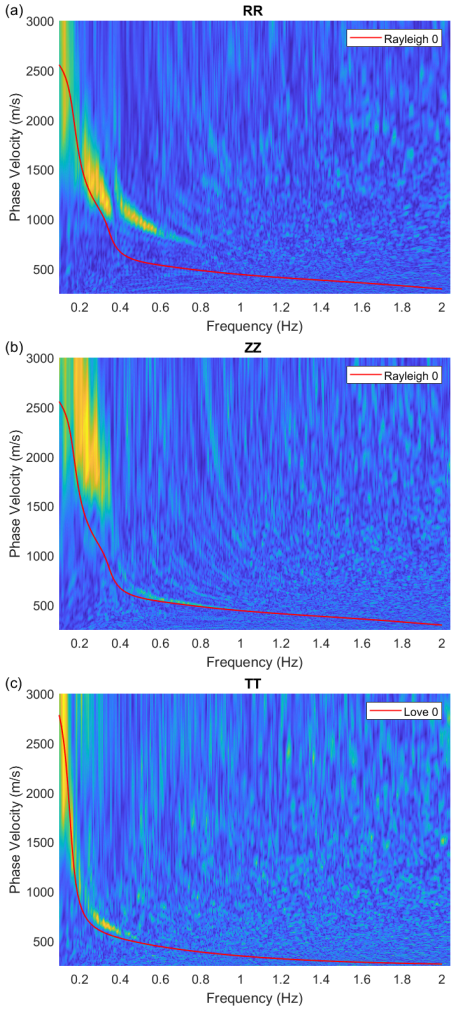

Figure 2.8: Multichannel analysis of surface waves (Park et al., 1998) of the reference cross-coherences shown in Figure 2.7 for components (a) RR , (b) ZZ, and (c) TT , visualized in a power plot. The red lines indicate the fundamental dispersion curves of (a,b) Rayleigh and (c) Love waves, obtained with the adjoint method (Hawkins, 2018).

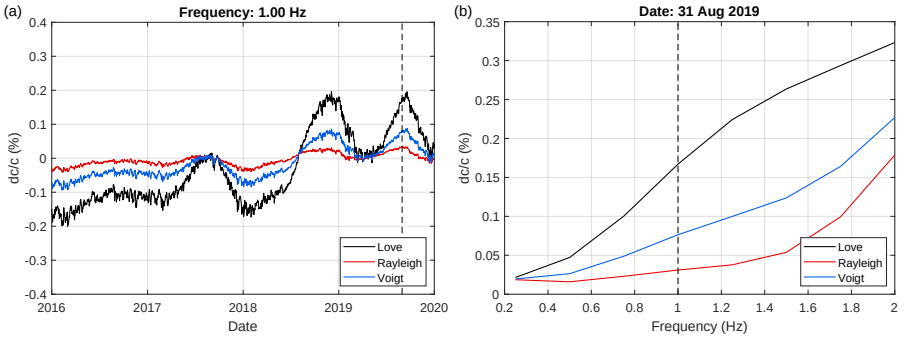

Figure 2.9: (a) Modeled surface-wave velocity changes for example frequency 1 Hz as a function of date, and (b) for the example date 31 Aug 2019 as a function of frequency. The individual lines represent velocity change of Love waves (black), Rayleigh waves (red) and their Voigt average $dc_V/c_V = \frac{2}{3}dc_R/c_R + \frac{1}{3}dc_L/c_L$ (blue).

2.3.5. Passive Image Interferometry

In an approach similar to Fokker and Ruigrok (2019), building upon the work of Sens-Schönfelder and Wegler (2006), we retrieved relative changes in the seismic velocity using passive image interferometry, consisting of two main processes. First, the time-varying Green's functions between two seismic receivers were estimated. Second, these estimates were used to determine the relative changes in arrival time, corresponding to the relative changes in velocity.

To estimate a daily Green's function (i.e., a one-day average of a Green's function), we computed the cross-coherence, i.e., the spectrally normalized cross-correlation (Wapenaar et al., 2010b), of ambient seismic noise, recorded by seismic receivers at x_A and x_B:

$$\hat{H}(x_B, x_A, \omega) = \frac{\hat{w}(x_B, \omega)\,\hat{w}^*(x_A, \omega)}{|\hat{w}(x_B, \omega)||\hat{w}(x_A, \omega)|}. \tag{2.14}$$

The frequency domain is indicated by a hat and the star denotes a complex conjugation. We stacked cross-coherences calculated from 50% overlapping time windows of 20 min durations, where the first time window ranges from 0:00 to 0:20 UTC, the second from 0:10 to 0:30 UTC, etc. We repeated this procedure for the data of every day between 1 January 2016 and 1 January 2020. The cross-coherences were computed for all component combinations. To speed up computation, we applied rotations to radial (R) and transverse (T) components after cross-correlation. Applying rotation after correlation gives a small yet acceptable error (Appendix 2.B). Figure 2.7 shows the average cross-coherence between 1 January 2017 and 31 December 2019 as a function of distance between receivers. A different time period was chosen for the reference cross-coherence, since in 2016 quite a lot of data are missing. In this way, the reference cross-coherence contains equal contributions from all seasons, while available data from 2016 can still be compared to a well estimated Green's function.

We determined velocity changes using the stretching method in the time do-

main (Lobkis & Weaver, 2003). Relative velocity changes $dv/v = \epsilon$ were found at the maximum correlation coefficient $CC(\epsilon)$ between lapse (daily) cross-coherence H_{lapse}, stretched in time with factor $(1-\epsilon)$, and reference cross-coherence H_{ref},

$$CC(\epsilon) = \frac{\int_{t_1}^{t_2} H_{\text{lapse}}[t(1-\epsilon)]H_{\text{ref}}[t]dt}{\sqrt{\int_{t_1}^{t_2}\left(H_{\text{lapse}}\right)^2[t(1-\epsilon)]dt}\sqrt{\int_{t_1}^{t_2}(H_{\text{ref}})^2[t]dt}}. \tag{2.15}$$

The obtained velocity changes are relative to the reference cross-coherence, here defined as the average cross-coherence between 1 January 2017 and 31 December 2019 (Figure 2.7). We decided to only use the coda of the cross-coherence (red areas in Figure 2.7), because the coda is less dependent on changes in illumination, and velocity change causes larger changes in traveltime for late arrivals. This results in more accurate and stable measurements of the velocity change. As time windows (integration boundaries in Equation 2.15) for the cross-coherence, we therefore used $(x/300+5)$ s $< |t| \leq 100$ s, where the first term is the distance x between the two receivers divided by the minimum expected propagation velocity. An additional 5 s was added to exclude the direct field with certainty. We applied bandpass filters to the cross-coherences, varying both the center frequency and the frequency span to obtain surface wave velocity changes as a function of frequency.

A disadvantage of the stretching method is spurious velocity changes when coda-wave amplitudes vary (Zhan et al., 2013). The use of a spectral normalization of the cross-correlation, the cross-coherence, limits amplitude variations, but when the ambient noise amplitudes are weaker than the normalization water level used, the amplitudes of the cross-coherence change, resulting in spurious arrivals. For this reason, we analyzed the velocity change distributions of 78 receiver pairs (Figure 2.1). Spurious arrivals can easily be spotted by an inconsistent distribution of velocity change. Figure 2.10 shows an example of an inconsistent distribution of velocity change. These spurious velocity changes can especially be observed during summers and at low frequencies ($f < 0.2$ Hz). During these seismically quiet periods, the 4.5 Hz geophones record a significant proportion of instrumental noise, which results in a poor estimate of the Green's function.

Employing coda waves measured on the horizontal components, we cannot distinguish between Rayleigh, Love and body waves, since the coda consists of multiply-scattered waves. To show that surface waves dominate the Groningen noise, we applied multichannel analysis of surface waves (Park et al., 1998) to the reference cross-coherences, measured on the radial, vertical and transverse components. Figure 2.8 shows a strong presence of both Rayleigh and Love waves. The surface-wave dispersion can be seen up until about 1 Hz. The dispersion cannot be discerned at higher frequencies, probably due to the near-surface heterogeneity over the area sampled with the 78 receiver pairs (Figure 2.1). Since surface waves dominate Green's function estimates (the cross-coherences), we treat the average velocity change in the coda for lower frequencies as the Voigt average of the Rayleigh and Love wave phase velocity changes, and for higher frequencies as Rayleigh wave phase velocity changes. Figure 2.11 shows that for the coda of the cross-coherence every horizontal component configuration (i.e., RR, RT, TR,

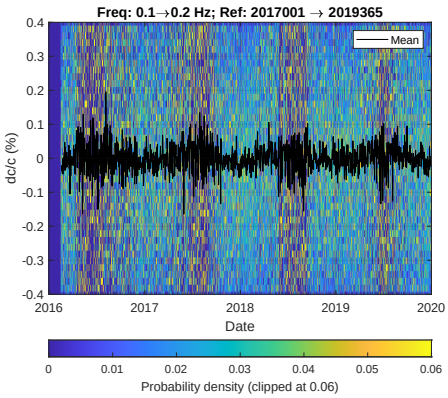

Figure 2.10: Time-lapse seismic velocity change retrieved from seismic ambient noise within frequency bandwidth [0.1 0.2] Hz, using the coda of the cross-coherence of horizontal (RR, RT, TR, TT) components between 78 receiver combinations. The background colors show the probability distribution of 312 estimates from dark blue (low probability) to yellow (high probability), while the black line shows the average velocity change.

TT) leads to similar velocity changes. This indicates that arrivals of both Love and Rayleigh waves can indeed be measured on the coda of all horizontal components. An average over all horizontal component configurations will lead to a cleaner distribution of velocity change. For the cross-coherence of vertical motion at both receivers, Rayleigh waves dominate. Hence, we treat velocity change obtained with coda waves recorded on the vertical component as phase velocity changes in the Rayleigh wave.

2.3.6. Model Validation

Relative seismic phase-velocity variations were retrieved for all combinations of the seismic receivers indicated in Figure 2.1 for frequency bandwidths [0.3 0.4] Hz, [0.7 0.8] Hz, [1.0 1.2] Hz, and [1.3 1.6] Hz. Figure 2.12 presents the mean velocity change (black) and its distribution (colored background) of 78 station combinations of one vertical (ZZ; left) and four horizontal-component configurations (i.e., the average velocity change of components RR, RT, TR, TT; right). The observations of surface-wave velocity change (black) match the results of the independent forward model (purple and red) quite well, both in shape and magnitude. For the vertical component and the higher frequencies of the horizontal components, the Rayleigh-wave velocity-change model is shown. For the lower frequencies of the horizontal components, a Voigt average was taken over the Rayleigh and Love velocity-change models (Figure 2.9).

2.4. Discussion

To retrieve velocity variations of surface waves, we used the stretching method (Lobkis & Weaver, 2003). This method is based on the assumption that velocity

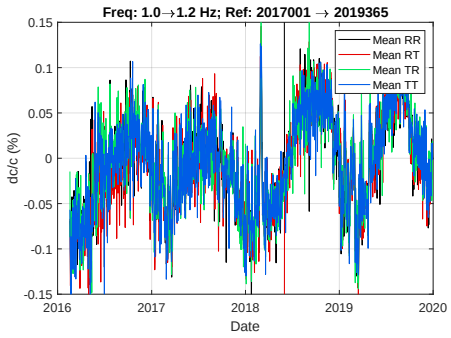

Figure 2.11: Time-lapse seismic velocity change retrieved from seismic ambient noise within frequency bandwidth [1.0 1.2] Hz, using the coda of the cross-coherence of individual horizontal component configurations, averaged over 78 receiver combinations.

change is homogeneous. This assumption is valid for velocity changes due to fluctuations in the pore pressure, because the causes of these fluctuations, i.e., precipitation and evaporation, are similar for the whole area. Local velocity changes, for which the assumption is not valid, cannot be retrieved using this method.

In a similar study Fokker and Ruigrok (2019) retrieved velocity variations in a region 15 km northwest of the area sampled in this study. Compared to their results, our velocity variations are three times smaller. This discrepancy can likely be explained by differences in depth sensitivity for fundamental modes and the overtones of Rayleigh waves, and the dominant amplitude of motion at 50 and 200 m depths. At a depth of 200 m, used in the present study, motion of the fundamental mode dominate over motion of the overtones (Figure 2.8). At a depth of 50 m, used by Fokker and Ruigrok (2019), motion of the first overtone dominates over the motion of the fundamental mode. In Mordret et al. (2020), it is shown that, in the Groningen setting, the first overtone of the Rayleigh wave has a higher sensitivity to velocity changes than the fundamental mode.

Note that, for some frequencies, we observed the first Rayleigh overtone on the RR com-ponent (Figure 2.8), while we used the fundamental mode in the modeling (Figures 2.9 and 2.12). The match between model and observation will likely improve when overtones are included.

In our model for velocity change, we excluded the Love wave contribution for frequencies $f \geq 1$ Hz, due to the low Love-wave energy (Figure 2.8) and its relatively small amplitude at 200 m depth (Figure 2.6). If the Voigt average (Figure 2.9 blue) was taken at these higher frequencies, the amplitude of the velocity change model would be much higher. The Voigt averaged model for velocity change would overestimate the velocity change observations at higher frequencies (Figure 2.12f,h).

In our stress model (Section 2.3.2), we interpolated the change in pressure head between the measurement depths, we extrapolated dh as uniform changes between 170.8 m and 840 m depth, and we assumed no changes below the consolidation interface at 840 m depth. We expected the permeability to decrease at this interface, limiting the changes in pore pressure. However, pore pressure changes at

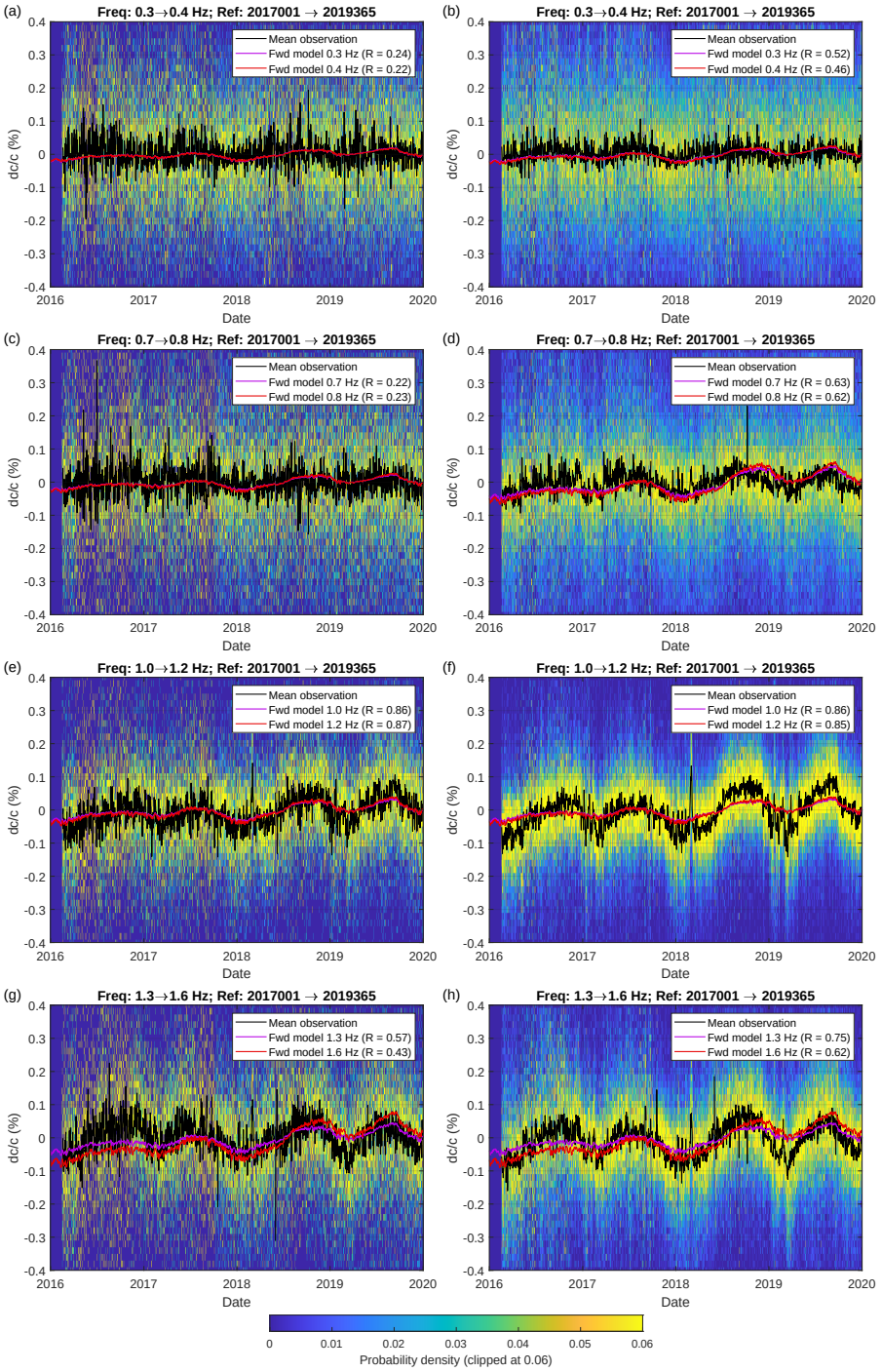
(a)
Freq: 0.3→0.4 Hz; Ref: 2017001 → 2019365
Mean observation
Fwd model 0.3 Hz (R = 0.24)
Fwd model 0.4 Hz (R = 0.22)
(b)
Freq: 0.3→0.4 Hz; Ref: 2017001 → 2019365
Mean observation
Fwd model 0.3 Hz (R = 0.52)
Fwd model 0.4 Hz (R = 0.46)
(c)
Freq: 0.7→0.8 Hz; Ref: 2017001 → 2019365
Mean observation
Fwd model 0.7 Hz (R = 0.22)
Fwd model 0.8 Hz (R = 0.23)
(d)
Freq: 0.7→0.8 Hz; Ref: 2017001 → 2019365
Mean observation
Fwd model 0.7 Hz (R = 0.63)
Fwd model 0.8 Hz (R = 0.62)
(e)
Freq: 1.0→1.2 Hz; Ref: 2017001 → 2019365
Mean observation
Fwd model 1.0 Hz (R = 0.86)
Fwd model 1.2 Hz (R = 0.87)
(f)
Freq: 1.0→1.2 Hz; Ref: 2017001 → 2019365
Mean observation
Fwd model 1.0 Hz (R = 0.86)
Fwd model 1.2 Hz (R = 0.85)
(g)
Freq: 1.3→1.6 Hz; Ref: 2017001 → 2019365
Mean observation
Fwd model 1.3 Hz (R = 0.57)
Fwd model 1.6 Hz (R = 0.43)
(h)
Freq: 1.3→1.6 Hz; Ref: 2017001 → 2019365
Mean observation
Fwd model 1.3 Hz (R = 0.75)
Fwd model 1.6 Hz (R = 0.62)
dc/c (%)
Date
Probability density (clipped at 0.06)

Figure 2.12

Figure 2.12: Time-lapse seismic velocity change retrieved from seismic ambient noise within the indicated frequency bandwidths, using the coda of the cross-coherence of vertical (left; ZZ) and horizontal (right; RR, RT, TR, TT) components between 78 receiver combinations. The background colors show the probability distribution of 78 (left) and 312 (right) estimates from dark blue (low probability) to yellow (high probability), while the black line shows the average velocity change. The purple and red lines show the results of the independent forward model for velocity change of Rayleigh waves (a,c,e,f,g,h) and the Voigt average (b,d) as in Figure 2.9. The match between the low-frequency trends of the modeled and the observed velocity change is quantified with a Pearson correlation after a low-pass filter is applied with a cut-off period of 60 days. The correlation coefficient R is shown in the legend.

depths below 840 m depth are not relevant for the purpose of this study, since the waves we study have no sensitivity to changes at depths below 500 m (Figure 2.5).

We observed that some studies found a positive correlation between groundwater fluctuations and velocity changes (Liu et al., 2020; Voisin et al., 2017), while others found an anti-correlation (Clements & Denolle, 2018; Hillers et al., 2014; Nakata & Snieder, 2012; Sens-Schönfelder & Wegler, 2006; Tsai, 2011). This can be explained by the different mechanisms presented in the Section 2.2. The contributions of du and $d\sigma_{zz}$ in Equations 2.9 and 2.11 have opposite effects: an increase in pore pressure results in a decrease in seismic velocity, while an increase in compressional stress (T_{zz} becomes more negative) results in an increase in seismic velocity. The balance between the mechanisms depends, on the one hand, on the permeability determining the size of du, relative to $d\sigma_{zz}$. On the other hand, it depends on the presence of Rayleigh and Love waves, and their responses to changes in shear-wave velocities. Both negative and positive correlations with, respectively, pore pressure and surface weight were found by Wang et al. (2017), who modeled the pore pressure from precipitation measurements and used measurements of snow depth for the surface loading.

This article argues that shear-wave velocity changes are caused by fluctuations of the effective stress through changes in the shear modulus. There is, however, a second mechanism to couple velocity change to induced effective stress. Effective pressure leads to compaction, affecting the density and hence the shear-wave velocity. This effect can be quantified using the density derivative of the shear-wave velocity, $dv_s/v_s = -\frac{1}{2}d\rho/\rho$, and the definition of the Bulk modulus, $d\rho/\rho = dp/\kappa$. A rise in effective pressure $d\tilde{p} = -du - \frac{1}{3}d\sigma_{zz}$ would induce a relative change in density $d\rho/\rho = -(du + \frac{1}{3}d\sigma_{zz})/\kappa$, resulting in an increase in shear-wave velocity $dv_s/v_s = (du + \frac{1}{3}d\sigma_{zz})/(2\kappa)$. For a typical bulk modulus in the Groningen subsurface, $\kappa \sim 5 \cdot 10^9$ Pa (Figure 2.2d), this would result in velocity changes that are two to three orders of magnitude smaller than the ones observed. Therefore, we neglected the mechanism of compaction.

This study focuses on seismic velocity changes due to changes in the pore pressure. Here, we address sources for velocity changes that could not have been measured due to our choices for surface waves, frequency bandwidths, temporal resolution and methodology.

In some studies, atmospheric temperature variations are correlated to seismic velocity change (e.g., Mao et al., 2019). The temperature oscillations in the sub-

surface, due to yearly atmospheric temperature variations, can mathematically be described as a highly damped wave propagating downwards. Most of the effect is located above 20 m. For depths below 20 m, the temperature changes for quartz, with a thermal diffusivity $\alpha_d = 1.4$ mm^2/s, would be limited to 0.1 °C. The surface waves, with frequencies we used, have no sensitivity to changes at depths shallower than 20 m (Figure 2.5). Furthermore, surface waves are sensitive to changes over a large range of depths, while the wavelength of the thermal 'wave' is approximately 25 m, resulting in temperature contributions of a range of seasons. This would not be detectable using surface waves at frequencies lower than 2 Hz.

Velocity changes caused by the Lunar tides were also left out, because we have only one velocity measurement per day, whereas Lunar tides cause two oscillations of velocity change per day. Velocity changes induced by Groningen earthquakes (maximum magnitude 3.4, at 3 km depth) would not be detectable due to the relatively small induced stress in the shallow subsurface and the heterogeneous nature of the velocity changes. Changes in water saturation are not relevant as a potential source either, since these changes can only be observed above the groundwater table, which around Groningen is at a depth of approximately 1 m.

The derived relationship between shear-wave velocity and induced effective stress is validated in the context of surface waves, traveling through the shallow subsurface of the Earth. It provides a new understanding of time-lapse variations in the subsurface. We postulate that it can be directly applied to monitoring studies using shear waves or compressional waves (Appendix 2.A) and may provide new insights in monitoring civil structures.

2.5. Conclusions

In this study, we developed a theory relating seismic velocity change to fluctuations in the pore pressure and vertical stress. By combining a relationship between seismic velocity and induced stress, derived from first principles (Tromp & Trampert, 2018), with basic hydrology and geomechanics, we derived a physics-based relationship for seismic velocity changes as a function of induced pore pressure, vertical compressional stress and elastic parameters. To validate this relationship, we modeled seismic surface-wave velocity changes, based on measurements of the pressure head, using the newly derived relationship and the adjoint method (Hawkins, 2018). Surface-wave velocity changes were independently retrieved by applying passive image interferometry (Sens-Schönfelder & Wegler, 2006) to seismic noise measured in the subsurface of Groningen, the Netherlands. The close match between model and observation shows the validity of the derived theory, and justifies the use of seismic velocity variations for pore pressure monitoring.

2.A. Stress-Induced Compressional-Wave Velocity Change

Similar to the derivation in Section 2.2 we can derive compressional-wave velocity change, starting from Tromp and Trampert (2018, Equation 37):

$$\begin{aligned}
\rho \tilde{v_p}^2 &= \left(\kappa + \kappa'_p dp\right) + \frac{4}{3}\left(\mu + \mu'_p dp\right) - \left(\kappa'_p + \frac{4}{3}\mu'_p\right)\hat{\boldsymbol{k}}\cdot d\boldsymbol{\tau}\cdot\hat{\boldsymbol{k}}, \\
\rho\left(\left(v_p + dv_p\right)^2 - v_p^2\right) &= \left(\kappa'_p + \frac{4}{3}\mu'_p\right)\left(dp - \hat{\boldsymbol{k}}\cdot d\boldsymbol{\tau}\cdot\hat{\boldsymbol{k}}\right), \\
\frac{dv_p}{v_p}\left(2 + \frac{dv_p}{v_p}\right) &= \frac{\kappa'_p + \frac{4}{3}\mu'_p}{\kappa + \frac{4}{3}\mu}\left(dp - \hat{\boldsymbol{k}}\cdot d\boldsymbol{\tau}\cdot\hat{\boldsymbol{k}}\right), \\
\frac{dv_p}{v_p} &\approx \frac{1}{2}\frac{\kappa'_p + \frac{4}{3}\mu'_p}{\kappa + \frac{4}{3}\mu}\left(dp - \hat{\boldsymbol{k}}\cdot d\boldsymbol{\tau}\cdot\hat{\boldsymbol{k}}\right), \qquad (2.16)
\end{aligned}$$

where v_p represents compressional-wave velocity, κ represents the bulk modulus, and κ'_p its pressure derivative.

Using Equations 2.6 and 2.7, we derive the relative compressional-wave velocity change for vertical ($\hat{k}_x = \hat{k}_y = 0;\ \hat{k}_z = 1$) and horizontal propagation ($\hat{k}_x^2 + \hat{k}_y^2 = 1;\ \hat{k}_z = 0$):

$$\left(\frac{dv_p}{v_p}\right)^{Vertical} \approx -\frac{1}{2}\frac{\kappa'_p + \frac{4}{3}\mu'_p}{\kappa + \frac{4}{3}\mu}\left(du + d\sigma_{zz}\right), \qquad (2.17)$$

$$\left(\frac{dv_p}{v_p}\right)^{Horizontal} \approx -\frac{1}{2}\frac{\kappa'_p + \frac{4}{3}\mu'_p}{\kappa + \frac{4}{3}\mu}du. \qquad (2.18)$$

2.B. Rotation Approximation

For the estimation of the Green's function in the radial and transverse directions, we need to rotate the seismic measurements to face these directions. Traditionally, this is carried out before a cross-correlation is made. However, the data that are stored after cross-correlation are only a fraction of the raw data. For this reason, the computation time can be significantly reduced when the rotation is carried out after the cross-correlation. In this appendix, we assess the error that is introduced by applying rotation after cross-correlation.

A cross-correlation of radial–radial components can, in the frequency domain, be written as

$$\begin{aligned}
\hat{C}_{BA}^{RR} &= \hat{w}_B^R \hat{w}_A^{R*}, \\
&= \left(\hat{w}_B^N \cos\phi + \hat{w}_B^E \sin\phi\right)\left(\hat{w}_A^{N*}\cos\phi + \hat{w}_A^{E*}\sin\phi\right), \\
&= \hat{w}_B^N \hat{w}_A^{N*}\cos^2\phi + \left(\hat{w}_B^N \hat{w}_A^{E*} + \hat{w}_B^E \hat{w}_A^{N*}\right)\cos\phi\sin\phi + \hat{w}_B^E \hat{w}_A^{E*}\sin^2\phi, \\
&= \hat{C}_{BA}^{NN}\cos^2\phi + \left(\hat{C}_{BA}^{NE} + \hat{C}_{BA}^{EN}\right)\cos\phi\sin\phi + \hat{C}_{BA}^{EE}\sin^2\phi, \qquad (2.19)
\end{aligned}$$

where $\hat{w}_B^R$ represents motion at location x_B in the radial direction, ϕ represents the clockwise angle between the station orientation (i.e. the line between x_A and x_B) and the North, and $\hat{C}_{BA}^{NE}$ denotes the cross-correlation between the motion at x_B in the northern direction and at x_A in the eastern direction. Similarly, we find

$$\hat{C}_{BA}^{TT} = \hat{C}_{BA}^{NN}\sin^2\phi + \left(-\hat{C}_{BA}^{NE} - \hat{C}_{BA}^{EN}\right)\cos\phi\sin\phi + \hat{C}_{BA}^{EE}\cos^2\phi, \tag{2.20}$$

$$\hat{C}_{BA}^{RT} = \hat{C}_{BA}^{NE}\cos^2\phi + \left(-\hat{C}_{BA}^{NN} + \hat{C}_{BA}^{EE}\right)\cos\phi\sin\phi - \hat{C}_{BA}^{EN}\sin^2\phi, \tag{2.21}$$

$$\hat{C}_{BA}^{TR} = -\hat{C}_{BA}^{NE}\sin^2\phi + \left(-\hat{C}_{BA}^{NN} + \hat{C}_{BA}^{EE}\right)\cos\phi\sin\phi + \hat{C}_{BA}^{EN}\cos^2\phi, \tag{2.22}$$

$$\hat{C}_{BA}^{RZ} = \hat{C}_{BA}^{NZ}\cos\phi + \hat{C}_{BA}^{EZ}\sin\phi, \tag{2.23}$$

$$\hat{C}_{BA}^{ZR} = \hat{C}_{BA}^{ZN}\cos\phi + \hat{C}_{BA}^{ZE}\sin\phi, \tag{2.24}$$

$$\hat{C}_{BA}^{TZ} = -\hat{C}_{BA}^{NZ}\sin\phi + \hat{C}_{BA}^{EZ}\cos\phi, \tag{2.25}$$

$$\hat{C}_{BA}^{ZT} = -\hat{C}_{BA}^{ZN}\sin\phi + \hat{C}_{BA}^{ZE}\cos\phi, \tag{2.26}$$

$$\hat{C}_{BA}^{ZZ} = \hat{C}_{BA}^{ZZ}. \tag{2.27}$$

If no normalization has been applied both in the time and frequency domains, the result should be identical if the rotation was applied before or after the cross-correlation. This we indeed observed. When spectral whitening is applied, however, differences are expected, because the spectra of Rayleigh and Love waves are not identical. If the rotation is then applied after the cross-correlation, the spectral whitening allows for leakage of Love-wave energy to the radial cross-correlation, and Rayleigh-wave energy to the transverse cross-correlation. This effect is quantified for the geophone combination shown in Figure 2.13.

For rotations to components *RR*, *RT*, *TR* and *TT*, the differences are largest, because the rotations are carried out in two steps using combinations of components *NN*, *NE*, *EN* and *EE*. Still, the phase differences are minimal, and the differences in amplitude are acceptable. The same applies for components *RZ*, *TZ*, *ZR* and *ZT*, in which only one rotation step is applied and where the differences are smaller. Component *ZZ* does not require a rotation and is therefore not affected by the processing order.

Furthermore, for the purpose of velocity variation estimation, leakage of Rayleigh and Love wave energy to orthogonal components is not relevant, because the direct wave is not used. In arrivals of (multiply) reflected surface waves i.e., surface waves that have reflected multiple times, leakage takes place anyway. Therefore, in this study, we did not apply rotation until after cross-correlation.

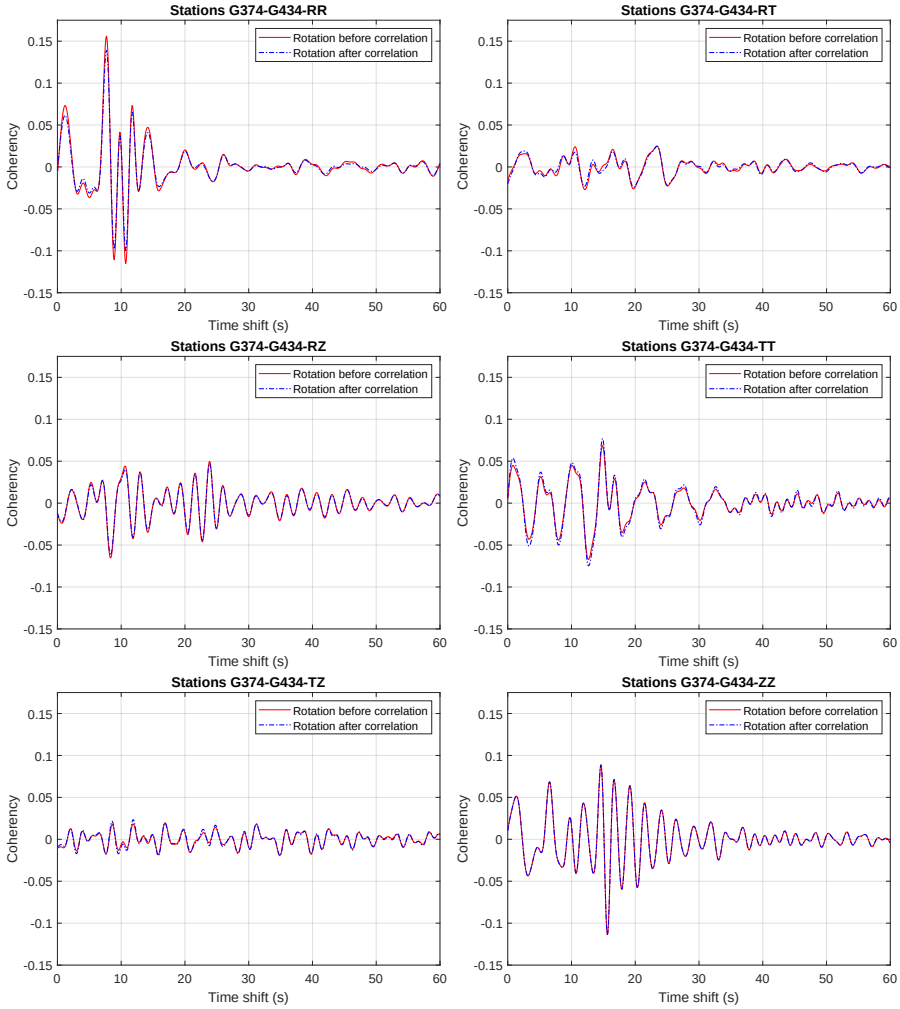

Figure 2.13: Comparison of applying rotation before or after cross-correlation using spectral normalization, for different component combinations, for receiver pair G374-G434.

3

4D Physics-Based Pore Pressure Monitoring Using Passive Image Interferometry

Abstract

This chapter introduces a technique for four-dimensional pore pressure monitoring using passive image interferometry. Surface-wave velocity changes as a function of frequency are directly linked to depth variations of pore pressure changes through sensitivity kernels. We demonstrate that these kernels can be used to invert time-lapse seismic velocity changes, retrieved with passive image interferometry, for hydrological pore pressure variations as a function of time, depth, and region. This new approach is applied in the Groningen region of the Netherlands. We show good recovery of pore pressure variations in the upper 200 m of the subsurface from passive seismic velocity observations. This depth range is primarily limited by the reliable frequency range of the seismic data.

The content of this chapter was published as: Fokker, E., Ruigrok, E., Hawkins, R., & Trampert, J. (2023). 4D physics-based pore pressure monitoring using passive image interferometry. *Geophysical Research Letters*, *50*(5).

3.1. Introduction

Traditionally, seismic imaging of the shallow subsurface is done with active sources. Seismic or acoustic sources from explosives or airguns excite downwards propagating waves, of which the reflections can be used to map geologic interfaces. Over the last decades, however, we have seen a shift toward passive imaging and monitoring. Seismic signals that were initially considered noise (e.g., microseisms) are now used to acquire subsurface data (e.g., Curtis et al., 2006).

Passive image interferometry (Sens-Schönfelder & Wegler, 2006) allows us to estimate seismic velocity changes using measurements of seismic ambient noise. This method consists of two steps. First, approximate Green's functions are estimated using cross-correlations of seismic noise measured at two receivers. This is referred to as seismic interferometry (Wapenaar et al., 2010a). Second, velocity changes as a function of time are retrieved by comparing the coda of time-lapse cross-correlations to a reference. This step is referred to as coda wave interferometry (Lobkis & Weaver, 2003; Snieder, 2006). With passive image interferometry, a single lapse cross-correlation is generally constructed from noise measurements with a duration of a few hours to a few weeks, while the reference cross-correlation is often an average over one to a few years. The relative difference in arrival times dt/t then represents the relative velocity change $dv/v = -dt/t$ with respect to the average reference velocity.

Seismic velocity variations have been empirically linked to many physical processes or observations, including temperature variations (e.g., Bièvre et al., 2018; Colombero et al., 2018; Richter et al., 2014), earthquake stress release (e.g., Brenguier et al., 2008a; Sleeman & de Zeeuw-van Dalfsen, 2020; Wegler & Sens-Schönfelder, 2007), and hydrological stress fluctuations (e.g., Andajani et al., 2020; Clements & Denolle, 2018). For instance, Illien et al. (2022) used seismic velocity change and an empirical link with a hydrological model to find short-term permeability increases directly after earthquakes. Such empirical relationships can give very useful insights in the processes causing velocity changes, provided the empirical relationship reflect the physical processes involved. Therefore, we prefer a more physics-based approach.

Recently, Fokker et al. (2021) provided a physical model for pore pressure monitoring using surface-wave phase-velocity changes. Building on the theory of Tromp and Trampert (2018), hey showed that pore pressure changes induce shear-wave velocity variations through changes in effective stress. Using surface-wave dispersion modeling (Hawkins, 2018), they showed that pore pressure changes explain the measured phase-velocity changes both in phase and amplitude.

In the current study, we demonstrate that measured velocity changes can be inverted for pore pressure variations as a function of time and space. We introduce pore pressure sensitivity kernels for surface-wave phase-velocity changes, and compute velocity variations by applying passive image interferometry to seismic ambient noise measurements in Groningen, the Netherlands. An inversion of these velocity changes results in models of pore pressure variation as a function of time, depth and region. Different regions of Groningen show a different temporal behavior that coincide with the jurisdictions of two independent water boards.

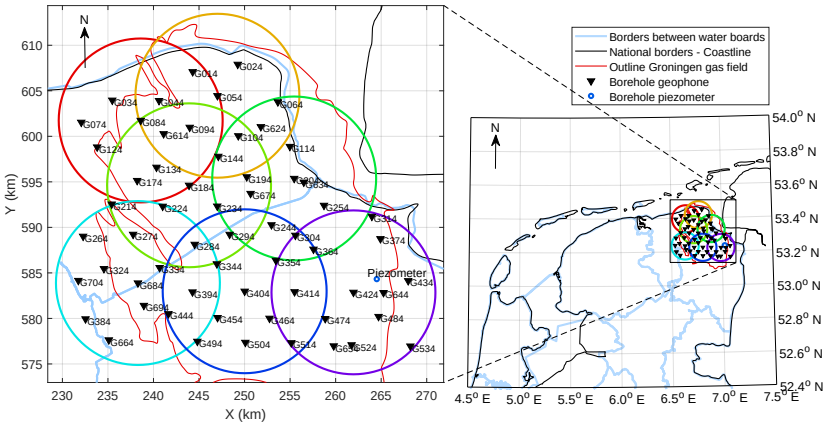

Figure 3.1: Map view of the locations of the measurement equipment employed in this study. The black triangles indicate borehole geophones at a depth of 200 m (KNMI, 1993) and the blue point indicates a borehole piezometer (Dinoloket, 2022). Different regions are indicated by circles. The color coding is used in Figures 3.3, 3.5 and 3.8-3.11 to distinguish regional results. The outline of the Netherlands and the Groningen gas field are shown as black and red lines, while the borders between different water boards are shown in light blue.

3.2. Groningen Setting, Data and Models

The Groningen region in the Netherlands has been studied extensively in the context of induced seismicity (e.g., Bourne et al., 2018; Hettema et al., 2017; Nepveu et al., 2016; Trampert et al., 2022) and subsidence (e.g., van der Wal & van Eijs, 2016; van Thienen-Visser et al., 2015; van Thienen-Visser & Fokker, 2017). The installation of a large dense network of borehole geophones (Dost et al., 2017) enabled intensive research activity. Seismic measurements on multiple depth levels were used to estimate shallow 1D velocity and attenuation profiles (Hofman et al., 2017; Ruigrok et al., 2022) and to estimate soil amplifications (van Ginkel et al., 2019), while the large azimuthal coverage of the network was used to test different quality assessment parameters for passive image interferometry (Fokker & Ruigrok, 2019). The great amount of geological and geophysical models, provided by previous studies, and the presence of the large seismic network make Groningen an ideal region to test our approach of physics-based pore pressure monitoring.

The Groningen region can be divided into water board Noorderzijlvest in the northwest and water board Hunze en Aa's in the southeast. The borders between different water boards are shown in Figure 3.1 in light blue. Different water boards in the Netherlands can have different policies regarding groundwater management, and thus the pore pressure variations may be region dependent. In the southeastern region, at the location shown in Figure 3.1 as the blue dot, a deep borehole piezometer (Dinoloket, 2022) takes direct continuous measurements of the pore pressure at multiple depth levels up to 170 m. Shallow direct measurements of pore pressure variation can be found throughout the whole region (Grondwatertools, 2022).

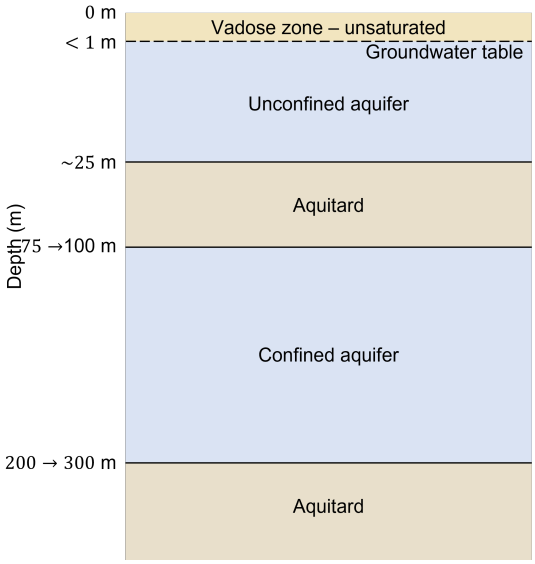

Figure 3.2: Schematic overview of the hydrologic layering. An unconfined aquifer occupies the first 25 m, where the groundwater table is situated at a depth smaller than 1 m. An aquitard comprised of impermeable clay layers spans from 25 m to roughly 75-100 m depth. A confined aquifer is situated between 75-100 m and 200-300 m depth.

Hydrologically, we can classify the shallow subsurface in the Groningen area roughly into three layers (Figure 3.2). An unconfined aquifer occupies the first 25 m depth. Pore pressure variations within this layer are a direct result of changes in the groundwater table. An aquitard is situated from 25 m to roughly 75-100 m depth, spanning the entire region with only sparse openings. Due to the low permeability of this clay layer, pore pressure diffusion cannot fully penetrate this layer and hence we do not expect large seasonal pore pressure variations. A confined aquifer can be found below the clay from 75-100 m to 200-300 m depth. The pore pressure in this layer is determined by the groundwater table at the recharge locations. Therefore, the spatial pore pressure variability is expected to be small within this layer.

From the seismic network in Groningen (Dost et al., 2017) we use data from the 4.5 Hz borehole geophones at 200 m depth at the locations shown in Figure 3.1 by the black triangles. We chose the deepest geophones from the borehole network, because they register the highest power of coherent noise from distant sources, compared to the power of incoherent noise from close sources. Each colored circle indicates a subregion that is investigated. For each subregion we gather shear-wave velocity and density models from Kruiver et al. (2017a) and a compressional-wave velocity model from Romijn (2017). From these models we computed all elastic parameters needed in this study (Figure 3.3).

The models for compressional-wave velocity, shear-wave velocity and density (Figure 3.3a-c) allow us to compute the bulk modulus, the shear modulus and the confining pressure (Figure 3.3d-f). The pressure derivative of the shear modulus,

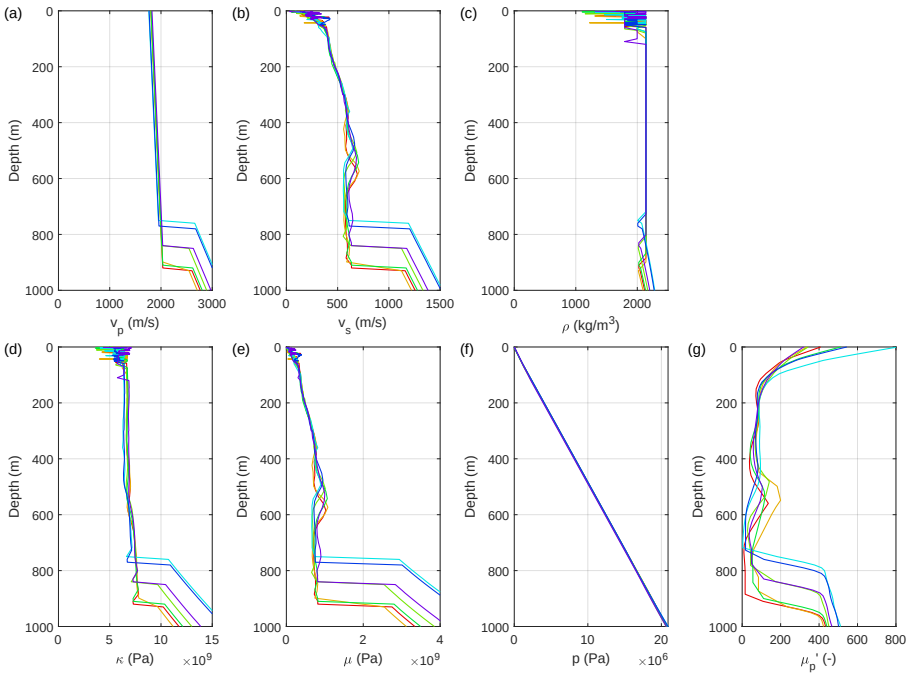

Figure 3.3: Elastic models from Kruiver et al. (2017a) and Romijn (2017) for the regions indicated by the colored circles in Figure 3.1: (a) Compressional-wave velocity v_p, (b) shear-wave velocity v_s, (c) mass density ρ, (d) bulk modulus $\kappa = \rho v_p^2 - \frac{4}{3}\rho v_s^2$, (e) shear modulus $\mu = \rho v_s^2$, (f) confining pressure $P = \int_0^z \rho(z) g \, dz$, with g the gravitational acceleration and z the depth below surface, and (g) pressure derivative of the shear modulus $\mu_p' = d\mu/dp$, based on the smoothed derivative of the shear modulus with respect to confining pressure.

needed for the sensitivity kernel, can be computed by a pointwise derivative of the shear modulus with respect to the confining pressure. At layer interfaces, however, the shear modulus can change abruptly due to a change in material from one layer to another. This will result in an unrealistic estimate for its pressure derivative. A smoothing operation with a robust weighing function and positivity constraint removes outliers that occur at such a layer intersection. Figure 3.3g shows our model for the pressure derivative of the shear modulus $d\mu/dp$ at the center of the corresponding region.

3.3. Passive Image Interferometry

To compute seismic velocity changes we apply passive image interferometry (Sens-Schönfelder & Wegler, 2006) to seismic ambient noise measured in Groningen, the Netherlands. This method consists of two processes. First, the Green's function between two seismic receivers is estimated using cross-correlations of ambient seismic noise. Second, time-lapse variations in arrival times are identified, corresponding to velocity variations.

To estimate the Green's function for one lapse period, we compute the cross-coherence of seismic noise, recorded by seismic receivers at locations x_A and x_B. The cross-coherence represents the spectrally normalized cross-correlation, and can be computed in the frequency domain (Wapenaar et al., 2010b):

$$\hat{H}(x_B, x_A, \omega) = \frac{\hat{w}(x_B, \omega)\,\hat{w}^*(x_A, \omega)}{|\hat{w}(x_B, \omega)||\hat{w}(x_A, \omega)|}. \tag{3.1}$$

where w is ground velocity. The frequency domain is indicated by a hat and the star denotes a complex conjugation. We stack cross-coherences calculated from 50% overlapping time windows of 20 min duration, where the first time window ranges from 0:00 to 0:20 UTC, the second from 0:10 to 0:30 UTC, etc., for a lapse period of 21 days. We repeat this procedure for lapse periods between 01 January 2017 and 01 January 2020. The cross-coherences are computed for vertical components. Figure 3.4 shows an example of cross-coherences in the time domain as a function of date, for receiver combination G014-G104 in the orange region (Figure 1) and frequency range [1.3 1.6] Hz.

We then determine velocity changes using the stretching method in the time domain (Lobkis & Weaver, 2003). Relative velocity changes $dc/c = \epsilon$ are found at the maximum correlation coefficient $CC(\epsilon)$ between lapse cross-coherence H_{lapse}, stretched in time with factor $(1-\epsilon)$, and reference cross-coherence H_{ref},

$$CC(\epsilon) = \frac{\int_{t_1}^{t_2} H_{\text{lapse}}[t(1-\epsilon)]\,H_{\text{ref}}[t]\,dt}{\sqrt{\int_{t_1}^{t_2} \left(H_{\text{lapse}}\right)^2[t(1-\epsilon)]\,dt}\sqrt{\int_{t_1}^{t_2} \left(H_{\text{ref}}\right)^2[t]\,dt}}. \tag{3.2}$$

The reference cross-coherence is defined as the 3-year average from 01 January 2017 0:00 UTC to 01 January 2020 0:00 UTC, hence the retrieved velocity change is relative to the average within this period.

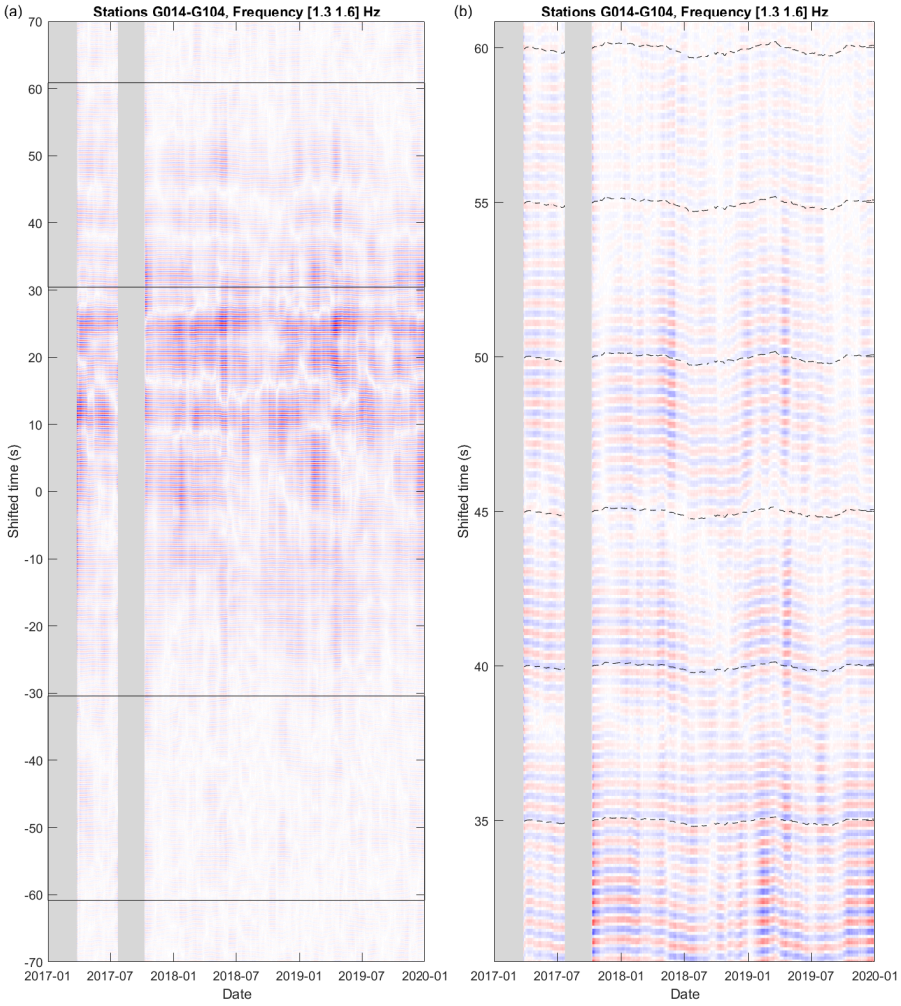

Figure 3.4: Cross-coherence of seismic noise recorded at receivers G014 and G104 at frequency range [1.3 1.6] Hz. (a) Cross-coherence for shifted times between -70 and +70 seconds, indicating in black the time-window used to retrieve relative velocity changes. (b) Zoomed cross-coherence at the causal time window plotted in (a), showing consistent arrivals up to 60 seconds. The black dashed curves indicate waveform stretching for which the correlation with the reference is highest (Equation 3.2). This corresponds to the relative velocity variations between receivers G014 and G104. For this particular receiver pair, the anti-causal part is weak in this frequency range.

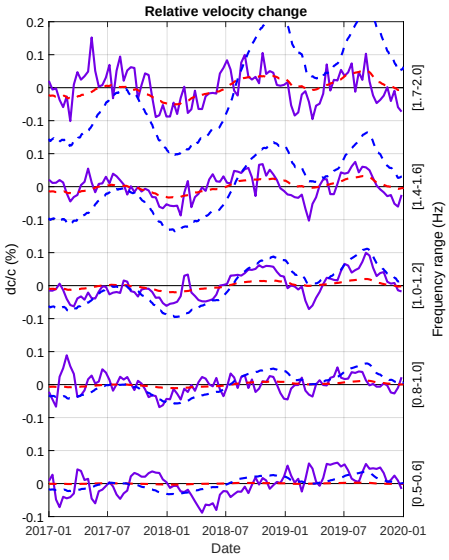

Figure 3.5: Models and observations of seismic velocity changes for the region indicated in Figure 3.1 in purple. The purple curves represent the velocity changes for six frequency ranges estimated using passive image interferometry (Sens-Schönfelder & Wegler, 2006) on the vertical components, while the red and the blue dashed curves show respectively the fundamental mode Rayleigh- and Love-wave velocity changes as modeled (Fokker et al., 2021) from pore pressure observations at the borehole piezometer (Fig. 3.1, blue point; Dinoloket, 2022).

The coda of the cross-correlation is more likely to contain stable parts of the Green's function, because this only requires a stable background noise structure (Hadziioannou et al., 2009), while direct waves also require well-illuminated Fresnel zones (Wapenaar et al., 2010a). For this reason, we omit all arrivals of direct waves, and choose our time windows (integration boundaries in Equation 3.2) for the cross-coherence as $\tau < |t| < 2\tau$, where $\tau = (x/v_{low} + 5)$ s. v_{low} is the fundamental-mode Rayleigh wave phase velocity in the model of Figure 3.3a-c. An additional 5 s is added to exclude the direct Rayleigh waves with more certainty. This narrow window excludes most body waves in the coda and should mainly leave closely scattered surface waves.

The cross-coherences are filtered with a bandpass filter before we estimate the velocity change for the chosen frequency range. To obtain velocity variations as a function of frequency range, we repeat this process for multiple frequency ranges. We compute an average velocity change for the regions indicated by the circles in Figure 3.1, using all receivers pairs within the indicated circles. This also allows us to compute the standard deviation of the sampling distribution of velocity change $\sigma_{dv/v} = \sigma/\sqrt{n}$, as an indication of the measurement uncertainty on the one hand, and the intrinsic variability over a region on the other hand.

We use the coda of the cross-coherence evaluated for the vertical components to estimate velocity changes. Likely, the velocity changes are caused by fundamental-mode Rayleigh waves, but contributions from higher modes, Love

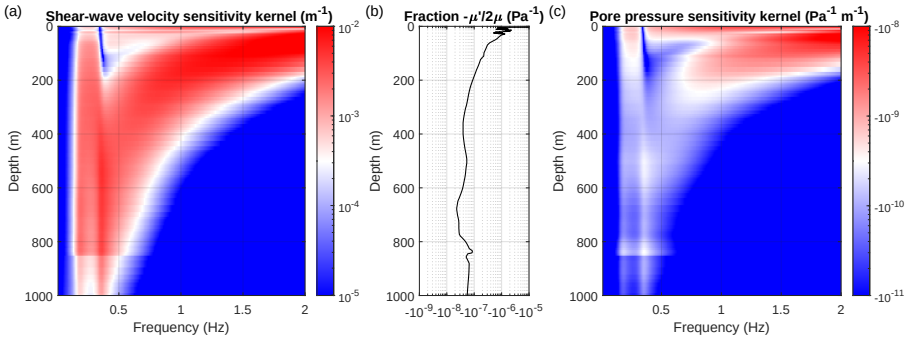

Figure 3.6: Visualization of Equation 3.6: (a) shear-wave sensitivity kernel $K^R_{v_s}(\omega, z)$ for Rayleigh-wave phase velocity, computed using the adjoint method (Hawkins, 2018) on models for compressional-wave velocity, shear-wave velocity and density (Figure 3.3a-c; purple), (b) fraction $-\mu'_p(z)/2\mu(z)$ where μ is the shear modulus and μ'_p is the pressure derivative of the shear modulus (Figure 3.3e,g; purple), and (c) pore pressure sensitivity kernel $K^R_u(\omega, z)$, which is a multiplication of figures (a) and (b). Note that the amplitude axes show logarithmic scales.

and body waves cannot a-priori be excluded. We repeat the approach of Fokker et al. (2021) to find what type of waves is the main contributor to the observed velocity change by making a forward calculation for the region containing the piezometer. Figure 3.5 shows velocity changes for five frequency ranges, retrieved using passive image interferometry (purple), and fundamental-mode phase-velocity changes for Rayleigh (red dashed) and Love (blue dashed) waves, modeled from the pore pressure variations measured by Dinoloket (2022). The velocity variations closely resemble fundamental-mode Rayleigh-wave velocity changes. Therefore, we treat the velocity changes measured on the vertical components as fundamental-mode Rayleigh-wave phase-velocity changes. We tried the same modeling with a Voigt average of Love and Rayleigh (Fokker et al., 2021), but this degraded the fit to the piezometer data.

3.4. Pore Pressure Sensitivity Kernels

To connect Rayleigh-wave phase-velocity change to pore pressure variation, we combine the physics-based relationship derived by Fokker et al. (2021) with shear-wave sensitivity kernels to construct pore pressure sensitivity kernels. Building on Tromp and Trampert (2018), Fokker et al. (2021) derived that a change in pore pressure du via effective stress induces shear-wave velocity change

$$\frac{dv_s}{v_s} = -\frac{\mu'_p}{2\mu} du, \tag{3.3}$$

with shear-wave velocity v_s, shear modulus μ, and pressure derivative of the shear modulus $\mu'_p = d\mu/dp$. A positive change in pore pressure thus results in a negative change in shear-wave velocity.

Changes in the shear-wave velocity directly induce surface-wave phase-velocity changes

$$\frac{dc}{c}(\omega) = \int_0^\infty K_{v_s}(\omega, z)\frac{dv_s}{v_s}(z)dz, \tag{3.4}$$

with surface-wave phase velocity c, and shear-wave sensitivity kernel K_{v_s}. We can now substitute Equation 3.3 in 3.4, resulting in

$$\frac{dc}{c}(\omega) = \int_0^\infty K_u(\omega, z)du(z)dz, \tag{3.5}$$

where

$$K_u(\omega, z) = -\frac{\mu_p'(z)}{2\mu(z)}K_{v_s}(\omega, z) \tag{3.6}$$

represents the pore pressure sensitivity kernel for surface-wave phase velocity.

Shear-wave sensitivity kernels for surface-wave phase velocity can be calculated using the adjoint method (Hawkins, 2018) together with one-dimensional models for compressional-wave velocity v_p, shear-wave velocity v_s, and density ρ. Figure 3.6a shows the shear-wave sensitivity kernel for Rayleigh-wave phase velocity for the region centered at receiver G424 (purple region in Figure 3.1), constructed from the elastic model shown in Figure 3.3a-c. The fraction $-\mu_p'/2\mu$ shown in Figure 3.6b is calculated using the shear modulus and its pressure derivative (Figure 3.3e and 3.3g). In accordance with Equation 3.6, we multiply Figures 3.6a and 3.6b to obtain the pore pressure sensitivity kernel shown in Figure 3.6c.

3.5. Inversion for Pore Pressure Variation

To invert surface-wave velocity change for pore pressure variation as a function of depth and time, we need to discretize the linear relation described by Equation 3.5. We expand pore pressure change du as

$$du(z, t_k) = \sum_j S_j(z)m_j(t_k), \tag{3.7}$$

where function $S_j(z)$ is chosen to be a cubic natural spline function, and $m_j(t_k)$ its coefficients at time t_k, which is the center of the 21 day lapse period (Section 3.3). We then rewrite Equation 3.5 as

$$\frac{dc}{c}(\omega_i, t_k) = \sum_j \int_0^\infty K_u(\omega_i, z)S_j(z)dz\, m_j(t_k). \tag{3.8}$$

For each lapse time t_k, this can be written as a linear forward problem,

$$\boldsymbol{d}(t_k) = \boldsymbol{G}\boldsymbol{m}(t_k), \tag{3.9}$$

where

$$d_i(t_k) = \frac{dc}{c}(\omega_i, t_k) \tag{3.10}$$

represents the data,

$$G_{ij} = \int_0^\infty K_u(\omega_i, z) S_j(z) dz \tag{3.11}$$

the forward operator, and $m_j(t_k)$ the model coefficients of the pore pressure change.

Model coefficients $m_j(t_k)$ can be retrieved using the explicit least-squares formulation (Tarantola, 2005),

$$\tilde{\boldsymbol{m}}(t_k) = \left(\boldsymbol{G}^T \boldsymbol{C}_{\boldsymbol{d}}^{-1}(t_k)\boldsymbol{G} + \boldsymbol{C}_{\boldsymbol{m}}^{-1}\right)^{-1} \boldsymbol{G}^T \boldsymbol{C}_{\boldsymbol{d}}^{-1}(t_k)\boldsymbol{d}(t_k), \tag{3.12}$$

with data covariance $\boldsymbol{C_d}$ and prior model covariance $\boldsymbol{C_m}$. Based on the pressure head measurements in the southeastern region we expect a variance in pore pressure of 10^6 Pa^2, hence we choose the model covariance as $\boldsymbol{C_m} = 10^6 \boldsymbol{I}$, where $\boldsymbol{I}$ represents the identity matrix. Since we are interested in the mean velocity change $dv/v(\omega_i, t_k)$ per region, we define the data covariance as the variance in the set of cross-coherences per region (see Figure 3.7a, error bars). We note that this variance can reflect the cross-coherence variability per region and/or direct observational uncertainty. We therefore use

$$\boldsymbol{C_d}(t_k) = \mathrm{diag}\left(\boldsymbol{\sigma_{dv/v}}(t_k)\right)^2. \tag{3.13}$$

The resolution $\boldsymbol{R}(t_k)$ of the inverted model representation $\tilde{\boldsymbol{m}}(t_k)$ can be obtained by substituting the data $\boldsymbol{d}$ in Equation 3.12 for the forward operator $\boldsymbol{G}$,

$$\boldsymbol{R}(t_k) = \left(\boldsymbol{G}^T \boldsymbol{C}_{\boldsymbol{d}}^{-1}(t_k)\boldsymbol{G} + \boldsymbol{C}_{\boldsymbol{m}}^{-1}\right)^{-1} \boldsymbol{G}^T \boldsymbol{C}_{\boldsymbol{d}}^{-1}(t_k)\boldsymbol{G}, \tag{3.14}$$

and the posterior model covariance can be found by

$$\boldsymbol{C}_{\tilde{\boldsymbol{m}}}(t_k) = \left(\boldsymbol{G}^T \boldsymbol{C}_{\boldsymbol{d}}^{-1}(t_k)\boldsymbol{G} + \boldsymbol{C}_{\boldsymbol{m}}^{-1}\right)^{-1}. \tag{3.15}$$

After inversion for model representation $m_j(t_k)$, we repeat the process for all lapse times t_k, and compute our final model for pore pressure variation using Equation 3.7.

Figure 3.7 shows the steps in the inversion scheme for the region centered at receiver G424 (purple region in Figure 3.1). Velocity changes retrieved using passive image interferometry form the data of this inversion (Figure 3.7a, error bars; two example frequency ranges). We use velocity variations of multiple frequency ranges with varying center frequency and frequency span (Figure 3.7b), and we define 10 spline functions S_j (Figure 3.7c). Following Equation 3.11, we construct forward operator G_{ij} (Figure 3.7d). Figure 3.7e shows pore pressure variations as retrieved using Equations 3.12 and 3.7, and Figure 3.7f shows the posterior model covariance as computed using Equation 3.15. The uncertainty of the retrieved model can

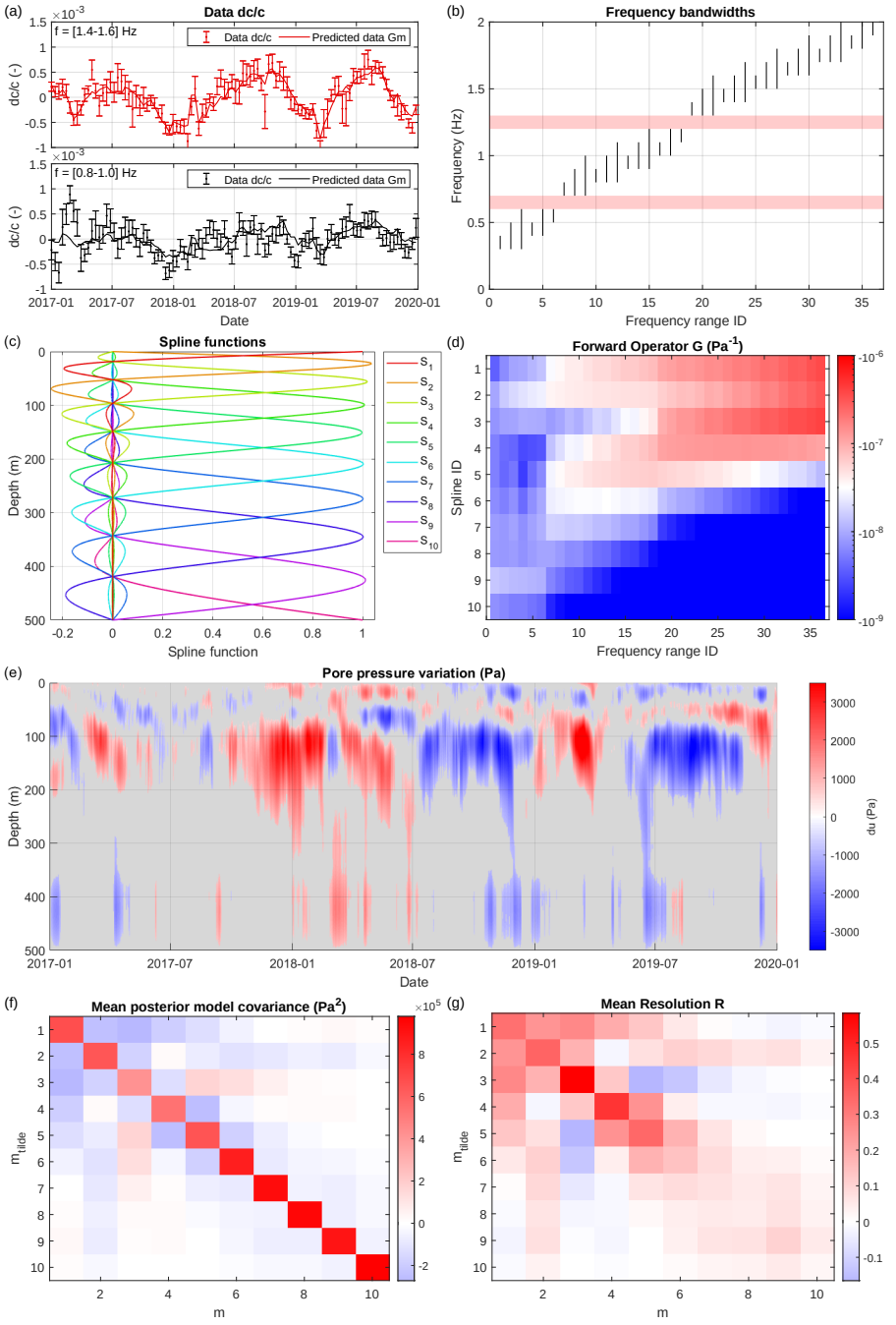
(a)
Data dc/c
f = [1.4-1.6] Hz
Data dc/c
Predicted data Gm
dc/c (-)
f = [0.8-1.0] Hz
2017-01
2017-07
2018-01
2018-07
2019-01
2019-07
2020-01
Date
(b)
Frequency bandwidths
Frequency (Hz)
Frequency range ID
(c)
Spline functions
Depth (m)
Spline function
(d)
Forward Operator G (Pa-1)
Spline ID
Frequency range ID
(e)
Pore pressure variation (Pa)
Depth (m)
Date
du (Pa)
(f)
Mean posterior model covariance (Pa2)
mtilde
m
(g)
Mean Resolution R
mtilde
m

Figure 3.7

Figure 3.7: Inversion scheme for retrieving pore pressure variations: (a) seismic velocity changes as a function of time for two example frequency ranges, obtained using passive image interferometry (error bars), and predicted based on the inferred pore pressure model and the forward operator (solid lines), (b) all frequency ranges between 0.3 and 2 Hz for which velocity changes are computed, the frequencies in the pink band are excluded (see text), (c) 10 spline functions used to discretize pore pressure variations, (d) discretized pore pressure sensitivity kernel (i.e., forward operator G_{ij} in Equation 3.11, with spline functions as in (c), for the frequency ranges shown in (b)), (e) final model for pore pressure change as function of time and depth in accordance with Equations 3.12 and 3.7, (f) the posterior model covariance in accordance with Equation 3.15, and (g) resolution matrix in accordance with Equation 3.14.

then be computed using the square root of the diagonal of the posterior model covariance. Pore pressure changes smaller than this uncertainty are colored gray in Figure 3.7e. The resolution matrix is computed using Equation 3.14 (Figure 3.7g), indicating that there is only sufficient resolution to confidently infer the model coefficients corresponding to the first six splines. Therefore, pore pressure variations can only be retrieved at depths smaller than about 200 m. The resolution matrix shows that deeper pore pressure models have contributions from splines 2 and 6-10, and are thus smeared out over a large depth range. To show how well the pore pressure model explains the velocity variations, we use Equation 3.9, the forward operator $\boldsymbol{G}$, and the inferred pore pressure model $\tilde{\boldsymbol{m}}$ to predict the data. Figure 3.7a (solid lines) shows the result.

We construct a four-dimensional pore pressure model by repeating the inversion procedure for all regions shown in Figure 3.1. We compute velocity changes (Fig 3.8a shows five example frequencies) and construct pore pressure sensitivity kernels based on the elastic parameters shown in Figure 3.3. The inversion leads to pore pressure models as a function of time, depth and region. Figure 3.8b shows in purple the inferred model in the region centered at receiver G424 for five depths, compared to the independent direct measurements of pore pressure variation in black (Figure 3.1, blue point; Dinoloket, 2022). The four-dimensional model of pore pressure variations is illustrated in Figure 3.8c, where for five depth levels and seven dates the pore pressure is shown in a colored map view. Detailed comparisons between pore pressure models and comparisons with shallow independent piezometric measurements are shown in Figures 3.9 and 3.10. The comparison of shallow pore pressure models in the northwest and the southeast shows significant spatial variations, while lateral variations of deeper pore pressure models could not be classified as significant. The shallow pore pressure models also compare well in phase and amplitude to the direct independent measurements of pore pressure change. The relative misfit between velocity change measured using passive image interferometry and predicted based on the inferred pore pressure model is shown in Figure 3.11, indicating that measured velocity variations between 0.7 and 1.8 Hz are well explained by our pore pressure model. In the lower frequency ranges, that is, larger depths, the model does not explain the data, in agreement with the information displayed on the posterior covariance and resolution matrix.

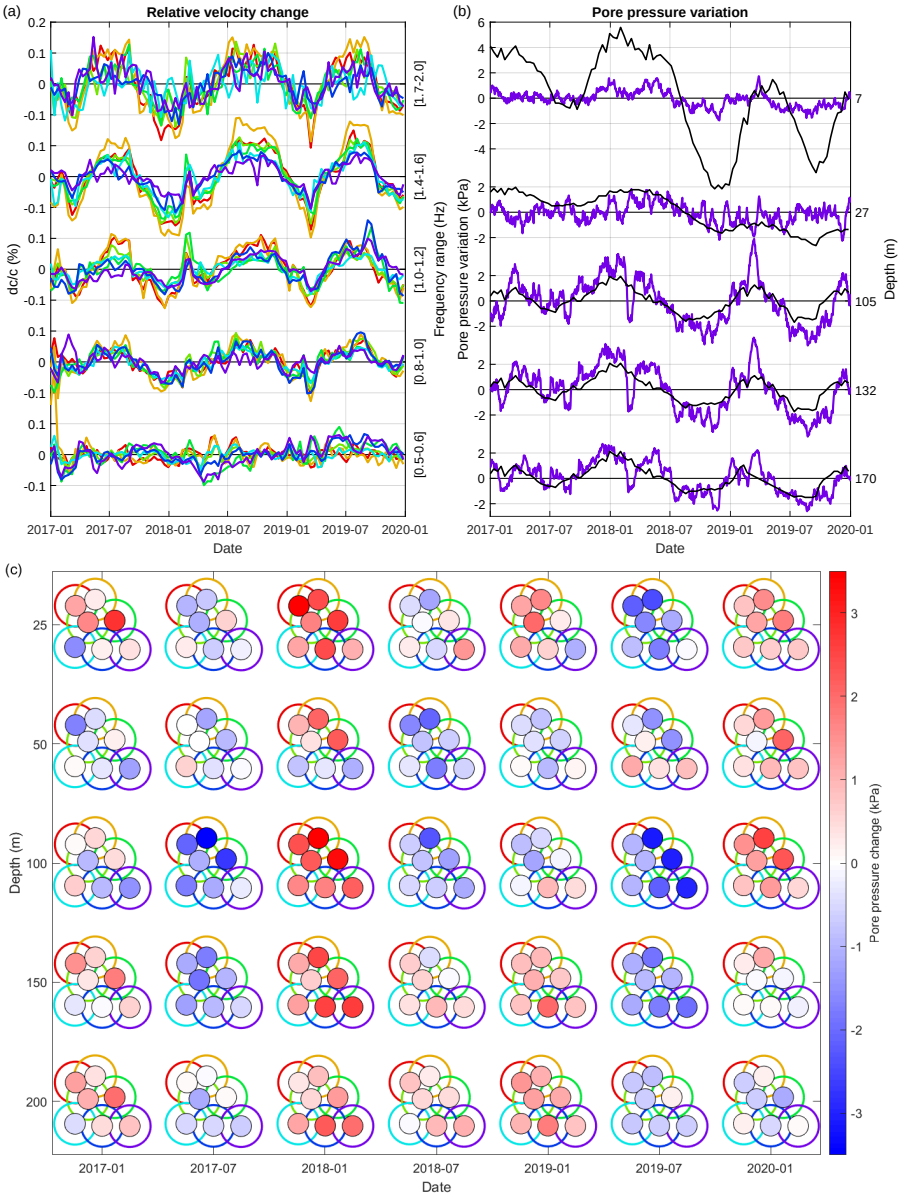

Figure 3.8: Four-dimensional variations in seismic velocity and pore pressure. The different colors indicate different regions, corresponding to the colors in Figure 3.1. (a) Seismic velocity change for five frequency ranges estimated using passive image interferometry (Sens-Schönfelder & Wegler, 2006) on the vertical components. (b) Inferred model for pore pressure variation in the region centered at receiver G424 for five depths. The black curves correspond to pore pressure measurements by the borehole piezometer indicated in Figure 3.1 as blue dot. (c) Map view of pore pressure models, as a function of time and depth. Each subplot corresponds to a certain time and depth, showing the pore pressure change as color for the seven different subregions presented in Figure 3.1.

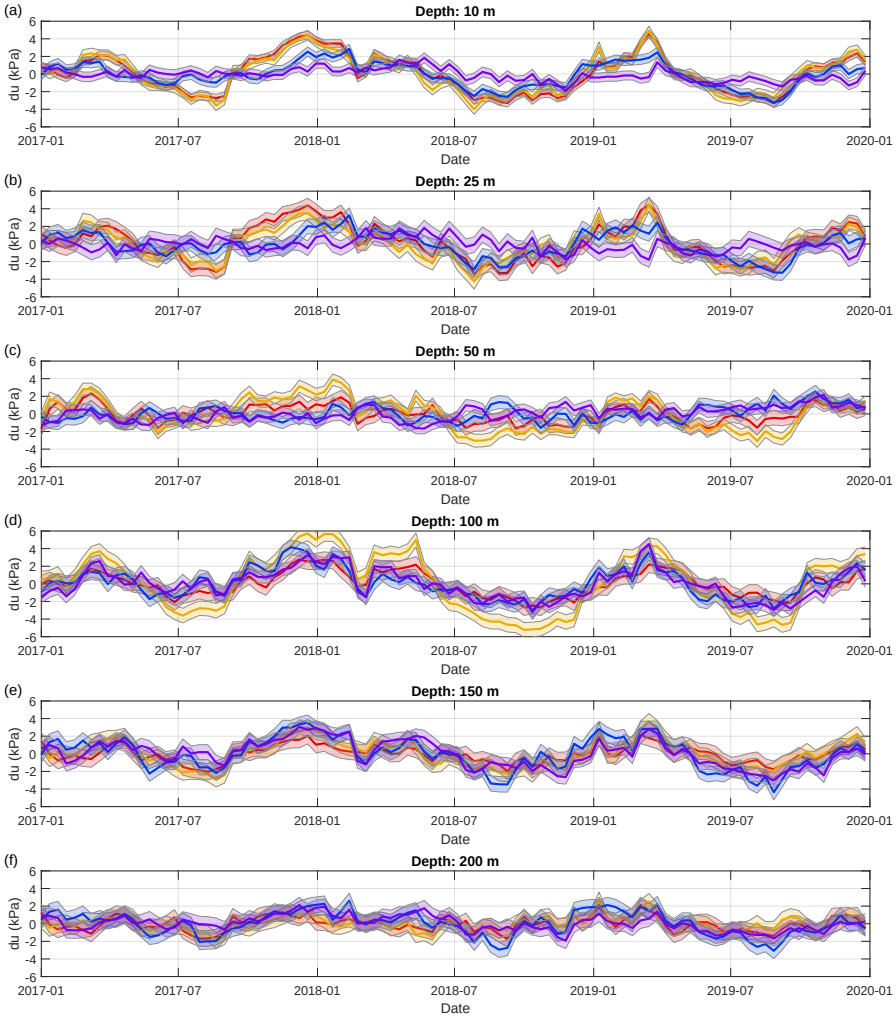

Figure 3.9: Comparison between pore pressure variations as modeled for different regions and depths. The pore pressure change has been modeled using Equations 3.12 and 3.7 (solid lines; colors correspond to regions in Figure 3.1), while the uncertainty range was modeled using the squareroot of the diagonal of the posterior model covariance (Equation 3.15; Figure 3.7f). The uncertainty ranges of the shallow models in the northwest and the southeast do not overlap, indicating a significant difference. Lateral variations of deeper pore pressure models, however, fall within the uncertainty and can therefore not be classified as significant.

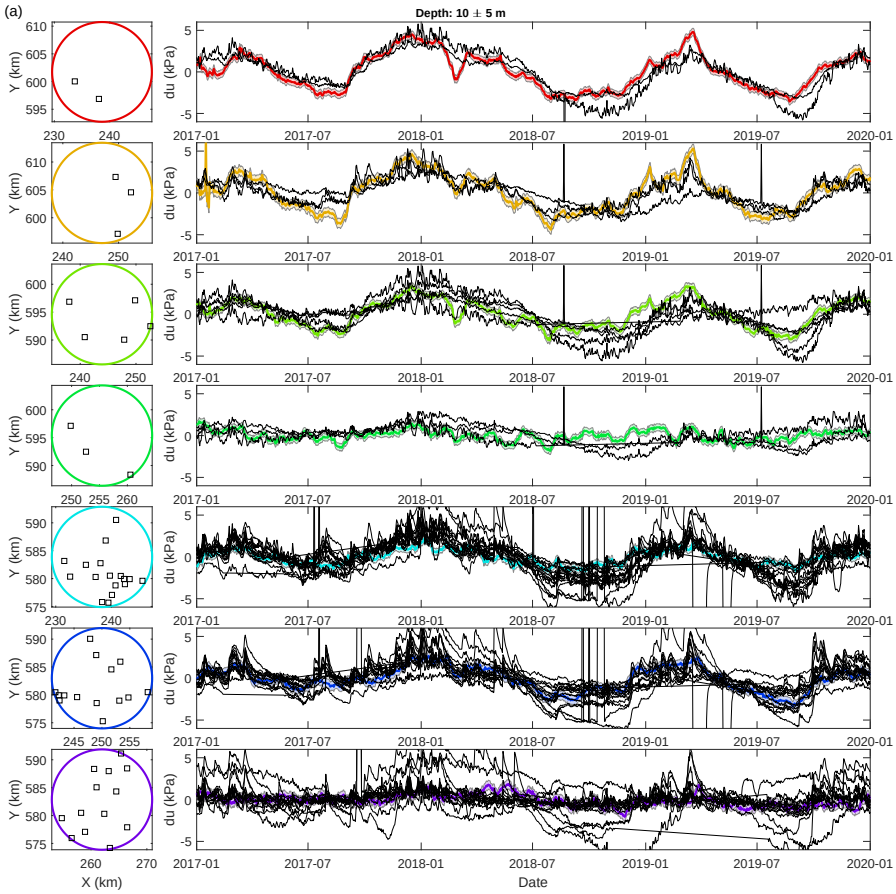

Figure 3.10: *Cont.*

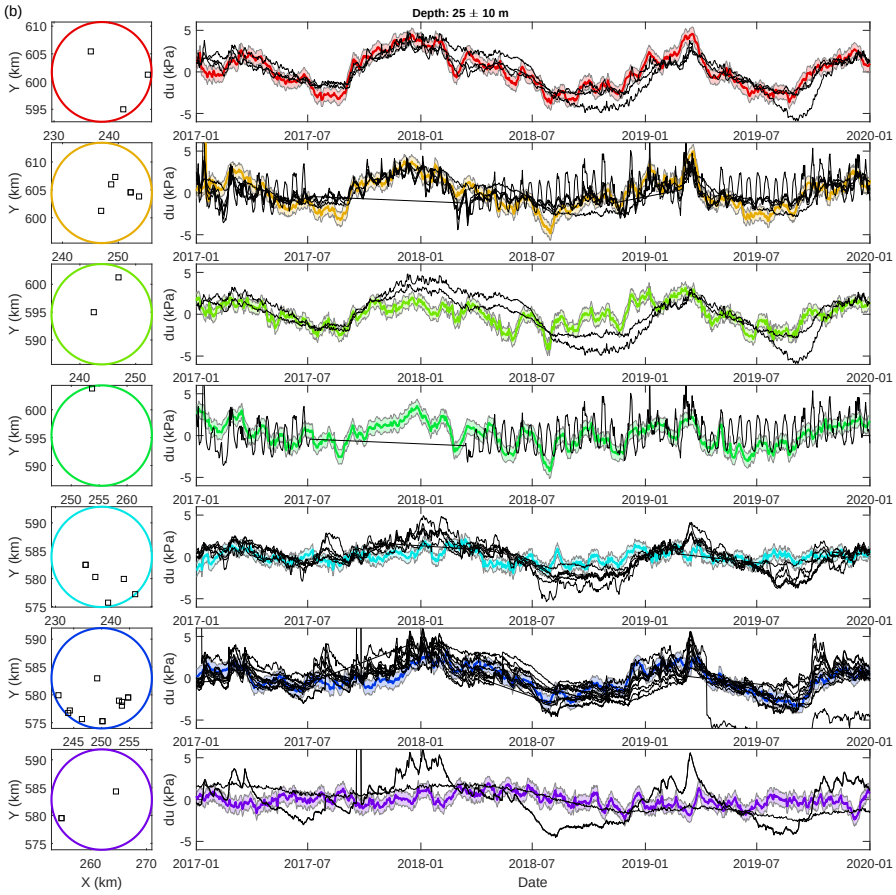

Figure 3.10: Comparison between pore pressure variations as modeled in this study and measured by local shallow piezometers (Grondwatertools, 2022). Left: Map views of separate regions in accordance with Figure 3.1, indicating locations of the piezometers as black squares. Right: Pore pressure variations as modeled in accordance with Section 3.5 for the region shown on the left, and measurements of pore pressure change (black) at the locations of the piezometers shown on the left. The pore pressure models are shown for depths of (a) 10 m and (b) 25 m, whereas the piezometric measurements are obtained (a) between 5 and 15 m depth and (b) between 15 and 35 m depth.

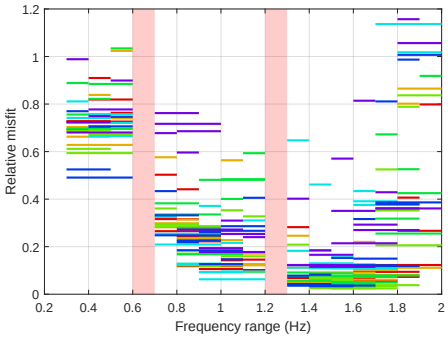

Figure 3.11: Relative misfit $\Phi = \frac{\sum_t (dv/v(\omega,t) - G\tilde{m}(\omega,t))^2}{\sum_t (dv/v(\omega,t))^2}$ between measured velocity change dv/v and predicted velocity change based on the inferred pore pressure model $G\tilde{m}$. The different colors correspond to the regions in Figure 3.1. The frequencies in the pink band were excluded.

3.6. Hydrologic Interpretation

The inferred pore pressure models reveal the characteristics of the hydrologic classification (Section 3.2, Figure 3.2).

Within the confined aquifer, pore pressure models compare well to the direct measurement in the southeast (Figure 3.8b) and models for the different regions are very similar to each other (Figure 3.9d-f). The seasonal trends show lower pore pressures during summers and higher pore pressures during winters. The source for pore pressure change in this lower layer is due to locations where the clay layer is absent or very thin and pore pressure diffusion can reach this aquifer. Therefore, the pore pressure in this aquifer represents groundwater fluctuations at the recharge locations.

Within the aquitard, we observe small pore pressure variations that show neither a clear seasonal pattern, nor consistency over the different regions. Within this layer we expect much smaller pore pressure variations, because the hydraulic conductivity in the order of 1 mm per day is too low for pore pressure diffusion to reach the core of this layer. In the inversion process, pore pressure variations must therefore have leaked from depths corresponding to neighboring splines. The resolution in Figure 3.7g shows that this is possible.

Within the unconfined aquifer, pore pressure variations are a direct result of the changing groundwater table. Changes in the groundwater table are very site dependent, since their sources (i.e., precipitation, topography, groundwater extraction, and groundwater management) can vary from region to region. Interestingly, there is a significant (Figure 3.9) difference in amplitude between shallow pore pressure variations in the southeast (purple and blue areas) and the northwest (red and orange areas). Independent shallow piezometric measurements of the pore pressure (Grondwatertools, 2022) show for this aquifer an amplitude increase in seasonal variations from the southeast to the northwest. The amplitude differences between the regions coincide with the jurisdictions of two different water boards that may have different policies for groundwater management. The mismatch between shal-

low pore pressure models and the direct measurements shown in Figure 3.8b can potentially be explained by local topography or the presence of clay, since the direct measurements are taken at a point location, while the models represent an average over a lateral area of 250 km^2. The spatial variability shown by other pore pressure measurements from this region (purple area in Figure 3.10) supports this hypothesis. Other shallow pore pressure measurements (Grondwatertools, 2022) show closer agreement with the shallow models (Figure 3.10).

3.7. Discussion

In this study we obtained seismic velocity changes using the stretching method (Lobkis & Weaver, 2003). However, Zhan et al. (2013) showed that varying amplitudes in the noise can lead to spurious velocity changes. This is what we observe at frequency ranges containing the frequencies of 0.63 or 1.24 Hz, which are eigenfrequencies of nearby wind turbines (van der Vleut, 2019). With varying wind direction, the swinging direction of the wind-turbine masts changes and therefore the directions, into which Rayleigh and Love waves are excited, will change. This causes substantial amplitude variations and hence spurious velocity changes. For this reason we excluded all frequency ranges containing these eigenfrequencies.

The advantage of the stretching method mostly lays in the ability to detect weak velocity changes using low signal-to-noise ratios. However, it makes use of the assumption of homogeneous velocity change. Using this method we can therefore only retrieve an average velocity change over a relatively large region. Alternatively, one could estimate velocity change using the moving window cross-spectral method (Clarke et al., 2011; James et al., 2017), dynamic time warping (Mikesell et al., 2015), or the wavelet method (Mao et al., 2020). These methods can be used for a higher-resolution spatial inversion of velocity change, taking into account the sensitivities of different wave types at different arrival times and frequencies (James et al., 2019; Mao et al., 2022; Margerin et al., 2016; Obermann et al., 2013b).

By using the coda of the cross-correlations of vertical components close after the arrival of the fundamental-mode Rayleigh wave, we excluded most Love-wave energy. If the ratio of Love to Rayleigh energy were known in the Groningen area, one would be able to add velocity change measured on the horizontal components (i.e., RR, RT, TR, TT). The pore pressure sensitivity kernels for Rayleigh and Love would need to be averaged accordingly. A Voigt average between Rayleigh and Love as used by Fokker et al. (2021) would be too rough an approximation for pore pressure inversion, since the ratio of Love to Rayleigh energy varies as a function of frequency (Juretzek & Hadziioannou, 2016).

Velocity changes are linked to pore pressure variations through pore pressure sensitivity kernels. To compute these kernels for Rayleigh-wave velocity change, we determined pressure derivatives of the shear modulus by a point-wise comparison between the shear modulus and the confining pressure. While this is a reliable method to determine the pressure derivative within a layer of one material, at interfaces this can lead to spurious values. A smoothing operation with a weighing

function can remove such outliers at the cost of resolution. Alternatively, one could conduct a lab experiment to determine the pressure derivative of the shear modulus as a function of depth and hence maintain a better vertical resolution.

There are unexplained low-frequency data (Figure 3.11). For frequencies below 0.5 Hz we are pushing the 4.5 Hz geophones to their limits. With much instrumental noise at these frequencies, the retrieved velocity variations are of low quality. However, for the inversion part the quality of the low-frequency velocity variations does not really matter, since the resolution shows that the pore pressure models below 200 m cannot be interpreted anyway.

In this study we showed that the velocity variations between 0.7 and 1.8 Hz can be attributed to pore pressure changes. While in Groningen pore pressure change is the main source for velocity variation, other sources also need to be addressed. Locally, earthquakes can cause subsurface damage, resulting in a velocity drop (e.g., Brenguier et al., 2008a; Wegler et al., 2009). However, this local effect has only been reported for much larger earthquakes than the ones observed in the Groningen area. Also temperature variations can induce seismic velocity changes (e.g., Colombero et al., 2018; Richter et al., 2014). Seasonal temperature variations by thermal diffusion through quartz, however, are naturally restricted to 0.1°C for depths below 20 m, and thermal energy storage systems only induce local temperature changes that cannot be resolved with our spatial resolution. Moisture variations within the vadose zone cause changes in density that can affect surface-wave velocities (e.g., Knight et al., 1998). In Groningen, however, the groundwater table can be found at approximately 1 m depth, which leaves a very small vadose zone and therefore a limited sensitivity to changes therein. For these reasons, we do not expect that other mechanisms should notably affect the seismic velocity, and therewith the pore pressure models at depths below 20 m.

Within the inversion procedure for depth variations of pore pressure, we used well-defined data and model covariances, enabling the use of the explicit Bayesian formulation. When data or model covariances are not available, it is still possible to carry out a damped least-squares inversion. One can search for an optimum weight for the residual norm minimization and the solution norm minimization. Additionally, one could use the correlation coefficient $CC_{max}(\omega, t)$ (Equation 3.2) as proxy for the quality of the retrieved velocity changes, since Fokker and Ruigrok (2019) showed that the standard deviation of retrieved velocity changes $\sigma(\omega_i, t_k)$ correlates strongly with $1 - CC_{max}(\omega_i, t_k)$. Therefore, this can be used as an alternative to the data covariance presented in this study (Equation 3.13).

3.8. Conclusions

This study introduces a new technique for pore pressure monitoring using passive image interferometry. We derived that pore pressure sensitivity kernels can be used to link surface-wave velocity change as function of frequency directly to pore pressure change as function of depth. In Groningen, the Netherlands, most sensitivity to pore pressure changes lays in the very shallow subsurface (i.e., top 200 m), much

shallower than the sensitivity to shear-wave velocity change. We showed that pore pressure sensitivity kernels can be used to invert surface-wave velocity changes for pore pressure variations as a function of depth, resulting in four-dimensional pore pressure models, agreeing with independent measurements of pore pressure variation and showing hydrological features.

4

Feasibility of Pore Pressure Monitoring in Subsurface Reservoirs Using Surface-Wave Phase-Velocity Variations

Abstract

This chapter investigates the feasibility of reservoir pressure monitoring using surface-wave phase-velocity variations. The pore pressure sensitivity kernels introduced in Chapter 3 are expanded to encompass the depth ranges of the Harlingen and Groningen gas fields, and used to model Rayleigh-wave phase-velocity changes for realistic production scenarios. For the Harlingen reservoir, the velocity variations appear sufficiently large to be detectable on a yearly basis using passive image interferometry, but for the Groningen reservoir, the modeled velocity variations fall within the measurement uncertainty of velocity changes. For the Harlingen reservoir, we examine the potential of inferring reservoir pressures from surface-wave velocity variations in the presence of seasonal pore pressure variations in shallow aquifers. The investigation reveals that shallow pore pressure variations have a substantial impact on the precision of reservoir pressure models, adding up to an uncertainty of 0.2 MPa for the reservoir pressure inference. This is nevertheless sufficiently accurate to be able to capture production-related pore pressure developments.

The content of this chapter is currently in preparation for submission: Fokker, E., Ruigrok, E., & Trampert, J. (in preparation). Monitoring anthropogenic fluctuations in reservoir pressure using surface-wave phase-velocity variations: A feasibility study. *In preparation for submission to Geophysical Prospecting*.

Parts of this chapter appeared in: Fokker, E., Ruigrok, E., Hawkins, R., & Trampert, J. (2022). Pore pressure monitoring in a chalk gas reservoir using surface-wave velocity variations. *1st EAGE/SBGf Workshop on Reservoir Monitoring and its Role in the Energy Transition*, *2022*(1), 1–5.

4.1. Introduction

Operating subsurface reservoirs requires accurate knowledge of the pore pressure variations. This is important for forecasting the production and determining the effects of operational decisions. Traditional measurements of pore pressure are directly acquired in wells. However, an important drawback of such measurements is that they are local and sparse. Furthermore, in case of measurements in a flowing well, the pore pressure is distorted.

The optimal data acquisition provides reliable pore pressure measurements without the deployment of wells. Indirect measurements are required to this end. One example of such techniques uses surface movement measurements to infer pore pressure (Fokker & van Thienen-Visser, 2016; Smith et al., 2019). However, such inversions are often ill-conditioned and require considerable prior knowledge to yield accurate results. In addition, geodetic data are not always available at the required precision.

A second technology to reveal non-local pore pressure is the use of 4D seismic surveys. The two-way travel times change due to the combined effect of two phenomena: velocity changes due to changes in effective stress and changes in travelled distance due to the compaction of the reservoir (Angelov, 2009; Landrø & Stammeijer, 2004). 4D seismic surveys, however, are expensive. It requires repeated seismic surveys and needs to be planned in advance.

Fokker et al. (2023) introduced a physics-based technique for pore pressure monitoring using passive image interferometry. They showed that pore pressure sensitivity kernels can be used to invert surface-wave phase-velocity changes for pore pressure variations as a function of time and space. Pore pressure sensitivities were found to decrease rapidly with depth, limiting this approach to the depth range of $0-200$ m for natural variations ($du \sim 1$ kPa). However, production related pore pressure variations can be three orders of magnitude larger and possibly still induce measurable surface-wave velocity variations.

In this chapter, we investigate the feasibility of pore pressure monitoring with surface-wave velocity variations for the soft chalk gas reservoir in Harlingen and the sandstone gas reservoir in Groningen, both located in the north of the Netherlands. We expand the pore pressure sensitivity kernel presented by Fokker et al. (2023) (Section 3.4) to include the depth of the Harlingen and Groningen gas reservoirs, and forward model surface-wave phase-velocity variations for hypothetical production scenarios. To assess the feasibility of pore pressure monitoring related to production, we perturb the forward model of production-related velocity changes by the shallow-origin velocity variations observed in Groningen (Section 3.3), and invert for pore pressure variations in the reservoir layer. As we know the variance of velocity variations retrieved with passive image interferometry, we can use a Bayesian inversion scheme to invert the perturbed velocity-change model for changes in reservoir pressure, and assess the corresponding uncertainty.

4.2. Expanded Models of the Groningen Subsurface

To compute sensitivity kernels, Fokker et al. (2023) utilized models from a set of physical parameters between 0 and 1000 m depth. This depth range is sufficient for monitoring shallow-origin pore pressure variations, but the gas reservoirs are located in the deeper subsurface. To expand the sensitivity kernels to depth ranges of the Harlingen and Groningen gas reservoirs, we first need to expand the models of physical parameters.

We gather the models of physical properties for the subsurface of Groningen at seismic receiver G08 (KNMI, 1993). The location of this station and the Harlingen gas field are similarly close to the Wadden Sea, making the shallowest 1800 m very similar. For the unconsolidated subsurface, that is, roughly the shallowest 1000 m, we can use the shear-wave velocity and density models from Ntinalexis et al. (2023), whereas for the consolidated subsurface we can use the models from Romijn (2017). The compressional-wave velocity model is retrieved from Romijn (2017) for the full depth range. The models for compressional-wave velocity, shear-wave velocity and density are visualized in Figure 4.1a-c. Following Fokker et al. (2021, 2023), we construct from these models (d) the confining pres-

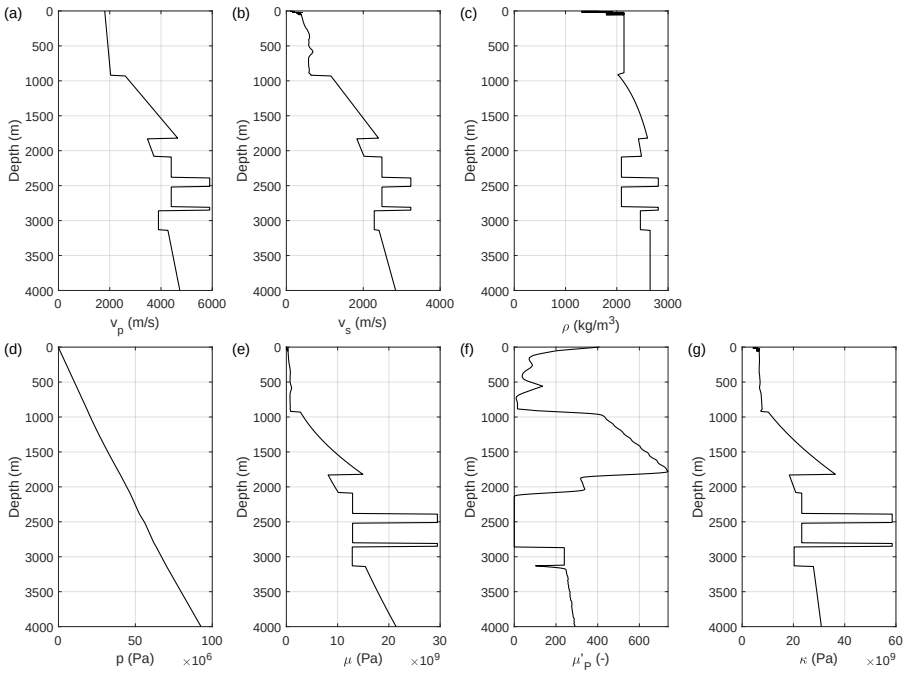

Figure 4.1: Models of physical properties used in this study, as a function of depth, retrieved from Ntinalexis et al. (2023) and Romijn (2017): (a) Compressional-wave velocity v_p, (b) shear-wave velocity v_s, (c) mass density ρ, (d) confining pressure under hydrostatic condition, $p(z) = \int_0^z \rho(z')g\,dz'$, (e) shear modulus $\mu = \rho v_s^2$, (f) smoothed derivative of the shear modulus with respect to the confining pressure $\mu'_p = \partial\mu/\partial p$, (g) bulk modulus $\kappa = \rho v_p^2 - \frac{4}{3}\rho v_s^2$.

sure $p(z) = \int_0^z \rho(z')g\,dz'$, (e) the shear modulus $\mu = \rho v_s^2$, (f) a smoothed derivative of the shear modulus with respect to the confining pressure $\mu'_p = \partial\mu/\partial p$, and (g) the bulk modulus $\kappa = \rho v_p^2 - \frac{4}{3}\rho v_s^2$.

The pressure derivative of the shear modulus (Figure 4.1f) is well-established for the depth range of the Chalk Group containing the Harlingen gas reservoir (1000-1030 m depth). The relatively high values can be explained by the weak nature of the chalk. For the Rotliegend sandstones harboring the Groningen gas field (2866-3124 m depth at the specific location of station G08), however, the pressure derivative of the shear modulus could not be derived, since the model only shows one value of the shear modulus for the entire reservoir depth range. From laboratory experiments on similar sandstones from the deep North Sea Basin (Orlander et al., 2021, Figure 9), we obtained a pressure derivative of the shear modulus of $\mu'_p = 240$, which we use for the depth range of the Groningen field.

4.3. Expanded Pore Pressure Sensitivity Kernels

The pore pressure sensitivity kernels as outlined by Fokker et al. (2023) establish a physics-based connection between depth-dependent pore pressure fluctuations du and frequency-dependent changes in surface-wave phase-velocity dc/c:

$$\frac{dc}{c}(\omega) = \int_0^\infty K_u(\omega, z)\,du(z)\,dz, \tag{4.1}$$

where

$$K_u(\omega, z) = -\frac{\mu'_p}{2\mu} K_{v_s}(\omega, z) \tag{4.2}$$

represents the pore pressure sensitivity kernel, μ symbolizes the shear modulus, μ'_p indicates the pressure derivative of the shear modulus, and K_{v_s} is the shear-wave sensitivity kernel of surface-wave velocities. The latter equation is exemplified in Figure 4.2, as it has been calculated for the parameters in Figure 4.1. The shear-wave sensitivity kernel (Figure 4.2a,d) has been computed using the adjoint method (Hawkins, 2018) on profiles for v_p, v_s and ρ (Figures 4.1a-c), and the fraction $-\mu'_p/2\mu$ (Figure 4.2b,e) has been computed using Figures 4.1e-f. The pore pressure sensitivity kernel in Figures 4.2c,f is the product of Figures 4.2a,d and 4.2b,e, in accordance with Equation 4.2. Note that the logarithmic color axes on the top row differ from the bottom row. The pore pressure sensitivity kernel shows that the Rayleigh-wave velocity is three orders of magnitude more sensitive to pore pressure changes at the depth of the Harlingen reservoir (1000-1030 m depth) than to pore pressure changes at the depth of the Groningen reservoir (2866-3124 m depth). For the depth range of 2100-2866 m, Figure 4.2f shows zero sensitivity to pore pressure variations. This is an artifact due to the absence of a model for μ'_p at this depth range.

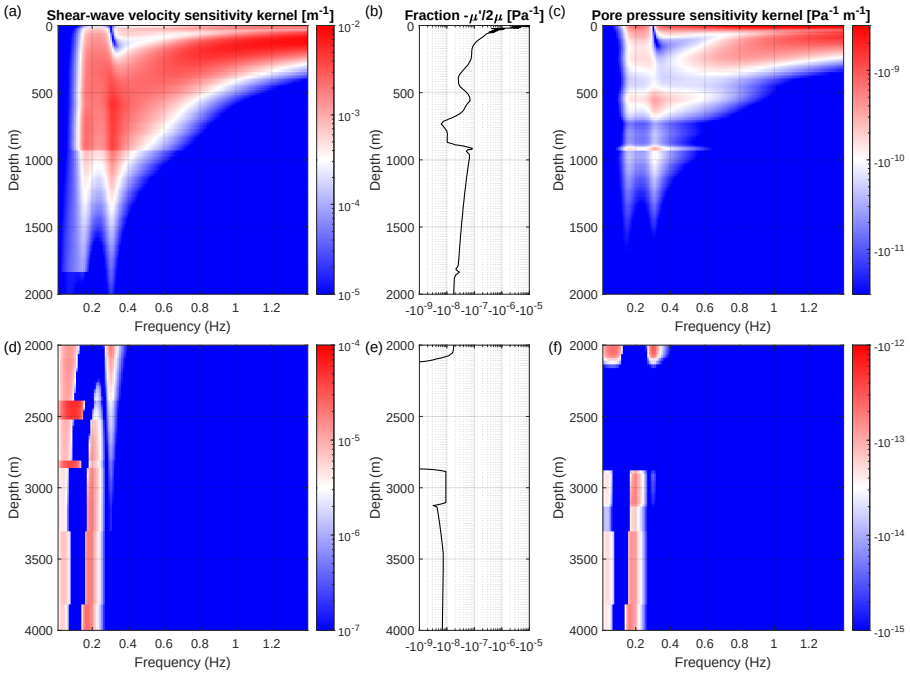

Figure 4.2: Visualization of Equation 4.2 for the subsurface of Groningen at seismic receiver G08 (KNMI, 1993): (a,d) shear-wave sensitivity kernel $K^R_{v_s}(\omega, z)$ for Rayleigh-wave phase velocity, computed using the adjoint method (Hawkins, 2018) on models for compressional-wave velocity, shear-wave velocity and density (Ntinalexis et al., 2023; Romijn, 2017), (b,e) fraction $-\mu'_p(z)/2\mu(z)$ where μ is the shear modulus and μ'_p is the pressure derivative of the shear modulus (derived from Ntinalexis et al., 2023; Romijn, 2017), and (c,f) pore pressure sensitivity kernel $K^R_u(\omega, z)$, which is a multiplication of figures (a,d) and (b,e). Note that the amplitude axes show logarithmic scales that differ from top and bottom rows.

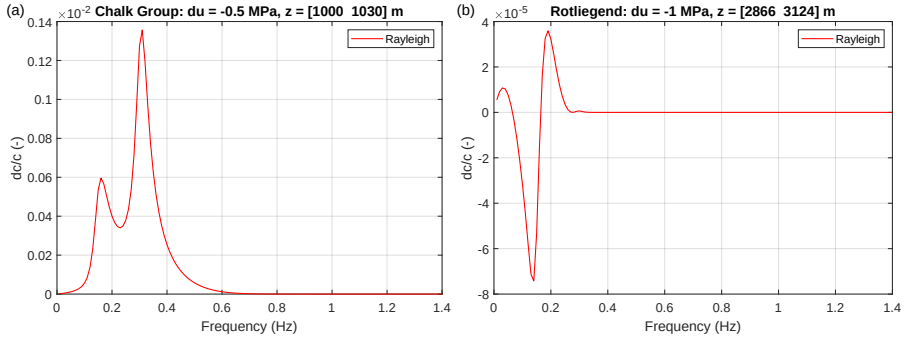

Figure 4.3: Rayleigh-wave velocity change related to gas production, as computed for (a) the Harlingen and (b) the Groningen gas fields using Equations 4.3 and 4.4, and the pore pressure sensitivity kernel presented in Figure 4.2c.

4.4. Forward Modeling of Surface-Wave Velocity Change

4.4.1. Harlingen Gas Reservoir

All the tools are now available to examine whether pore pressure changes in a gas reservoir can result in measurable surface-wave velocity changes. To illustrate this potential application, we first use parameters derived from a gas field in the northwest of the Netherlands that is located in a shallow and soft chalk: the Harlingen gas field. The depth and thickness of the field are about 1000 m and 30 m, respectively. The field has produced gas between 1988 and 2001 with an average pore pressure decrease of $du = -0.5$ MPa/year (Schatz & Bandiziol, 2014). Typical for the chalk is the strong pressure dependence of the shear modulus μ'_p. Although the Harlingen field is about 70 km west of the Groningen area, we can deploy the kernel derived for Groningen for an order of magnitude calculation, since the global subsurface structure is very similar: weak, unconsolidated layers down to 800 m and below that the chalk, reaching a depth of about 1500 m.

We compute Rayleigh-wave velocity change as a function of frequency by inserting the numbers for the Harlingen gas reservoir in Equation 4.1:

$$\frac{dc_R}{c_R}(\omega) = \int_{1000}^{1030} K_u^R(\omega, z)(-0.5 \cdot 10^6 \text{ Pa})dz, \tag{4.3}$$

and using Figure 4.2c as pore pressure sensitivity kernel $K_u^R(\omega, z)$. The resulting velocity change is illustrated in Figure 4.3a as a function of frequency. A pore pressure decrease in this specific depth range results in a Rayleigh-wave velocity increase concentrated between frequencies 0.1 and 0.6 Hz. For the average pore pressure change of $du = -0.5$ MPa/year, Rayleigh-wave velocity change is in the order of 0.1 %/year, which is measurable using passive techniques such as passive image interferometry (Sens-Schönfelder & Wegler, 2006).

4.4.2. Groningen Gas Reservoir

The northeast of the Netherlands hosts the Groningen gas field: the largest gas field in Europe. The reservoir depth ranges from roughly 2600 to 3200 m with a varying thickness of approximately 100 m in the southeast to 300 m in the northwest. At the location of seismic station G08, the reservoir ranges from 2866 to 3124 m depth. Gas production started at the early sixties (de Jager & Visser, 2017), and has continued to the present day. At the peak of production the reservoir pressure decreased by 1 MPa/year (van Oeveren et al., 2017).

Similar to the previous section, we compute Rayleigh-wave velocity change as a function of frequency by inserting the numbers for the Groningen gas reservoir in Equation 4.1:

$$\frac{dc_R}{c_R}(\omega) = \int_{2866}^{3124} K_u^R(\omega, z)(-1 \cdot 10^6 \text{ Pa})dz, \tag{4.4}$$

and using Figure 4.2f as pore pressure sensitivity kernel $K_u^R(\omega, z)$. The resulting velocity change is shown in Figure 4.3b as a function of frequency. A pore pressure

decrease in this specific depth range results in Rayleigh-wave velocity changes concentrated between frequencies 0.01 and 0.3 Hz. For the high estimate of the yearly pore pressure drop, $du = -1$ MPa, the relative change in the Rayleigh-wave velocity is in the order of 10^{-4}. This falls within the range of uncertainty of velocity-change measurements, as velocity changes are retrieved with an uncertainty of about $\sigma_{dc/c} \sim 5 \cdot 10^{-4}$ (e.g., Figure 3.7a).

The Rayleigh-wave velocity change due to gas production was estimated for the maximum pore pressure drop that the Groningen field experienced over the last decades, and at a location where the reservoir reaches its maximum thickness. Decreasing the pressure change or the reservoir thickness further decreases the amplitude of surface-wave velocity changes, and hence the possibility to detect phase-velocity variations related to gas depletion in the Groningen field. Therefore, pore pressure monitoring using surface-wave phase-velocity variations appears not feasible for the Groningen gas reservoir.

4.5. Feasibility of Reservoir Pressure Monitoring

Finding that reservoir pressure developments in the Harlingen field have a substantial effect on surface-wave phase velocities does not automatically imply that reservoir pressures can be inferred from surface-wave velocities. Due to the large sensitivity of surface-wave velocities to shallow pore pressure changes, even small shallow-origin velocity variations can disturb velocity changes related to production. To assess the feasibility of inferring reservoir pressures from surface-wave velocity measurements, we generate artificial velocity data due to production, perturb the velocity data using shallow-origin velocity-change measurements, invert them for pore pressure models, and quantify the uncertainty of such inverse models.

We model a hypothetical production scenario where pore pressures within the reservoir decrease linearly over time (Figure 4.4a red). Similar to the previous section, we compute seismic velocity changes as a function of frequency. The average velocity variations within certain frequency ranges serve as artificial velocity data in this feasibility study (Figure 4.4b). We use the frequency ranges employed in Chapter 3 (Figure 3.7b), as these frequencies have sufficient signal-to-noise ratios with the 4.5 Hz geophones.

We perturb the forward model by the shallow-origin velocity variations observed in Groningen. Since the shallow subsurface in the Harlingen area is similar to the Groningen region, we expect similar hydrologic pore pressure variations in the shallow subsurface, resulting in similar natural velocity variations. The measured seasonal velocity variations (Section 3.3) are shown in Figure 4.4c, and the perturbed artificial velocity data is shown in Figure 4.4d for three example frequencies. Figure 4.4d represents the sum of Figures 4.4b and c. As measurement uncertainty of the perturbed artificial data we adopt the measurement uncertainty of the velocity variations observed in Groningen.

With a few alterations, we follow the inversion method presented in Section 3.5 to invert the perturbed velocity-change model for pore pressure variations as

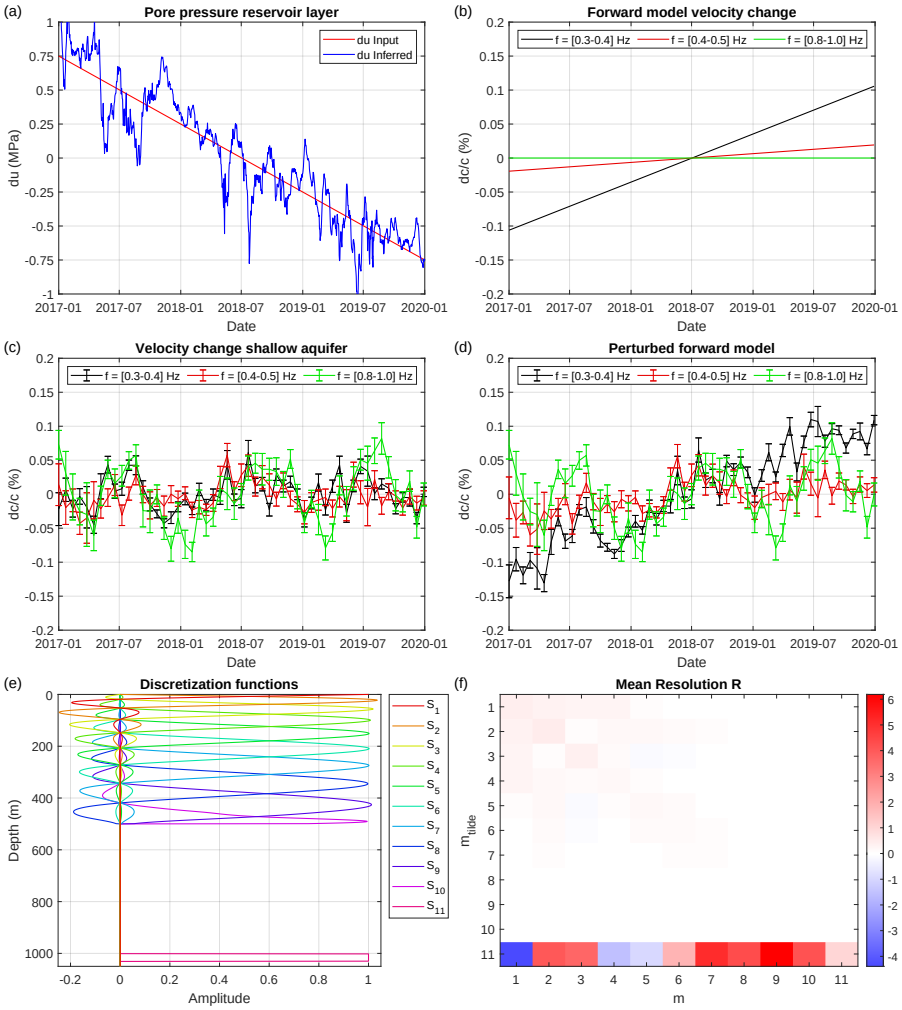

Figure 4.4: Forward and inverse modeling of surface-wave velocity changes due to reservoir pressure developments: (a) Input (red) and inferred (blue) pore pressure model for the reservoir layer, (b) surface-wave velocity changes for three example frequencies, computed using Equation 4.1, the pore pressure sensitivity kernel presented in Figure 4.2c and the input pore pressure model in (a), (c) seasonal velocity changes as measured using passive image interferometry (Section 3.3), (d) perturbed forward velocity-change model, obtained through the sum of (b) and (c), (e) discretization functions S_j used to discretize pore pressure change du in accordance with Equation 4.5, (f) resolution matrix indicating the model leakage in the inversion process from one model coefficient to another.

a function of depth. Compared to Section 3.5, we discretize pore pressure change du with an additional reservoir layer:

$$du(z, t_k) = \sum_j S_j(z) m_j(t_k), \tag{4.5}$$

with function $S_j(z)$ chosen to be a cubic natural spline function for $j \leq 10$ and a Boxcar function bounded by the reservoir depth range for $j = 11$ (Figure 4.4e). Their model coefficients are given by $m_j(t_k)$ at time t_k. We discretize the pore pressure sensitivity kernel for Rayleigh-wave velocity change accordingly.

Whereas for shallow depths pore pressure variations appear in the order or $du \sim$ 1 kPa, for the reservoir layer we can expect larger pressure variations in the order of $du \sim 1$ MPa. We construct the prior model covariance accordingly, such that $C_{\boldsymbol{m}}^{ij} = 10^6 \delta_{ij}$ Pa^2 for $j \leq 10$ and $C_{\boldsymbol{m}}^{ij} = 10^{12} \delta_{ij}$ Pa^2 for $j = 11$.

As the shallow-origin velocity changes were obtained with a certain variance, reflecting observational uncertainty and spatial variability, we can assume that also velocity variations due to both shallow-origin and reservoir pore pressure variations would be obtained with such an uncertainty. Therefore, we assign the same variance to the perturbed forward model. This allows us to construct a data covariance matrix with the velocity-change variance on the diagonal, and perform a Bayesian inversion as outlined in Section 3.5.

We invert the artificial velocity-change data to find model representation m_j. The reservoir pressure at time t_k is then described by model representation $m_{11}(t_k)$. Figure 4.4a shows in blue the inferred reservoir pressure as a function of time.

Compared to the hypothetical reservoir pressure (4.4f; red), the inferred model (4.4f; blue) has been contaminated by the shallow-origin velocity-change measurements. Within the inversion process, pore pressure changes leak from one layer to another. However, the pore pressure model also shows a clear trend consistent with the production-related pore pressure decline.

Knowing the input pore pressure enables us to quantify the uncertainty of reservoir pressure using such a method. The uncertainty can be described by the standard deviation of the inferred model with respect to the input. We observe an uncertainty of 0.2 MPa, which is sufficiently small for monitoring pore pressure changes related to production.

The uncertainty of the reservoir pressure model is a result of leakage from other model coefficients. The resolution matrix (Figure 4.4f) shows on the bottom row values varying from -4 to 6, indicating that actual pore pressure variations at corresponding coefficients 1-10 reach the reservoir layer model coefficient amplified by these values. In contrast, column 11 shows values in the order of 10^{-6}, indicating that reservoir pressure developments negligibly affect shallow pore pressure models. Diagonal element 11 shows a value of 0.998, indicating that 99.8% of reservoir pressure changes reaches the reservoir pressure model.

4.6. Discussion

We developed a forward model describing surface-wave velocity changes due to reservoir pressure variations. Specifically, we considered how reservoir pressure developments affect Rayleigh-wave velocities through changes in the shear modulus. However, three other processes in the reservoir affecting the seismic velocity need to be considered. First, the gas extraction does not only lead to a pore pressure change, but also to a gas density decrease. A pore pressure change $du = -0.5$ MPa corresponds to gas density change of $d\rho = -6$ kg/m^3, causing negative velocity changes that are two orders of magnitude smaller than the velocity changes presented in Figure 4.3. Second, a decrease in pore pressure results in a decrease in volumetric strain, which results in a small increase of the rock density. This mechanism induces positive velocity changes that are four orders of magnitude smaller than the ones presented in Figure 4.3. Last, through compaction the elastic parameters (Fig. 4.2b) can also change, affecting the pore pressure sensitivity kernel. A decrease in pore pressure $du = -0.5$ MPa corresponds to an increase in effective pressure of $p = 0.5$ MPa. At a 20 m larger depth, where the effective pressure was 0.5 MPa larger already, the fraction of elastic parameters ($-\mu'_p/2\mu$, Fig. 1b) is 6% smaller. Therefore, the pore pressure sensitivity kernels themselves are affected by pore pressure change. By using the linear kernel-based approach for such a nonlinear problem we introduce errors up to 6% and overestimate surface-wave velocity change by this amount (i.e., we would predict velocity change $dc/c = 0.106\%$ instead of 0.1%). While this is important in future research, it does not affect the conclusions.

Inferring changes in reservoir pore pressure, we employed the frequency bandwidths used in Chapter 3 (Figure 3.7b). For the retrieved shallow-origin velocity variations, we applied passive image interferometry to ambient seismic ambient noise recorded with 4.5 Hz geophones. Frequencies below 0.2 Hz were omitted because the instrumental noise dominated over the coherent seismic ambient noise. By choosing these frequency ranges as artificial velocity data, we include the maximum velocity change at 0.3 Hz, but we exclude the second maximum at 0.15 Hz (Figure 4.3a). Knowledge about velocity change between 0.1 and 0.2 Hz may improve the accuracy of the inferred reservoir pressure model. One would have to record seismic ambient noise with broadband sensors and compute seismic velocity changes using these data.

Based on the variance of velocity changes, retrieved with passive image interferometry, we can conclude that reservoir pressure monitoring in the Groningen gas reservoir is not possible using passive image interferometry, as the expected surface-wave velocity changes fall within the measurement uncertainty. The measurement uncertainty would need to be decreased by a factor of 5-10 to reveal phase-velocity changes due to 1 MPa pressure drops in a thick part of the reservoir. For a thinner part of the reservoir, or for smaller pressure changes, the measurement accuracy needs to be improved even further.

We investigated how the uncertainty of reservoir pressure inferences is affected by shallow pore pressure variations. It is yet to be determined how pressure changes just above or below the reservoir affect the inversion process.

Reservoir pressure monitoring has been presented in this chapter as a one-dimensional problem. In reality, the reservoir depth and thickness vary over the region. Consequently, the signature of surface-wave velocity changes can vary over the region. For dipping reservoirs this presents considerable challenges for using passive image interferometry on such a problem. Instead of using passive image interferometry as presented in Section 3.3, it is key to horizontally localize surface-wave velocity changes first. This has been shown to be possible for shallow-origin surface-wave velocity variations (James et al., 2019; Mao et al., 2022; Margerin et al., 2016). Subsequently, we can employ local pore pressure sensitivity kernels to infer pore pressure variations using the method presented here.

4.7. Conclusions

Pore pressure changes can be coupled to surface-wave velocity changes through pore pressure sensitivity kernels. This allows us to calculate surface-wave phase-velocity change as a function of frequency for realistic values of pore pressure change within subsurface reservoirs. We found that for reservoir pressure changes in the Harlingen field, Rayleigh-wave velocity changes are sufficiently large to be detectable with a yearly resolution using passive image interferometry. For reservoir pressure developments in the Groningen field, however, the induced surface-wave phase-velocity changes fall within the range of measurement uncertainty. Therefore, reservoir pressure monitoring using surface-wave velocities is not feasible for the Groningen field.

For the Harlingen field, we investigated the feasibility of inferring reservoir pressures from surface-wave velocity variations in the presence of pore pressure variations in shallow aquifers. Shallow pore pressure variations were found to significantly contribute to the uncertainties of the reservoir pressure models. The surface-wave velocity variations as present in the province of Groningen, the Netherlands, introduce an uncertainty of 0.2 MPa for the reservoir pressure inference. This implies that, for reservoirs like the shallow Harlingen reservoir with a yearly pressure depletion of 0.5 MPa, it is feasible to monitor field-wide pore pressure changes with continuous seismic noise recordings at the surface, even in the presence of pore pressure variations in shallow aquifers.

5

On the Temperature Sensitivity of Near-Surface Seismic Properties

Abstract

Subsurface temperature measurements play a crucial role in optimizing geothermal power plants and monitoring heat-storage systems. Previous studies have demonstrated that time-lapse variations in temperature can be correlated with variations in seismic velocity, offering the potential for temperature monitoring through seismic velocity changes. However, a discrepancy has emerged between field and laboratory experiments. Field studies predominantly report positive correlations between temperature and seismic velocities, while laboratory experiments often disclose anti-correlations. This inconsistency underscores the need for a comprehensive, physics-based understanding of temperature-induced velocity changes. In this study, we strive to bridge the gap between field and laboratory findings by examining three mechanisms governing temperature-induced seismic velocity change: (1) the intrinsic temperature dependency of elastic parameters, (2) thermally-induced stress, and (3) thermally-induced strain. We present a series of physics-based models to identify the primary mechanisms responsible for temperature-induced seismic velocity changes and to assess the sensitivities of seismic velocities to temperature fluctuations. Our investigations indicate that thermally-induced strain can be considered negligible in the context of our models. Instead, the intrinsic temperature dependency of elastic parameters and thermally-induced stress emerge as the primary contenders, offering a potential explanation for the discrepancies observed between field and laboratory experiments. We considered models for the unconsolidated sediments in the shallow subsurface of Groningen, where subsurface temperature fluctuations are driven by seasonal atmospheric temperature fluctuations roughly between −5 and 30 °C. For these models, we predict seasonal temperature-induced changes in body-wave velocities of up to 8%, high-frequency surface-wave phase-velocity variations in the range of 1-2%, and relative changes

A revised version of this chapter has been accepted for publication: Fokker, E., Ruigrok, E., & Trampert, J. (2024). On the temperature sensitivity of near-surface seismic wave speeds: Application to the Groningen region, the Netherlands. *Geophysical Journal International*, *in press.*

in site amplification on the order of 4%. These findings contribute to a more comprehensive understanding of the intricate relationship between temperature and near-surface seismic properties, offering insights for applications as subsurface temperature monitoring systems.

5.1. Introduction

Accurate subsurface temperature measurements are key to optimizing geothermal power plants and monitoring heat-storage systems. Previous studies showed that time-lapse variations in temperature correlate with variations in seismic velocity (e.g., Bièvre et al., 2018; Colombero et al., 2018; Ermert et al., 2023; Lecocq et al., 2017; Richter et al., 2014; Sleeman & de Zeeuw-van Dalfsen, 2020). This suggests the possibility of using seismic velocity variations as a means to monitor temperature changes. However, not all mechanisms for temperature-induced velocity change have been considered at once, and the conditions under which temperature variations induce measurable seismic velocity changes are not well understood.

Moreover, field and laboratory studies have yielded seemingly contradictory results when examining the relationship between temperature and seismic velocity. Most field studies have reported positive correlations between temperature and seismic velocities (e.g., Ermert et al., 2023; Lecocq et al., 2017; Richter et al., 2014; Sleeman & de Zeeuw-van Dalfsen, 2020), while most laboratory experiments have shown anti-correlations (e.g., Birch, 1943; Christensen, 1979; Jaya et al., 2010; Kern, 1978; Kohnen, 1974). It is not always clear which mechanisms drive velocity changes under which conditions.

Understanding the mechanisms behind velocity changes is needed to determine when and where temperature monitoring using seismic signals is feasible. By studying the underlying mechanisms, we can identify the dominant factors contributing to temperature-induced seismic velocity changes, assess the potential for temperature monitoring using seismic velocity measurements, and infer environmental implications such as the seasonality of site amplifications.

This study presents a series of physics-based models, identifying temperature-induced changes in seismic properties. The approach, as visually outlined in Figure 5.1, involves estimating subsurface temperature evolutions resulting from surface temperature variations (Section 5.3.1), evaluating the corresponding thermally-induced stresses and strains (Section 5.3.2), and determining temperature-induced variations in body-wave velocities (Section 5.3.3), surface-wave velocities (Section 5.3.4) and site amplifications (Section 5.3.5). We identify the dominant mechanisms driving temperature-induced seismic velocity change and introduce temperature sensitivity kernels as a tool for monitoring temperature variations with surface-wave velocity variations.

5.2. Physical properties and temperature data

Physics-based modelling of temperature-induced variations in seismic velocities requires models correctly describing the physical properties. We use models from the subsurface of the province of Groningen in the Netherlands, and lab experiments on similar unconsolidated materials. The Groningen region provides an

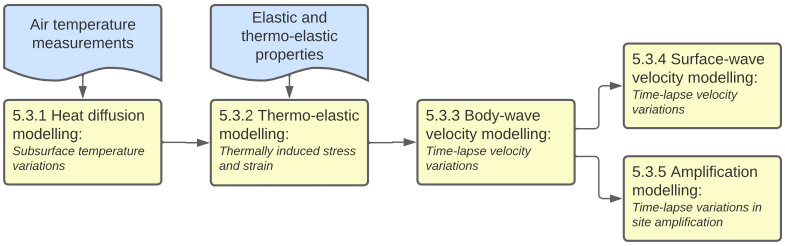

Figure 5.1: Block diagram of the series of physics-based models for temperature-induced variations in seismic properties. The yellow blocks represent modelling processes, each corresponding to a subsection of Section 5.3, and the blue blocks denote physical properties (Figure 5.2) or measurements. An overview of the parameters used in this study can be found in the Glossary.

ideal setting for physics-based modelling due to its well-documented geological and geophysical characteristics. Moreover, we can rely on air temperature measurements from the meteorological station in Eelde, operated by the Royal Netherlands Meteorological Institute (KNMI, 2023). The properties and mathematical definitions used in this study can be found in the Glossary.

We gather shear-wave velocity and density models from Ntinalexis et al. (2023) and a compressional-wave velocity model from Romijn (2017), all at the location of seismic station G08 (KNMI, 1993). From these models we can compute all elastic parameters needed for this study. Following Fokker et al. (2021, 2023), we compute the pressure derivative of the bulk and shear moduli by a pointwise derivative of the bulk and shear moduli with respect to the confining pressure. A smoothing operation with a robust weighing function and positivity constraint removes outliers that occur at layer intersections. Figures 5.2a-h show the elastic models used in this study. The detailed models of Ntinalexis et al. (2023) in blue have been smoothed for this study to obtain the black curves.

Thermo-elastic model parameters should be selected from experiments on similar unconsolidated materials. Temperature derivatives of the bulk and shear moduli can only be determined in a laboratory setting. For fully saturated clays, Bentil and Zhou (2022) found that after multiple thermal cycles the temperature derivative of the shear modulus is in the order of $\mu'_T \sim -0.6 \cdot 10^6$ Pa/°C (Figure 5.2i). For the temperature derivative of the bulk modulus, however, we could not find values for unconsolidated materials. At a temperature of $T = 20$°C, values are reported to be $\kappa'_T = -5.3 \cdot 10^6$ Pa/°C and $\kappa'_T = -18 \cdot 10^6$ Pa/°C for quartz and calcite, respectively (Dandekar & Ruoff, 1968; Lakshtanov et al., 2007; Ohno, 1995; Orlander et al., 2021). In this study we use the value for quartz (Figure 5.2j), although this might be a slight overestimation for unconsolidated materials.

Thermal expansion coefficients can be as small as $\alpha_T \sim 10 \cdot 10^{-6}$/°C (Radkovskỳ et al., 2022; Svidró et al., 2020), whereas for natural clays and sands we find values from $\alpha_T \sim 18 \cdot 10^{-6}$/°C to $\alpha_T \sim 22 \cdot 10^{-6}$/°C (Bobrowski et al., 2018; McKinstry, 1965).

For the purpose of this study we use $\alpha_T = 20 \cdot 10^{-6}/°C$, independently of depth (Figure 5.2k). As thermal diffusivity of clayey sands, Kooi (2008) reported a value of $\alpha_d = 2.2 \cdot 10^{-6}$ m^2/s, which we adopt in our study, independently of depth (Figure 5.2l).

5.3. Workflow for modelling temperature-induced variations in seismic properties

We present a series of physics-based models, characterising temperature-induced variations in seismic velocities and site amplification. The workflow is visualized in the diagram in Figure 5.1, where the yellow blocks represent modelling processes and blue blocks denote physical properties. The diagram visually outlines the physics-based models presented in this section.

In Section 5.3.1 we describe how surface temperature variations cause subsurface temperature variations through heat diffusion. Then, we explain how under specific boundary conditions subsurface temperature variations induce thermal stresses and strains (Section 5.3.2). Third, we determine the temperature dependency of body-wave velocities through three mechanisms (Section 5.3.3). Then, in Section 5.3.4 we use temperature sensitivity kernels to link surface-wave velocity variations to temperature variations. And last, we model how temperature variations affect site amplification (Section 5.3.5).

5.3.1. Heat diffusion modelling

We assume here that temperature predominantly varies in the vertical direction. In this case, heat transport through diffusion can be described by the 1D heat diffusion equation,

$$\frac{\partial T}{\partial t}(z,t) = \alpha_d(z)\frac{\partial^2 T}{\partial z^2}(z,t), \tag{5.1}$$

where α_d represents the thermal diffusivity of the medium, and $\partial T/\partial t$ describes the change in temperature over time, due to spatial changes in the temperature gradient $\partial^2 T/\partial z^2$. Knowing the surface temperature evolution, i.e., air temperature measurements in Eelde (KNMI, 2023), and the thermal diffusivity ($\alpha_d \sim 2.2 \cdot 10^{-6}$ m^2/s; Kooi, 2008), we model the subsurface temperature evolution by (1) updating the temperature model at the surface using the air temperature measurements at time $t = \tau$,

$$T(z=0, t=\tau) = T^{(air)}(t=\tau), \tag{5.2}$$

(2) computing temperature change over time step Δt,

$$\Delta T(z, t=\tau) = \alpha_d(z)\frac{\partial^2 T}{\partial z^2}(z, t=\tau)\Delta t, \tag{5.3}$$

and (3) updating the temperature model for the next time step $t = \tau + \Delta t$,

$$T(z, t=\tau+\Delta t) = T(z, t=\tau) + \Delta T(z, t=\tau). \tag{5.4}$$

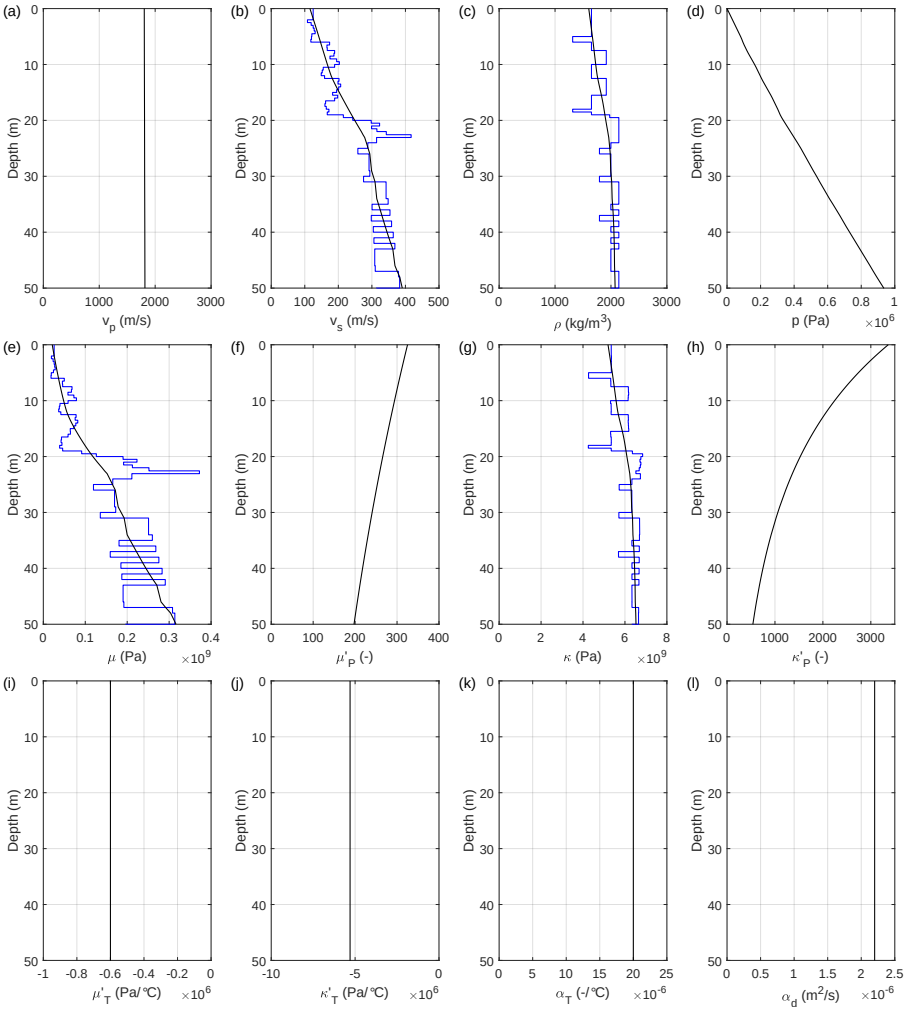

Figure 5.2: Models of physical properties used in this study, as a function of depth: (a) Compressional-wave velocity v_p retrieved from Romijn (2017), (b) shear-wave velocity v_s from Ntinalexis et al. (2023) in blue and smoothed in black, (c) mass density ρ as presented by Ntinalexis et al. (2023) in blue and smoothed in black, (d) confining pressure under hydrostatic condition, $p(z) = \int_0^z \rho(z')g\,dz'$, (e) shear modulus $\mu = \rho v_s^2$, (f) smoothed derivative of the shear modulus with respect to the confining pressure $\mu'_p = \partial\mu/\partial p$, (g) bulk modulus $\kappa = \rho v_p^2 - \frac{4}{3}\rho v_s^2$, (h) smoothed derivative of the bulk modulus with respect to the confining pressure $\kappa'_p = \partial\kappa/\partial p$, (i) temperature derivative of the shear modulus $\mu'_T = \partial\mu/\partial T$ for saturated clay after multiple thermal cycles (Bentil & Zhou, 2022), (j) temperature derivative of the bulk modulus $\kappa'_T = \partial\kappa/\partial T$ for quartz (Lakshtanov et al., 2007; Ohno, 1995; Orlander et al., 2021), (k) estimate of the thermal expansion coefficient α_T for unconsolidated materials (Bobrowski et al., 2018; McKinstry, 1965), and (l) thermal diffusivity α_d for clayey sands as reported by Kooi (2008).

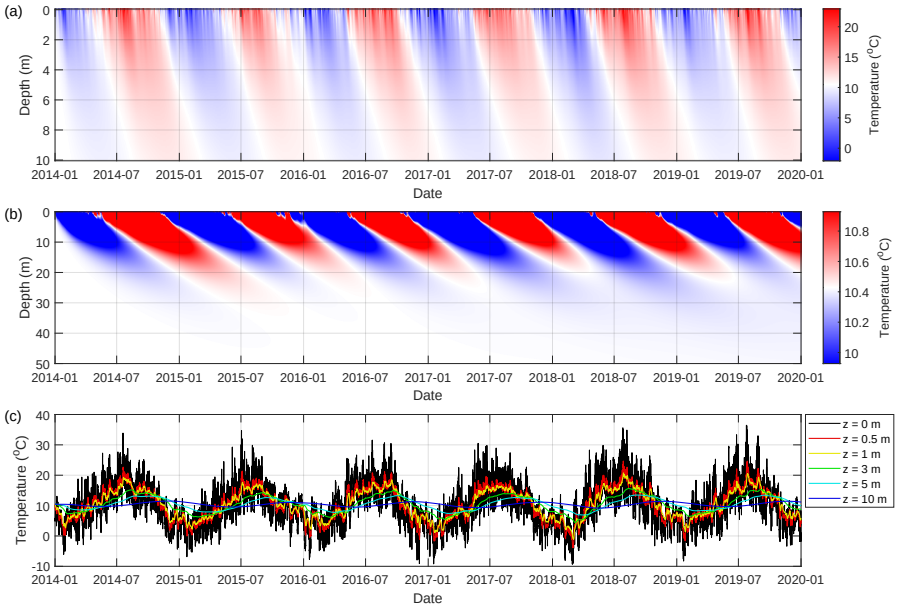

Figure 5.3: Temperature diffusion model for clayey sands ($\alpha_d = 2.2 \cdot 10^{-6}$ m^2/s; Kooi, 2008) as a function of time and depth in different visualizations: (a) Colour plot for the depth range 0 to 10 m, (b) colour plot clipped at temperature range 9.9 °C to 10.9 °C for the depth range 0 to 50 m, (c) line plots for various depth levels. Yearly temperature variations are clearly shown in all visualizations, whereas the daily variations are only visible in (a) and (c).

We start from a uniform temperature model, fixed at the average air temperature over six years $T_{avg}^{(air)} = 10.4$°C, and repeat steps (1), (2) and (3) for time steps of $\Delta t = 600$ s and vertical steps of $\Delta z = 0.1$ m to obtain a temperature model as a function of depth and time. The results are shown in Figure 5.3, revealing not only a rapid decrease in temperature change with depth, but also a time delay increasing with depth. At 10 meters depth we find a time delay of approximately four months with respect to the surface temperature and temperature differences between summer and winter are in the order of 1.5 °C. Daily temperature variations do not penetrate further than 1 meter into the subsurface. The results of Figure 5.3 are in the same order of magnitude as the direct subsurface temperature measurements by Bense and Kooi (2004, Figure 3) and Kole et al. (2020, Figure 29) with distributed temperature sensing at a similar site in Groningen. The temperature variations presented here will be used to drive dT in the next sections.

5.3.2. Thermo-elastic modelling

Subsurface temperature variations disturb the equilibrium between stress and strain. Using linear thermo-elasticity we can model such disturbances. Although we start with the same principle assumption as Berger (1975) and Richter et al. (2014), our approach is slighly different as we do not approximate temperature variations as cosine functions over time, and we do not consider lateral temperature

gradients. In addition to Fjær et al. (2008) and Jaeger et al. (2009), we include the pressure and temperature dependencies of the bulk and shear moduli and their effects on the thermally-induced stress and strain. In our analysis, we do not consider variations in effective stress through temperature-induced pore pressure changes.

Principles of linear thermo-elasticity

We base our model on the assumption that a change in strain is induced simultaneously by temperature and stress:

$$d\epsilon_{ij}^{\text{total}} = d\epsilon_{ij}^{\text{temp-ind}} + d\epsilon_{ij}^{\text{str-ind}}. \tag{5.5}$$

The change in strain $d\epsilon_{ij}$ is here defined positive for an increase in volume. A change in temperature affects the volume of an isotropic material as defined by the thermal expansion coefficient α_T (Nye, 1985):

$$\frac{\partial \epsilon_{ij}}{\partial T} = \alpha_T \delta_{ij}, \tag{5.6}$$

where ϵ_{ij} represents the strain tensor, T denotes temperature, and δ_{ij} indicates a Kronecker delta. The temperature-induced part of the change in strain can thus be written as

$$d\epsilon_{ij}^{\text{temp-ind}} = \alpha_T dT \delta_{ij}. \tag{5.7}$$

The stress-induced part of the change in strain can be obtained by taking the differential of Hooke's law for an isotropic body:

$$\sigma_{ij} = 2\mu\epsilon_{ij}^{\text{str-ind}} + \left(\kappa - \tfrac{2}{3}\mu\right)\epsilon_{kk}^{\text{str-ind}}, \tag{5.8}$$

$$d\sigma_{ij} = 2d\mu\epsilon_{ij}^{\text{str-ind}} + 2\mu d\epsilon_{ij}^{\text{str-ind}} + \left(d\kappa - \tfrac{2}{3}d\mu\right)\epsilon_{kk}^{\text{str-ind}} + \left(\kappa - \tfrac{2}{3}\mu\right)d\epsilon_{kk}^{\text{str-ind}}. \tag{5.9}$$

Here, σ_{ij} represents the stress tensor, defined negative for compressional stress, and μ and κ are the shear and bulk moduli, respectively. The combination of Equations 5.5, 5.7 and 5.9 provides the basis for linear thermoelasicity:

$$d\sigma_{ij} = 2d\mu\epsilon_{ij}^{\text{str-ind}} + 2\mu d\epsilon_{ij}^{\text{total}} + \left(d\kappa - \tfrac{2}{3}d\mu\right)\epsilon_{kk}^{\text{str-ind}} + \left(\kappa - \tfrac{2}{3}\mu\right)d\epsilon_{kk}^{\text{total}} - 3\kappa\alpha_T dT\delta_{ij}. \tag{5.10}$$

The initial and boundary conditions determine how temperature affects stress and strain. If a material is free to expand, temperature variations will not induce additional stresses, but in a fully rigid framework, the stress-induced part of strain must compensate the temperature-induced part of strain, hence thermal stresses will appear.

Initial and boundary conditions

To solve Equation 5.10 for change in pressure $dp = -\frac{1}{3}d\sigma_{kk}$ and change in volume $d\epsilon_{kk}$, we need to simplify Equation 5.10 using initial and boundary conditions.

First, for unconsolidated materials we can assume initial hydrostatic pressure,

$$\sigma_{ij}(z) = -p(z)\delta_{ij} = -\int_0^z \rho(z')g\,dz'\delta_{ij}, \tag{5.11}$$

with density ρ, gravitational acceleration g, and depth z. Through Equation 5.8 this leads to initial stress-induced strain

$$\epsilon_{ij}^{\text{str-ind}} = -\frac{1}{3\kappa}p\delta_{ij}. \tag{5.12}$$

This initial condition allows us to simplify Equation 5.10 to

$$d\sigma_{ij} = 2\mu d\epsilon_{ij} + \left(-\frac{d\kappa}{\kappa}p + \left(\kappa - \tfrac{2}{3}\mu\right)d\epsilon_{kk} - 3\kappa\alpha_T dT\right)\delta_{ij}. \tag{5.13}$$

Second, when heat diffusion from the surface into the subsurface is the source for temperature change, the temperature variations are quite homogeneous in the horizontal directions. In a horizontally infinite medium, or a medium with rigid boundaries, laterally homogeneous temperature variations cannot cause horizontal strain. Therefore, we assume horizontal strains to be static:

$$d\epsilon_{xx} = d\epsilon_{yy} = 0. \tag{5.14}$$

In the vertical direction, however, the material is free to expand, naturally restricting changes in vertical stress:

$$d\sigma_{zz} = 0. \tag{5.15}$$

Laterally homogeneous temperature variations thus induce horizontal stress and vertical strain. Applying these boundary conditions to Equation 5.13, while writing out all diagonal components, leads to the following expressions:

$$\begin{aligned} d\sigma_{xx} = d\sigma_{yy} &= -\frac{d\kappa}{\kappa}p + \left(\kappa - \tfrac{2}{3}\mu\right)d\epsilon_{zz} - 3\kappa\alpha_T dT, \\ 0 &= -\frac{d\kappa}{\kappa}p + \left(\kappa + \tfrac{4}{3}\mu\right)d\epsilon_{zz} - 3\kappa\alpha_T dT. \end{aligned} \tag{5.16}$$

Since the bulk modulus is a function of temperature and pressure, its differential can be written as

$$d\kappa = \kappa'_T dT + \kappa'_p dp, \tag{5.17}$$

with temperature and pressure derivatives of the bulk modulus $\kappa'_T = \partial\kappa/\partial T$ and $\kappa'_p = \partial\kappa/\partial p$, respectively, and change in pressure

$$dp = -\tfrac{1}{3}d\sigma_{xx} - \tfrac{1}{3}d\sigma_{yy}. \tag{5.18}$$

We now have enough information to deduce temperature-induced changes in pressure and volumetric strain.

Solution for temperature-induced changes in pressure and volumetric strain

To obtain changes in pressure and volumetric strain as a function of temperature, the elastic and the thermo-elastic properties, we form a system of equations consisting of Equations 5.16, 5.17 and 5.18, and solve for dp and $d\epsilon_{kk}$:

$$dp = \frac{4\mu\left(p\kappa'_T + 3\kappa^2\alpha_T\right)}{3\kappa^2 + 4\kappa\mu - 4\mu\kappa'_p p}dT, \tag{5.19}$$

$$d\epsilon_{kk} = d\epsilon_{zz} = \frac{3\left(p\kappa'_T + 3\kappa^2\alpha_T\right)}{3\kappa^2 + 4\kappa\mu - 4\mu\kappa'_p p}dT. \tag{5.20}$$

In Equations 5.19 and 5.20, every parameter is a function of depth z. Using these equations divided by dT, for the elastic and the thermo-elastic models presented in Section 5.2, we compute the temperature sensitivity of pressure and strain. Figure 5.4 shows the temperature sensitivity for pressure (a) and volumetric strain (b) as a function of depth. The steep increase of the pressure sensitivity with depth can be explained by the rapid increase in shear modulus μ. The stress and strain models both show a positive dependence on temperature. This also implies that the density, which can be related directly to volumetric changes as

$$\frac{d\rho}{\rho} = -d\epsilon_{kk} = -\frac{3\left(p\kappa'_T + 3\kappa^2\alpha_T\right)}{3\kappa^2 + 4\kappa\mu - 4\mu\kappa'_p p}dT, \tag{5.21}$$

will decrease when the temperatures increases.

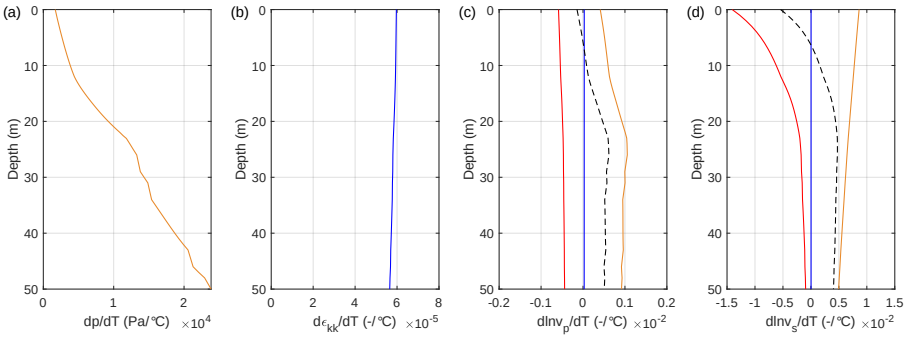

Figure 5.4: Sensitivities to temperature changes as functions of depth for the elastic and the thermo-elastic models presented in Section 5.2. Temperature sensitivity of pressure (a) and volumetric strain (b) in accordance with Equations 5.19 and 5.20, respectively. Sensitivity of compressional- (c) and shear-wave velocities (d) to temperature variations in accordance with Equations 5.26 and 5.27 for three mechanisms separately and for their sum. The red curves indicate the temperature sensitivities via the intrinsic temperature dependency of the elastic parameters, the orange curves show sensitivities through thermally-induced pressure, the blue curves reveal the sensitivity through thermally-induced strain, and the black dashed curves show the sum of all mechanism in accordance with Equations 5.26 and 5.27.

5.3.3. Body-wave velocity modelling

In this section we model how body-wave velocities are affected by temperature change. We consider three mechanisms for temperature-induced velocity change: (1) velocity change via the intrinsic temperature dependency of the elastic moduli, (2) velocity change through thermally-induced pressure (Equation 5.19), and (3) velocity change by thermally-induced strain (Equation 5.20). We determine the sensitivity of body-wave velocities for each mechanism and model velocity variations due to seasonal temperature changes (Section 5.3.1).

Compressional and shear wave velocities v_p and v_s depend on the bulk modulus κ, the shear modulus μ and the density ρ:

$$\begin{aligned} v_p &= \sqrt{\frac{\kappa + \frac{4}{3}\mu}{\rho}}, \\ v_s &= \sqrt{\frac{\mu}{\rho}}. \end{aligned} \tag{5.22}$$

Body-wave velocities can therefore only vary via these properties. By differentiating Equation 5.22, we obtain relative velocity changes

$$\begin{aligned} \frac{dv_p}{v_p} &= \frac{d\kappa + \frac{4}{3}d\mu}{2(\kappa + \frac{4}{3}\mu)} - \frac{d\rho}{2\rho}, \\ \frac{dv_s}{v_s} &= \frac{d\mu}{2\mu} - \frac{d\rho}{2\rho}. \end{aligned} \tag{5.23}$$

Similar to the bulk modulus (Equation 5.17), the shear modulus is also a function of temperature and pressure, hence its differential can be written as

$$d\mu = \mu'_T dT + \mu'_p dp, \tag{5.24}$$

with temperature and pressure derivatives of the shear modulus $\mu'_T = \partial\mu/\partial T$ and $\mu'_p = \partial\mu/\partial p$, respectively. By substituting Equations 5.17, 5.21 and 5.24 in Equation 5.23 we can write the velocity change as

$$\begin{aligned} \frac{dv_p}{v_p} &= \frac{\kappa'_T + \frac{4}{3}\mu'_T}{2(\kappa + \frac{4}{3}\mu)} dT + \frac{\kappa'_p + \frac{4}{3}\mu'_p}{2(\kappa + \frac{4}{3}\mu)} dp + \frac{1}{2} d\epsilon_{kk}, \\ \frac{dv_s}{v_s} &= \frac{\mu'_T}{2\mu} dT + \frac{\mu'_p}{2\mu} dp + \frac{1}{2} d\epsilon_{kk}, \end{aligned} \tag{5.25}$$

where the first terms represent temperature-induced velocity changes via the intrinsic temperature dependency of the elastic moduli, the second terms represent

pressure-induced velocity changes, and the third terms represent strain-induced velocity changes. Body-wave velocity variations as a function of temperature change are obtained by the substitution of Equations 5.19 and 5.20 in Equation 5.25:

$$d\ln v_p = \frac{dv_p}{v_p} = \frac{\kappa'_T + \frac{4}{3}\mu'_T}{2(\kappa + \frac{4}{3}\mu)}dT + \frac{\kappa'_p + \frac{4}{3}\mu'_p}{2(\kappa + \frac{4}{3}\mu)}\frac{4\mu\left(p\kappa'_T + 3\kappa^2\alpha_T\right)}{3\kappa^2 + 4\kappa\mu - 4\mu\kappa'_p p}dT + \frac{1}{2}\frac{3\left(p\kappa'_T + 3\kappa^2\alpha_T\right)}{3\kappa^2 + 4\kappa\mu - 4\mu\kappa'_p p}dT, \tag{5.26}$$

$$d\ln v_s = \frac{dv_s}{v_s} = \frac{\mu'_T}{2\mu}dT + \frac{\mu'_p}{2\mu}\frac{4\mu\left(p\kappa'_T + 3\kappa^2\alpha_T\right)}{3\kappa^2 + 4\kappa\mu - 4\mu\kappa'_p p}dT + \frac{1}{2}\frac{3\left(p\kappa'_T + 3\kappa^2\alpha_T\right)}{3\kappa^2 + 4\kappa\mu - 4\mu\kappa'_p p}dT. \tag{5.27}$$

All parameters of Equations 5.26 and 5.27 are a function of depth z. Using these solutions divided by dT, for the elastic and the thermo-elastic models presented in Section 5.2, we compute the temperature sensitivity of compressional- and shear-wave velocities. Figure 5.4 shows the temperature sensitivity of v_p (c) and v_s (d) as a function of depth, for each mechanism separately (red, orange, blue) and for their sum (black).

Figures 5.4c-d clearly show the opposing signs of the different mechanisms. Velocity changes via the intrinsic temperature dependency of the elastic parameters (red) are negatively affected by temperature, since the temperature derivatives of the bulk and shear moduli are negative. Velocity changes through thermal stress (orange) and strain (blue), on the other hand, are positively affected by temperature, since $|p\kappa'_T| < 3\kappa^2\alpha_T$ and all other parameters are positive. Although the different mechanisms have clearly opposing effects on the velocities, the amplitudes of velocity change through thermal stress and the intrinsic temperature dependency are in the same order of magnitude. Therefore, the sign of the sum of velocity change through all mechanisms can be positive or negative, depending on the parameters in Equations 5.26 and 5.27. For the models presented in Section 5.2, we notice total velocity changes with a negative sign from 0 to 6 m depth, and a positive sign beyond 6 m depth. The mechanism by thermal strain shows velocity changes two orders of magnitude smaller, hence this mechanism can be neglected for the chosen parameters.

Knowing the temperature sensitivity of compressional and shear-wave velocities, we can now model velocity variations due to temperature variations as modelled in Section 5.3.1. Temperature changes $dT(t,z)$ are constructed from the temperature model presented in Figure 5.3 by removing the mean temperature over six years, and substituted in Equations 5.26 and 5.27. Figure 5.5 shows the modelled velocity variations as a function of time and depth for compressional waves (a,b) and shear waves (c,d). The distinct change in sign at a depth of 6 m can again be explained by the transition from one dominant mechanism to another. Velocity

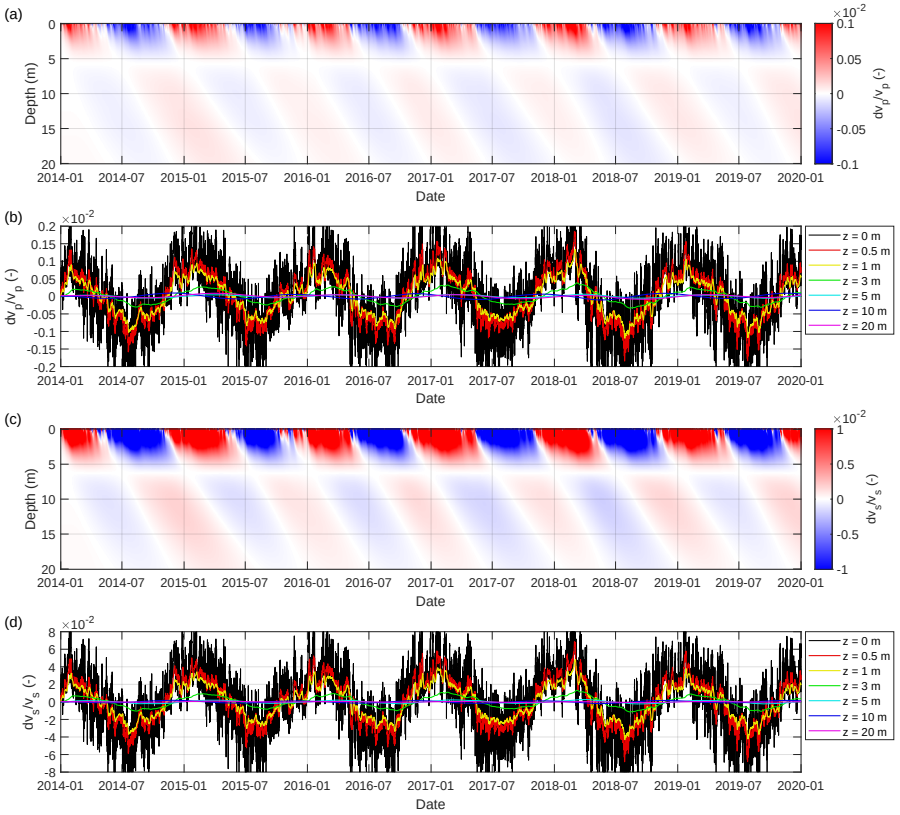

Figure 5.5: Variations in body-wave velocities due to the temperature variations modelled in Section 5.3.1 (Figure 5.3), visualised here as a function of time and depth. Velocity variations of compressional waves (a,b) and shear waves (c,d) are plotted as colour plots (a,c) and line plots (b,d). The models of velocity change were obtained by a multiplication of the temperature model presented in Figure 5.3, reduced by the mean temperature over six years, and the temperature sensitivities of compressional-wave and shear-wave velocities as displayed in Figures 5.4c-d.

changes in the first 6 m are dominated by the intrinsic temperature dependencies of the bulk and the shear moduli, while beyond a depth of 6 m velocity changes are dominated by thermally-induced stress.

5.3.4. Surface-wave phase velocity modelling

In this section we expand the temperature sensitivity study of the previous sections to surface-wave phase velocities. We introduce temperature sensitivity kernels and model Rayleigh- and Love-wave phase-velocity changes as a function of time and frequency.

Surface-wave phase velocity changes are mainly caused by changes in shear-wave velocities. For small velocity changes this can be described as

$$\frac{dc_R}{c_R}(\omega) = \int_0^\infty \left(K_s^R(\omega, z) d\ln v_s(z)\right) dz, \tag{5.28}$$

$$\frac{dc_L}{c_L}(\omega) = \int_0^\infty \left(K_s^L(\omega, z) d\ln v_s(z)\right) dz, \tag{5.29}$$

where c_R and c_L represent Rayleigh- and Love-wave phase velocity as a function of angular frequency ω, and shear-wave sensitivity kernels are indicated by K_s^R and K_s^L for Rayleigh and Love waves, respectively. Since the shear-wave velocity depends on temperature (Equation 5.27), we can rewrite Equations 5.28 and 5.29 as

$$\frac{dc_R}{c_R}(\omega) = \int_0^\infty \left(K_T^R(\omega, z) dT(z)\right) dz, \tag{5.30}$$

$$\frac{dc_L}{c_L}(\omega) = \int_0^\infty \left(K_T^L(\omega, z) dT(z)\right) dz, \tag{5.31}$$

where temperature sensitivity kernels K_T are defined as

$$\begin{aligned} K_T(\omega, z) =& K_s(\omega, z) \frac{d\ln v_s}{dT}(z) \\ =& K_s(\omega, z) \left(\frac{\mu_T'}{2\mu} + \frac{\mu_p'}{2\mu} \frac{4\mu\left(p\kappa_T' + 3\kappa^2\alpha_T\right)}{3\kappa^2 + 4\kappa\mu - 4\mu\kappa_p' p} + \frac{1}{2} \frac{3\left(p\kappa_T' + 3\kappa^2\alpha_T\right)}{3\kappa^2 + 4\kappa\mu - 4\mu\kappa_p' p} \right)(z). \end{aligned} \tag{5.32}$$

To obtain temperature sensitivity kernels for Rayleigh and Love waves, we compute shear-wave sensitivity kernels K_s^R and K_s^L using the adjoint method (Hawkins, 2018) on the one-dimensional profiles for compressional-wave velocity, shear-wave velocity and density presented in Section 5.2, and multiply them with the temperature sensitivity of the shear-wave velocity $d\ln v_s/dT$ as displayed by the black curve in Figure 5.4d. Figure 5.6 shows temperature sensitivity kernels for Rayleigh (a) and Love (b) waves. We find again a distinct sign change at 6 m depth, corresponding to the sign change in Figure 5.4d.

Phase-velocity changes of Rayleigh and Love waves are then modelled using Equations 5.30 and 5.31, the temperature sensitivity kernels shown in Figure 5.6, and the temperature variations as modelled in Section 5.3.1. Figure 5.7 shows the Rayleigh and Love wave velocity changes as a function of time and frequency. Unlike Figures 5.4c-d, 5.5 and 5.6, Figure 5.7 does not show the distinct sign change associated with a change in mechanism. This can be explained by the amplitude decay with depth of the temperature variations. This leads to very small changes in low-frequency surface-wave phase velocity. Velocity changes of Love waves can be neglected below 2 Hz, while for Rayleigh-wave velocity change can be neglected below 4 Hz. Besides the differences frequency-wise, velocity changes of Love waves are also larger in amplitudes compared to Rayleigh waves. This can be explained by the shallower sensitivity of Love-wave velocities in general.

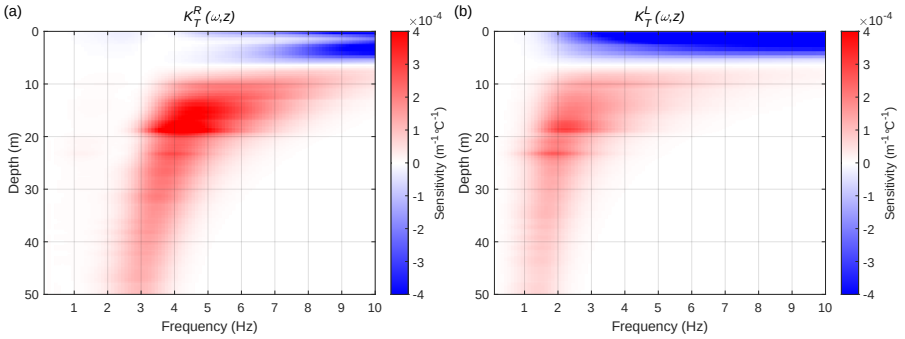

Figure 5.6: Temperature sensitivity kernels for Rayleigh (a) and Love waves (b), as computed using Equation 5.32. Shear wave sensitivity kernels K_s^R and K_s^L have been computed using the adjoint method (Hawkins, 2018) on the elastic parameters presented in Section 5.2, and multiplied by the temperature sensitivities of the shear-wave velocity (Equation 5.27; Figure 5.4d).

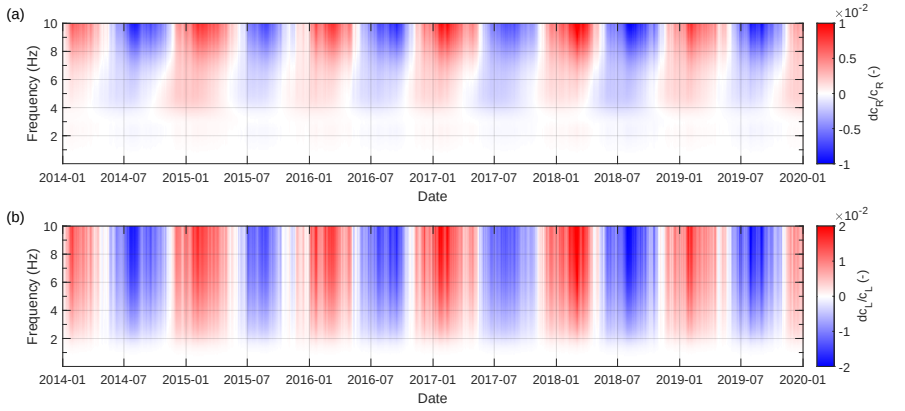

Figure 5.7: Variations in surface-wave phase velocities due to the temperature variations modelled in Section 5.3.1 (Figure 5.3), visualised here as a function of time and frequency. Velocity variations of Rayleigh waves (a) and Love waves (b) are plotted as colour plots. The models of velocity change were computed in accordance with Equations 5.30 (a) and 5.31 (b) for the temperature model presented in Figure 5.3, reduced by the mean temperature over six years, and the temperature sensitivity kernels for Rayleigh- and Love-wave velocities as displayed in Figures 5.6a-b.

5.3.5. Amplification modelling

Amplifications of relatively small earthquake motions in the Groningen region have led to considerable damage (Bommer et al., 2017; Kruiver et al., 2017b; Rodriguez-Marek et al., 2017; van Ginkel et al., 2019). As in similar regions, earthquake motions are amplified by the low impedance (density times velocity) of shallow soft sedimentary layers, overlaying harder bedrock (Bard et al., 1988; Bradley, 2012). Here we derive how the changes in compressional- and shear-wave velocity due to temperature variations (Section 5.3.3; Figure 5.5) affect site amplification.

Ruigrok et al. (2022, Appendix A) compared two approaches to compute the amplification factor using density and velocity, either using the Zoeppritz equation at every single interface, or assuming a smooth impedance gradient. The difference between the two approaches decreases with an increasing number of layers. For simplicity, we use the second approach, since we have many layers in the Groningen subsurface.

For smooth impedance gradients, the amplification term can be written as

$$F(z_1, z_2) = \sqrt{\frac{\rho_2 v_2}{\rho_1 v_1}}, \tag{5.33}$$

with ρ_1 and v_1 density and velocity corresponding to depth z_1, and ρ_2 and v_2 density and velocity corresponding to depth z_2. The amplification factor describes the relative increase in signal amplitude, when travelling from depth z_2 to z_1. A temperature-induced change in velocity at depth z_1, while depth z_2 is not subjected to change, leads to a relative change in amplification of

$$\frac{dF}{F}(z_1) = -\frac{1}{2}\frac{dv_1}{v_1}, \tag{5.34}$$

with dv_1/v_1 the relative velocity change at depth z_1.

Temperature-induced changes in amplification are computed using Equation 5.34 for compressional- and shear-wave velocity change at the surface (i.e., $z = 0$ m) as computed in Section 5.3.3. Figure 5.8 shows the amplification factors due to temperature-induced changes in body-wave velocity at the surface. The amplification factor for compressional waves changes by $dF_p/F_p \sim 0.1\%$ from winter to summer, while for shear waves we find values of $dF_s/F_s \sim 4\%$ from winter to summer.

5.4. Discussion

In this study, we delved into the physics of seismic velocity change caused by temperature variations. We established relationships based on fundamental principles. However, it is important to note that we did not account for all possible factors in our analysis, and therefore, our models may not fully explain all the observations found in the existing literature. Nonetheless, for unconsolidated materials we are confident that our investigation captured the dominant mechanisms for temperature-induced seismic velocity change.

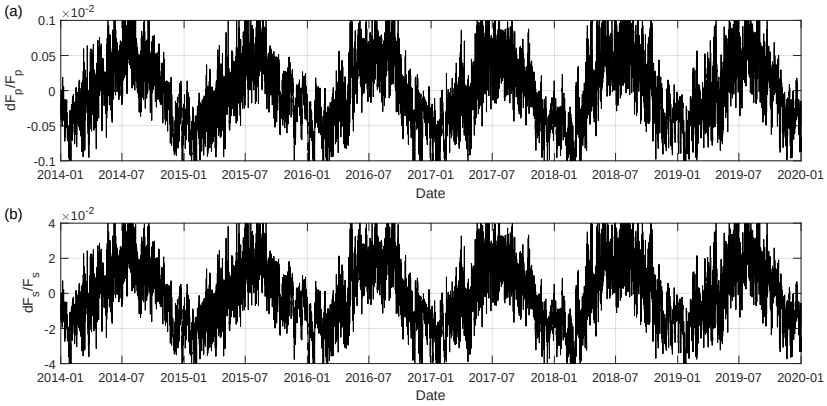

Figure 5.8: Relative change in site amplification due to the body-wave velocity variations modelled in Section 5.3.3 (Figure 5.5).

5

In Section 5.2, we selected from literature physical models for the shallow subsurface of Groningen or for similar unconsolidated materials. However, the literature lacks readily available temperature derivatives for bulk and shear moduli. For unconsolidated materials, we came across only one study that explores the connection between the shear modulus and temperature (Bentil & Zhou, 2022), and none that investigate the temperature dependency of the bulk modulus. Therefore, we resorted to values determined for quartz (Lakshtanov et al., 2007; Ohno, 1995; Orlander et al., 2021), which may be an overestimation. Less negative values for κ'_T would, in accordance with Equations 5.26 and 5.27, shift the red curve in Figure 5.4c (intrinsic temperature dependency) towards less negative values, while the orange curves in Figures 5.4c and d shift to slightly more positive values. Halving the value of κ'_T just pushes compressional-wave velocity change to the positive regime (Figure 5.4c black), while shear-wave velocity changes remain mostly unaffected. As alternative to laboratory experiments, temperature derivatives of the bulk modulus can for saturated materials potentially be approximated using the Gassmann equations, since Jaya et al. (2010) showed that fluid characteristics play a significant role in seismic velocity changes in a laboratory setting, and the bulk modulus of water is a well-known parameter as a function of temperature. We can use the Gassmann equations to compute the change in bulk modulus due to a substitution of water of a certain temperature with water of a different temperature, ultimately resulting in a temperature derivative of the bulk modulus.

The modelled temperature evolution in Section 5.3.1 is an approximation of the actual temperature developments, since temperature change due to advection and phase transitions (Rutten et al., 2010), and upward heat transport from the deep subsurface are not taken into account. Furthermore, not only are surface temperatures affected by air temperatures and radiation, air temperatures are also partly controlled by soil temperatures. Air temperature variations are therefore not simply a source for soil temperature changes, but merely an estimate of surface tempera-

tures. This does not pose a problem, since we only use air temperature measurements as boundary condition.

Upward heat transport from the deep subsurface results in a temperature gradient as shown by Ter Voorde et al. (2014). Such a steady gradient does not affect the change in temperature, since only the second spatial derivative contributes to temporal changes (Equation 5.1). Phase transitions can also form a source for temperature change. As the contact area between liquid and gas is largest in the unsaturated subsurface, evaporation mostly affects the temperature in this layer. During the summer, this layer will slightly cool down due to evaporation, hence the temperature difference between summer and winter will be slightly smaller than presented in Figure 5.3. This effect is rather small, as the modelled subsurface temperature differences between summer and winter are in the same order of magnitude as direct temperature measurements (Bense & Kooi, 2004; Kole et al., 2020). Groundwater flow can also contribute to heat transport (Bense & Kooi, 2004; de Louw et al., 2010). However, in the saturated subsurface, vertical flow is relatively low (maximum of 360 mm/yr, Kooi, 2008), making heat transport through advection negligible compared to the yearly heat transport by diffusion.

Regardless of the previously mentioned points of discussion, the subsurface temperature model presented in Section 5.3.1 aligns with direct temperature measurements (Bense & Kooi, 2004; Kole et al., 2020). This demonstrates that the heat diffusion model yields reasonable temperature estimations, and their magnitudes are consistent with observed data.

In Section 5.3.2 we made a few assumptions regarding thermo-elastic changes, including the exclusion of vertical stress and horizontal strain, as well as assuming an initial hydrostatic pressure. While these assumptions are valid in a horizontally isotropic medium with no horizontal temperature variations, they do not entirely hold true in reality. Nevertheless, due to the fact that horizontal variations in geology are small in an unconsolidated setting, and vertical heat diffusion is the dominant mechanism for temperature changes, these approximations remain reasonable.

Anelastic effects were not considered in our analysis. Due to a low shear strength there is a potential for reorganization in unconsolidated materials as sands and clays, leading to the anelastic transmission of horizontal stress to vertical strain (Ben-Zion & Leary, 1986). While the shear strength in unconsolidated materials is relatively small, it is not negligible (Liu et al., 2018). Therefore, shear stresses can indeed exist, implying that thermo-elasticity holds to some extent. It is only when the stress levels exceed the shear strength that anelastic changes will start to occur.

In our analysis, we did not consider temperature-induced changes in pore fluids. When the temperature rises under drained conditions, the pore fluid will expand as described by the thermal expansion coefficient of water ($d\epsilon_{kk}^{water}/dT = 3\alpha_T^{water} = 2.2 \cdot 10^{-4}/°\text{C}$ for $\alpha_T^{water} = 7.4 \cdot 10^{-5}/°\text{C}$ at $T = 12°\text{C}$), decreasing the fluid's mass density. However, the fluid's density affects the total density only by a small amount, leading to total strain changes smaller than the ones presented in Figure 5.4b. Consequently, the corresponding body-wave velocity changes are smaller than the already insignificant blue curves in Figures 5.4c,d and can hence be ne-

glected.

The pore fluids expand faster due to temperature changes ($d\epsilon_{kk}^{water}/dT = 2.2 \cdot 10^{-4}/°C$) than the total volume including the pore space ($d\epsilon_{kk}^{total}/dT = 0.6 \cdot 10^{-4}/°C$; Figure 5.4b). This leads to groundwater migration, a slight increase of the groundwater level, and hence a temperature-induced change in pore pressure and seismic velocity. It is however unknown how the porosity responds to expansion, hence we can only assess the order of magnitude for temperature-induced pore pressure change. The pore pressure $u(z)$ is determined by the height h of the water column above depth z, the density of the pore fluid ρ_w, and the gravitational acceleration g: $u = h\rho_w g$. For a relative increase of the water column of $2.2 \cdot 10^{-4}$ of an initial $h = 50$ m, the pore pressure increases by $du \sim 110$ Pa, independently of depth. Decreasing the density by relatively $2.2 \cdot 10^{-4}$ over the same depth range of 50 m, changes the pore pressure by $du \sim -110$ Pa at the bottom of the water column, while the top of the column remains unaffected. These pore pressure effects are at least two orders of magnitude smaller than the pressure changes presented in Figure 5.4a, and can thus be neglected. Under undrained conditions, the restriction of pore fluid expansion significantly affects the pore pressure and needs to be accounted for.

To reconcile laboratory and field experiments, we propose in Section 5.3.3 competing mechanisms for temperature-induced seismic velocity change. The negative intrinsic temperature dependencies of the shear and bulk moduli result in negative correlations between velocity and temperature changes, while the thermally-induced stresses and strains lead to positive correlations. In laboratory settings, typically only the intrinsic temperature dependency is tested, whereas in the field these mechanisms compete. In our chosen models, a clear turning point emerges at a depth of 6 m, above which the intrinsic temperature dependency is the dominant mechanism, and below which the mechanism through thermally-induced stress is dominant for temperature-induced seismic velocity change. The depth of this turning point is determined by the complex combinations of physical properties as presented in Equations 5.26 and 5.27.

We did not consider the effect of freezing and thawing of the pore fluids on the elastic parameters. Freezing of pore fluids significantly increases the shear modulus, consequently increasing body-wave velocities and decreasing site amplifications. This effect has not been taken into account. As Dutch winters are relatively mild (Figure 5.3), the temperatures in the unsaturated subsurface reach freezing temperatures only a few times per year and the saturated subsurface rarely freezes. In colder environments this needs to be addressed (e.g., James et al., 2019; Lindner et al., 2021).

In Section 5.3.4, we only considered surface-wave velocity change through changes in shear-wave velocities, and excluded density and compressional-wave sensitivity kernels in Equations 5.28, 5.29 and 5.32. We can justify this by two observations. Density and compressional-wave sensitivity kernels are at least an order of magnitude smaller than shear-wave sensitivity kernels, and temperature sensitivities of the density and compressional-wave velocity are at least one order of magnitude smaller than the temperature sensitivity of the shear-wave velocity (Figure 5.4c-d). Therefore, temperature-induced surface-wave phase-velocity change can

be approximated using Equations 5.30 and 5.31, and the temperature sensitivity kernels derived from shear-wave sensitivity kernels and temperature sensitivities of shear waves (Equation 5.32).

The derived sensitivity kernels in our study establish a connection between temperature variations and surface-wave phase-velocity changes. However, we need to note that the kernel-based approach is only valid for small perturbations, since pressure and temperature derivatives of the bulk and shear moduli are dependent on temperature and pressure themselves, and shear-wave sensitivity kernels also vary with shear-wave velocity. We expect that the velocity variations up to 8% (Figure 5.5) fall within the range of small perturbations.

In Section 5.3.5, we only considered changes in amplification due to temperature-induced body-wave velocity changes at the surface, whereas in reality temperature variations affect body-wave velocities at a larger depth range (Section 5.3.3). Moreover, we assumed a smooth impedance gradient. Although the introduced errors for the amplification factor are much smaller for the relative change in amplification, we treat the modelled changes in amplification only as order of magnitude. We need to note that temperature variations below well-insulated buildings may be smaller, leading to smaller differences in amplification, and the amplification factor at a building's foundation depth may be the more important factor for structure safety.

We focused on laterally homogeneous temperature variations. However, some other research considers lateral variations in temperature, leading to non-zero horizontal strains and vertical stresses (e.g., Ben-Zion & Allam, 2013; Ben-Zion & Leary, 1986; Berger, 1975; Richter et al., 2014). Such configurations result in stresses and strains propagating much deeper than the actual temperature change, as illustrated in Tsai (2011, Figure 1). Consequently, body-wave velocity changes are affected at greater depths, and surface-wave velocity changes extend to lower frequencies. Ermert et al. (2023) discovered that low-frequency sensitivities to surface temperature variations are particularly prominent in lake zones, where significant lateral temperature gradients exist. For higher frequencies they observed no distinction between zones with or without temperature gradients, suggesting that lateral temperature gradients do not significantly affect thermal stresses and strains in shallow layers. Our study area shows no significant lateral temperature gradient and Fokker et al. (2023) found no temperature-related seismic velocity changes up to 2 Hz. This indicates that laterally homogeneous temperature variations are a reasonable assumption in our research area.

Although the response of pressure to temperature change dp/dT increases with depth (Figure 5.4a), the sensitivities of body-wave velocity to temperature change $\frac{d\ln v}{dT}$ still decrease with depth (Figure 5.4c,d) due to the rapidly decreasing sensitivities of body-wave velocity to pressure change $\frac{d\ln v_s}{dp} = \mu'_p/2\mu$ and $\frac{d\ln v_p}{dp} = (\kappa'_p + \frac{4}{3}\mu'_p)/(2(\kappa + \frac{4}{3}\mu))$ (Equation 5.25). The shallow thermally-induced pressures are therefore more important, even if deeper pressure changes are induced due to lateral temperature gradients.

Comparing this study to the results of Fokker et al. (2023), we find a few similarities. For both temperature and pore pressure we can derive physics-based sensi-

tivity kernels for monitoring with surface-wave phase-velocity variations. The pore pressure sensitivity kernel decays slightly faster with depth, but the temperature sensitivity kernel also shows a rapid decay. Both temperature and pore pressure variations are the result of a diffusion process, driven by seasonal variations at the surface. Pore pressure diffusion is a relatively fast process, as it reaches confined aquifers at depths of 200 m in a time-scale of several days. Heat diffusion is rather slow, with a penetration depth of about 20 m that is reached in about a year. This difference in penetration depth makes that for the frequencies below 2 Hz, surface-wave velocity variations are dominated by seasonal changes in pore pressure. For the higher frequencies, we expect a combination of surface-wave phase-velocity variations induced by both pore pressure and temperature changes.

In our study, we studied seismic changes resulting from natural daily and seasonal temperature variations, and our assumptions were tailored accordingly. However, in the context of subsurface heat storage or geothermal power plants, certain assumptions need reconsideration. Specifically, we need to account for horizontal heat transport through diffusion and advection, as well as horizontal strain and vertical stress. Stricker et al. (2023) have demonstrated that it is possible to solve this problem semi-analytically (van Wees et al., 2019) for thermally-induced stresses and strains, as well as for pore pressure changes resulting from injection and production. To evaluate the effect of thermo-elasticity on seismic velocities, we can still use Equation 5.25. Aditionally, for the poro-elastic part, we can employ the equations provided by Fokker et al. (2021, Equations 12 and A2-A3).

Given the relationships between temperature, seismic velocities, and site amplification, the question arises: does climate change pose a threat to human safety through changes in site amplification? The temperature sensitivities presented in Figure 5.4d show that shear-wave velocities decrease by 0.5%/°C at the surface, leading to an increase in site amplification of 0.25%/°C. Even when considering a pessimistic temperature scenario of $dT = 4$°C by the year 2100 (Figure TS.4 in Pörtner et al., 2023), we predict an increase in site amplification in the order of only 1%. Therefore, climate change has a minimal effect on site amplification.

5.5. Conclusions

We have investigated the effects of temperature on seismic properties in the shallow subsurface. For models of physical parameters for the unconsolidated subsurface of Groningen in the Netherlands, we computed the sensitivity of near-surface seismic properties to temperature variations as a function of depth and frequency. Through a series of physics-based models, we estimated variations in subsurface temperature, evaluated thermally-induced stresses and strains, and determined how these factors influence body-wave velocities, surface-wave velocities, and site amplifications.

We have considered three mechanisms that contribute to velocity change: the intrinsic temperature dependency of elastic moduli, thermally-induced stress, and thermally-induced strain. Our findings revealed that thermally-induced strain is negligible and can be disregarded for our models. The intrinsic temperature dependency of the elastic parameters and thermally-induced stress were found to be

competing mechanisms, potentially reconciling discrepancies observed between field and laboratory experiments. We notice a distinct turning point at 6 m depth, above which the intrinsic temperature dependency dominates velocity changes, while below 6 m, thermal stress becomes the dominant factor.

We considered models for the shallow unconsolidated sediments in the shallow subsurface of Groningen, where subsurface temperature fluctuations are driven by seasonal atmospheric temperature fluctuations roughly between −5 and 30 °C. For these models, we predict seasonal temperature-induced changes in body-wave velocities up to 8%, high-frequency surface-wave phase-velocity variations of approximately 1-2%, and relative changes in site amplification in the order of 4%. The competition between the two dominant mechanisms for velocity change determines whether site amplification is more pronounced during summer or winter.

6

Conclusions and Outlook

6.1. Conclusions

Throughout this doctoral research, I developed a deeper understanding on the physics behind seismic velocity changes and hence their interpretations. I related seismic velocity variations to specific subsurface properties: fluctuations in pore pressure, vertical compressional stress, temperature, thermally-induced pressure and thermally-induced volumetric strain. This led to more accurate and comprehensive interpretations of surface-wave velocity variations originating from the shallow unconsolidated subsurface. Moreover, it formed the basis for achieving quantitative pore pressure inferences from seismic velocity measurements. It further allowed for the development of projective velocity-change models for hypothetical production scenarios and predictions of site amplification change due to seasonal temperature variations and climate change. Last, it offered a reconciliation of laboratory and field experiments investigating temperature-induced seismic velocity changes.

In Chapter 2, I formulated a theory that connects variations in seismic velocity to fluctuations in pore pressure and vertical stress. This theory was developed by combining an established relationship between seismic velocity and induced stress, which was derived from fundamental principles (Tromp & Trampert, 2018), with fundamental hydrology and geomechanics. The derivation resulted in physics-based relationships describing changes in body-wave velocities as functions of pore pressure, vertical compressional stress, and elastic parameters.

To assess the validity of this newly derived relationship, I modeled surface-wave phase-velocity variations using pressure head measurements (Dinoloket, 2022), the newly derived relationship and the adjoint method (Hawkins, 2018). Independently, I computed actual surface-wave phase-velocity variations by applying passive image interferometry (Sens-Schönfelder & Wegler, 2006) to seismic noise data collected in the province of Groningen in the Netherlands (KNMI, 1993). The remarkable agreement between the model predictions and the observed data confirms the plausibility of the proposed theory. The physics-based understanding of seismic velocity changes opens up new possibilities for improved pore pressure monitoring and imaging. While the physics-based relationships have been successfully validated for pore pressure and shear-wave velocity, the validations for vertical stress and compressional-wave velocity are still pending.

In Chapter 3, I exploited seismic velocity measurements to infer four-dimensional pore pressure models for the shallow subsurface beneath Groningen. I established that pore pressure sensitivity kernels can serve as a direct link between surface-wave phase-velocity variations and pore pressure changes as a function of depth. Notably, in the Groningen region of the Netherlands, the highest sensitivity to pore pressure changes is concentrated in the very shallow subsurface: within the top 200 m. This sensitivity to pore pressure variations decays considerably faster with depth compared to the sensitivity to changes in elastic parameters. The observation of a rapidly decreasing pore pressure sensitivity can be extended to pressure sensitivities in general, as shear-wave velocity changes can be connected to pressure changes via the fraction $\mu'_p/(2\mu)$ (Equation 2.4). Qualitatively, this observation can be generalized for all unconsolidated sediments, since the shear modulus gen-

erally increases with depth, while its pressure derivative decreases with depth for these materials.

My research demonstrated that it is possible to infer depth-dependent pore pressure variations using pore pressure sensitivity kernels and frequency-dependent surface-wave phase-velocity variations. The inversion of surface-wave phase-velocity variations in the subsurface of Groningen resulted in a four-dimensional model of pore pressure variation. The close alignments with independent measurements of pore pressure variations and hydrological characteristics in the area (Grondwatertools, 2022) indicate the reliability of this quantitative inference. The demonstration of four-dimensional pore pressure monitoring using surface-wave phase-velocity changes illustrates the technological advancements that can be achieved through a physics-based approach.

In Chapter 4, I investigated the feasibility of using surface-wave phase-velocity variations for monitoring pore pressure developments in deeper reservoirs. To accomplish this, I expanded the pore pressure sensitivity kernels to encompass the depth ranges of the Harlingen and Groningen gas reservoirs. I conducted forward modeling exercises to assess how surface-wave phase velocities would change in response to hypothetical production scenarios.

The results revealed that for the Harlingen reservoir (1 km depth), Rayleigh-wave velocity changes are big enough to be detected with a yearly resolution using passive image interferometry. Inverse modeling of a perturbed forward velocity-change model uncovered that, due to measurement uncertainties, minor fluctuations in shallow pore pressure however have a significant impact on the uncertainties of inferred reservoir pressure models. Specifically, the measurements of surface-wave phase-velocity variations detailed in Chapter 3 introduced an uncertainty of 0.2 MPa in the reservoir pressure estimation. Nevertheless, this level of uncertainty remains sufficiently small to effectively capture pore pressure developments linked to production activities. Therefore, reservoir pressure monitoring using surface-wave phase-velocity changes appears feasible for shallow reservoirs like the Harlingen field.

For the Groningen reservoir (3 km depth), however, production-related variations in surface-wave phase velocities fall within the range of measurement uncertainties. Production-related velocity changes could be retrieved for large pore pressure changes ($du \sim 1$ MPa) in a thick part of the reservoir (~ 300 m), if the measurement uncertainty of low-frequency velocity-change measurements would be decreased by a factor of 5-10. For a thinner part of the reservoir, or for smaller pore pressure changes, the accuracy would need to be improved even further. For the given measurement uncertainties, pore pressure monitoring in the Groningen reservoir is not feasible using surface-wave phase-velocity changes, even when velocity measurements are not contaminated with shallow-origin velocity variations.

Chapter 5 delved into physics determining the temperature sensitivity of seismic properties within the shallow unconsolidated subsurface. I derived physics-based relationships for temperature-induced changes in body-wave velocities, and considered three underlying mechanisms: the intrinsic temperature dependency of the elastic moduli, thermally-induced pressure, and thermally-induced volumet-

ric strain. A series of physics-based models revealed how dynamic surface temperatures affect subsurface temperature variations, induce thermal stresses and strains, and cause changes in body-wave velocities, surface-wave phase velocities, and site amplifications. The mechanism of thermally-induced strain appeared negligible with respect to the mechanisms of thermally-induced pressure and the moduli's intrinsic temperature dependencies. The competition between the two dominant mechanisms for velocity change reconciles field and laboratory experiments regarding temperature-induced seismic velocity changes, and determines whether site amplification is more pronounced during summer or winter.

I considered models for the shallow unconsolidated sediments in the subsurface of Groningen, where subsurface temperature fluctuations are driven by seasonal atmospheric temperature fluctuations roughly between −5 and 30 °C. For these models, I predicted seasonal temperature-induced changes in body-wave velocities up to 8%, high-frequency surface-wave phase-velocity variations of approximately 1-2%, and relative changes in site amplification in the order of 4%.

To gain insight into the response of the surface-wave phase velocity to temperature variations, I computed temperature sensitivity kernels for surface-wave phase velocities. Although the temperature sensitivity of pressure increases with depth, the temperature sensitivities of body and surface-wave phase velocities through thermally-induced pressure still decrease with depth. This can be explained by the rapid decay of pressure sensitivities of shear-wave velocities.

When comparing variations in subsurface temperature and pore pressure, there are similarities and differences. Depth-dependent changes in both properties can be connected to frequency-dependent surface-wave phase-velocity variations through sensitivity kernels. Sensitivities to both temperature and pore pressure show a rapid decay with depth, much faster than the sensitivity to changes in elastic parameters. However, the temperature sensitivity kernels decrease slightly slower with depth, since the sensitivity of pressure to changes in temperature increases with depth, while the sensitivity of pressure to changes in pore pressure is not depth dependent (i.e., −1 at all depths for a Biot constant of $\alpha_B \approx 1$). For the studied cases, both temperature and pore pressure variations are the result of a diffusion process, driven by seasonal variations at the surface. Pore pressure diffusion occurs relatively quickly, reaching confined aquifers at depths of 200 m within a few days. In contrast, heat diffusion is considerably slower, with a penetration depth of approximately 20 m achieved over the course of a year. The variation in penetration depth results in surface-wave phase-velocity changes being primarily influenced by seasonal fluctuations in pore pressure for frequencies below 2 Hz. For higher frequencies, I anticipate surface-wave phase-velocity variations driven by a mixture of pore pressure and temperature change.

6.2. Outlook

Throughout this study, I modeled velocity variations using many models of physical parameters (e.g., Figure 5.2). Whereas for some parameters very detailed models were available (e.g., compressional- and shear-wave velocities and density), other parameters needed to be estimated. Especially the pressure and temperature

derivatives of the bulk and shear moduli are uncertain. To achieve greater accuracy, it is imperative to establish precise models through new laboratory experiments for these parameters, especially for complicated unconsolidated materials.

In Chapter 3, I showed that four-dimensional pore pressure variations can be inferred from seismic velocity measurements. In the Groningen subsurface this is possible since natural pore pressure variations are the dominant source for low-frequency (<2 Hz) seismic velocity changes. Nevertheless, seismic velocity variations result from a complex interplay of multiple factors. When there is more than one dominant source for seismic velocity change, as we expect at higher frequencies, we can still forward model seismic velocity changes. However, the inverse problem is highly underdetermined. A proper inversion scheme therefore requires alternative measurements and prior information.

For retrieving seismic velocity variations, I used passive image interferometry. Specifically, in the second step of this method, that is, coda wave interferometry, I used the stretching method to estimate seismic velocity variations from coda waves. One of the advantages of the stretching method is the ability to detect velocity changes with high precision. This allows for the detection of weak velocity changes. However, using this method we can only localize velocity variations with low spatial resolutions. Both for monitoring natural pore pressure variations in the shallow subsurface (Chapter 3) and for deeper reservoir monitoring (Chapter 4), spatial localization would benefit the interpretation. It is worth investigating whether higher spatial resolutions can be achieved by using direct arrivals, lower temporal resolutions or active sources. It is however important to keep in mind that the low-frequency measurement uncertainties need to be adequately small to be able to infer deeper reservoir pressure changes from surface-wave phase-velocity variations.

Another possibility for improving the spatial resolution is to consider velocity changes as a function of arrival time in the coda. By considering the sensitivities of different wave types at different arrival times and frequencies (Margerin et al., 2016; Obermann et al., 2013b), one can perform a higher-resolution spatial inversion of phase-velocity changes (James et al., 2019; Mao et al., 2022). This can be achieved using the moving window cross-spectral method (Clarke et al., 2011; James et al., 2017), dynamic time warping (Mikesell et al., 2015), or the wavelet method (Mao et al., 2020), but also by choosing multiple small time windows using the stretching method (Lobkis & Weaver, 2003). Knowing the sensitivities of coda-wave arrival times to localized phase-velocity changes, and the local sensitivities of phase-velocities to depth-dependent pore pressure variations, one can construct pore pressure sensitivity kernels for velocity changes as a function of arrival time in the coda. This allows for a one-step inversion for a high-resolution 4D pore pressure model, based on velocity variations in different parts of the coda.

Chapter 5 considered seismic velocity variations, driven by seasonal temperature fluctuations at the surface. I predicted that seasonal temperature variations have a measurable effect on the seismic velocities. Due to the small penetration depth of heat diffusion, however, the temperature variations only affected body-wave velocities in a depth range of about 30 m, and surface-wave phase veloci-

ties above 2 Hz. It is worthwhile to investigate how temperature variations driven by other processes affect seismic velocities, and examine whether it is feasible to monitor changes in temperature and thermal stress using seismic velocities. One other source for temperature variations can be found in high-temperature aquifer thermal energy storage (HT-ATES) systems. To assess the seismic changes induced by such systems, certain assumptions made in Chapter 5 need to be reconsidered. In particular, one must factor in horizontal heat transport through diffusion and advection, along with horizontal strain and vertical stress. Stricker et al. (2023) have demonstrated that for an HT-ATES system, the evolution of thermal stress, thermal strain, and pore pressure can be modeled semi-analytically (van Wees et al., 2019) for injection and production scenarios. The resulting body-wave velocity changes can be modeled as a function of temperature, thermally-induced pressure and thermally-induced volumetric strain using Equation 5.25, and as a function of pore pressure using Equations 2.12, 2.17 and 2.18.

This doctoral research focused on seismic monitoring of the saturated subsurface. In the Groningen region of the Netherlands, the groundwater table can be found at approximately 1 m depth, making the vadose zone, the unsaturated subsurface, relatively small. As the vadose zone facilitates water exchange between surface and subsurface water (Vereecken et al., 2008), it determines the well-being of ecosystems and the recharging of groundwater reserves (Dobriyal et al., 2012), hence it may be interesting to study seismic wave propagation through this layer. It has been shown that water seepage through the vadose zone can measurably affect seismic velocities (e.g., Blazevic et al., 2020). To assess where and how changes in the vadose zone can be monitored using seismic velocity variations, all properties affecting seismic velocities need to be considered, including capillary stress, adsorptive stress, atmospheric pressure, water temperature, density and phase transitions (Linneman et al., 2021; Mordret et al., 2022). A physics-based analysis can then determine which mechanisms are dominant in the vadose zone, and which properties can potentially be inferred from seismic velocity measurements.

Glossary

This glossary lists the symbols and definitions used throughout this thesis, organized by the Greek and Roman alphabet. It is important to note that the symbols and notations used in this thesis may differ from those in the published articles upon which the chapters are based.

α_B	Biot constant [-]
α_d	Thermal diffusivity [m^2/s]
α_T	Thermal expansion coefficient [$°C^{-1}$]
δ_{ij}	Kronecker delta yielding 1 for $i = j$ and 0 otherwise
ϵ	Stretching factor [-]
$\boldsymbol{\epsilon}/\epsilon_{ij}$	Strain tensor [-] (defined positive for increased volume)
κ	Bulk modulus [Pa]
κ'_p	Pressure derivative of the bulk modulus [-]
κ'_T	Temperature derivative of the bulk modulus [Pa/°C]
μ	Shear modulus [Pa]
μ'_p	Pressure derivative of the shear modulus [-]
μ'_T	Temperature derivative of the shear modulus [Pa/°C]
ρ	Mass density [kg/m^3]
σ_q	Standard deviation of the sampling distribution of property q
$\boldsymbol{\sigma}/\sigma_{ij}$	Stress tensor [Pa] (defined negative for compression)
$\tilde{\boldsymbol{\sigma}}/\tilde{\sigma}_{ij}$	Effective stress tensor $\tilde{\boldsymbol{\sigma}} = \boldsymbol{\sigma} + \alpha_B u \boldsymbol{I}$ [Pa]
$\boldsymbol{\tau}/\tau_{ij}$	Deviatoric stress tensor $\boldsymbol{\tau} = \boldsymbol{\sigma} - \frac{1}{3} tr(\boldsymbol{\sigma}) \boldsymbol{I}$ [Pa]
ϕ	Porosity [-]
ω	Angular frequency [rad/s]

$\hat{\boldsymbol{a}}$	Unitvector direction of motion [-]
c	Surface-wave phase velocity [m/s]
c_R	Rayleigh-wave phase velocity [m/s]
c_L	Love-wave phase velocity [m/s]
CC	Correlation coefficient
$\boldsymbol{C_d}$	Data covariance
$\boldsymbol{C_m}$	Model covariance
$d\ln v$	Alternative notation for relative velocity change: $d\ln v = \frac{dv}{v}$
$\boldsymbol{d}$	Data coefficients
f	Frequency [Hz]
F_p	Amplification factor for compressional waves [-]
F_s	Amplification factor for shear waves [-]
g	Gravitational acceleration [m/s^2]
$\boldsymbol{G}$	Forward operator
h	Pressure head [m]
H	Cross-coherence [-]
$\boldsymbol{I}$	Identity matrix [-]
k	Wave number [m^{-1}]
$\hat{\boldsymbol{k}}$	Unitvector direction of propagation [-]
K_{v_p}	Compressional-wave velocity sensitivity kernel for surface waves [m^{-1}]
K_{v_s}	Shear-wave velocity sensitivity kernel for surface waves [m^{-1}]
K_ρ	Density sensitivity kernel for surface waves [m^{-1}]
K_T	Temperature sensitivity kernel for surface waves [°C^{-1}m^{-1}]
K_u	Pore pressure sensitivity kernel for surface waves [Pa^{-1}m^{-1}]
$\boldsymbol{m}$	Model coefficients
p	Pressure $p = -\frac{1}{3}tr(\boldsymbol{\sigma})$ [Pa]
$\boldsymbol{R}$	Resolution matrix
S	Cubic natural spline function [-]
T	Temperature [°C]
t	Time [s]
u	Pore pressure [Pa]
v	Seismic velocity in general [m/s]
v_p	Compressional-wave velocity [m/s]
v_s	Shear-wave velocity [m/s]
$\hat{w}$	Ground velocity in the frequency domain [m/s]
x	Horizontal distance [m]
y	Horizontal distance [m]
z	Depth [m]

Bibliography

Andajani, R. D., Tsuji, T., Snieder, R., & Ikeda, T. (2020). Spatial and temporal influence of rainfall on crustal pore pressure based on seismic velocity monitoring. *Earth, Planets and Space*, *72*(1), 1–17.

Angelov, P. V. (2009). *4D seismic reservoir characterization, integrated with geomechanical modelling* (Doctoral dissertation). Delft University of Technology.

Bard, P.-Y., Campillo, M., Chavez-Garcia, F., & Sanchez-Sesma, F. (1988). The Mexico earthquake of September 19, 1985 – A theoretical investigation of large- and small-scale amplification effects in the Mexico City Valley. *Earthquake Spectra*, *4*(3), 609–633.

Bense, V., & Kooi, H. (2004). Temporal and spatial variations of shallow subsurface temperature as a record of lateral variations in groundwater flow. *Journal of Geophysical Research: Solid Earth*, *109*(B4).

Bentil, O. T., & Zhou, C. (2022). Effects of temperature and thermal cycles on the elastic shear modulus of saturated clay. *Journal of Geotechnical and Geoenvironmental Engineering*, *148*(7), 06022006.

Ben-Zion, Y., & Allam, A. (2013). Seasonal thermoelastic strain and postseismic effects in Parkfield borehole dilatometers. *Earth and Planetary Science Letters*, *379*, 120–126.

Ben-Zion, Y., & Leary, P. (1986). Thermoelastic strain in a half-space covered by unconsolidated material. *Bulletin of the Seismological Society of America*, *76*(5), 1447–1460.

Berger, J. (1975). A note on thermoelastic strains and tilts. *Journal of Geophysical Research*, *80*(2), 274–277.

Bièvre, G., Franz, M., Larose, E., Carrière, S., Jongmans, D., & Jaboyedoff, M. (2018). Influence of environmental parameters on the seismic velocity changes in a clayey mudflow (Pont-Bourquin Landslide, Switzerland). *Engineering Geology*, *245*, 248–257.

Birch, F. (1943). Elasticity of igneous rocks at high temperatures and pressures. *Bulletin of the Geological Society of America*, *54*(2), 263–286.

Blazevic, L. A., Bodet, L., Pasquet, S., Linde, N., Jougnot, D., & Longuevergne, L. (2020). Time-lapse seismic and electrical monitoring of the vadose zone during a controlled infiltration experiment at the ploemeur hydrological observatory, france. *Water*, *12*(5), 1230.

Bobrowski, A., Drożyński, D., Jakubski, J., Szumera, M., Kaczmarska, K., & Grabowska, B. (2018). Thermal deformation of moulding and core sands with an inorganic binder containing a relaxation additive. *Archives of Foundry Engineering*, *18*.

Bommer, J. J., Stafford, P. J., Edwards, B., Dost, B., van Dedem, E., Rodriguez-Marek, A., Kruiver, P., van Elk, J., Doornhof, D., & Ntinalexis, M. (2017). Framework for a ground-motion model for induced seismic hazard and risk analysis in the Groningen gas field, the Netherlands. *Earthquake Spectra*, *33*(2), 481–498.

Bourne, S. J., Oates, S. J., & van Elk, J. (2018). The exponential rise of induced seismicity with increasing stress levels in the Groningen gas field and its implications for controlling seismic risk. *Geophysical Journal International*, *213*(3), 1693–1700.

Bradley, B. A. (2012). Strong ground motion characteristics observed in the 4 September 2010 Darfield, New Zealand earthquake. *Soil Dynamics and Earthquake Engineering*, *42*, 32–46.

Brenguier, F., Campillo, M., Hadziioannou, C., Shapiro, N. M., Nadeau, R. M., & Larose, E. (2008a). Postseismic relaxation along the San Andreas Fault at Parkfield from continuous seismological observations. *Science*, *321*(5895), 1478–1481.

Brenguier, F., Courbis, R., Mordret, A., Campman, X., Boué, P., Chmiel, M., Takano, T., Lecocq, T., van der Veen, W., Postif, S., et al. (2020). Noise-based ballistic wave passive seismic monitoring. – Part 1: Body waves. *Geophysical Journal International*, *221*(1), 683–691.

Brenguier, F., Boué, P., Ben-Zion, Y., Vernon, F., Johnson, C. W., Mordret, A., Coutant, O., Share, P.-E., Beaucé, E., Hollis, D., et al. (2019). Train traffic as a powerful noise source for monitoring active faults with seismic interferometry. *Geophysical Research Letters*, *46*(16), 9529–9536.

Brenguier, F., Clarke, D., Aoki, Y., Shapiro, N. M., Campillo, M., & Ferrazzini, V. (2011). Monitoring volcanoes using seismic noise correlations. *Comptes Rendus Geoscience*, *343*(8-9), 633–638.

Brenguier, F., Shapiro, N. M., Campillo, M., Ferrazzini, V., Duputel, Z., Coutant, O., & Nercessian, A. (2008b). Towards forecasting volcanic eruptions using seismic noise. *Nature Geoscience*, *1*(2), 126.

Brenguier, F., Shapiro, N. M., Campillo, M., Nercessian, A., & Ferrazzini, V. (2007). 3-D surface wave tomography of the Piton de la Fournaise volcano using seismic noise correlations. *Geophysical Research Letters*, *34*(2).

Cessaro, R. K. (1994). Sources of primary and secondary microseisms. *Bulletin of the Seismological Society of America*, *84*(1), 142–148.

Christensen, N. I. (1979). Compressional wave velocities in rocks at high temperatures and pressures, critical thermal gradients, and crustal low-velocity zones. *Journal of Geophysical Research: Solid Earth*, *84*(B12), 6849–6857.

Clarke, D., Zaccarelli, L., Shapiro, N., & Brenguier, F. (2011). Assessment of resolution and accuracy of the moving window cross spectral technique for monitoring crustal temporal variations using ambient seismic noise. *Geophysical Journal International*, *186*(2), 867–882.

Clements, T., & Denolle, M. (2023). The seismic signature of California's earthquakes, droughts, and floods. *Journal of Geophysical Research: Solid Earth*, *128*(1), e2022JB025553.

Clements, T., & Denolle, M. A. (2018). Tracking groundwater levels using the ambient seismic field. *Geophysical Research Letters*, *45*(13), 6459–6465.

Colombero, C., Baillet, L., Comina, C., Jongmans, D., Larose, E., Valentin, J., & Vinciguerra, S. (2018). Integration of ambient seismic noise monitoring, displacement and meteorological measurements to infer the temperature-controlled long-term evolution of a complex prone-to-fall cliff. *Geophysical Journal International*, *213*(3), 1876–1897.

Curtis, A., Gerstoft, P., Sato, H., Snieder, R., & Wapenaar, K. (2006). Seismic interferometry – Turning noise into signal. *The Leading Edge*, *25*(9), 1082–1092.

Dandekar, D. P., & Ruoff, A. L. (1968). Temperature dependence of the elastic constants of calcite between 160 and 300 K. *Journal of Applied Physics*, *39*(13), 6004–6009.

de Jager, J., & Visser, C. (2017). Geology of the Groningen field – An overview. *Netherlands Journal of Geosciences*, *96*(5), s3–s15.

de Louw, P. G., Essink, G. O., Stuyfzand, P. J., & van der Zee, S. (2010). Upward groundwater flow in boils as the dominant mechanism of salinization in deep polders, the Netherlands. *Journal of Hydrology*, *394*(3-4), 494–506.

Díaz, J., Ruiz, M., Sánchez-Pastor, P. S., & Romero, P. (2017). Urban seismology: On the origin of earth vibrations within a city. *Scientific Reports*, *7*(1), 15296.

Dinoloket. (2022). Groundwater research – Borehole identification B08C0952. Dinoloket.nl [Last accessed: 7 September 2022].

Dobriyal, P., Qureshi, A., Badola, R., & Hussain, S. A. (2012). A review of the methods available for estimating soil moisture and its implications for water resource management. *Journal of Hydrology*, *458*, 110–117.

Dost, B., Ruigrok, E., & Spetzler, J. (2017). Development of seismicity and probabilistic hazard assessment for the Groningen gas field. *Netherlands Journal of Geosciences*, *96*(5), s235–s245.

Duputel, Z., Ferrazzini, V., Brenguier, F., Shapiro, N., Campillo, M., & Nercessian, A. (2009). Real time monitoring of relative velocity changes using ambient seismic noise at the Piton de la Fournaise volcano (La Réunion) from January 2006 to June 2007. *Journal of Volcanology and Geothermal Research*, *184*(1-2), 164–173.

Ermert, L. A., Cabral-Cano, E., Chaussard, E., Solano-Rojas, D., Quintanar, L., Morales Padilla, D., Fernández-Torres, E. A., & Denolle, M. A. (2023). Probing environmental and tectonic changes underneath Mexico City with the urban seismic field. *Solid Earth*, *14*(5), 529–549.

Fjær, E., Holt, R. M., Raaen, A., & Horsrud, P. (2008). *Petroleum related rock mechanics*. Elsevier.

Fokker, E. B., & Ruigrok, E. N. (2019). Quality parameters for passive image interferometry tested at the Groningen network. *Geophysical Journal International*, *218*(2), 1367–1378.

Fokker, E., Ruigrok, E., Hawkins, R., & Trampert, J. (2021). Physics-based relationship for pore pressure and vertical stress monitoring using seismic velocity variations. *Remote Sensing*, *13*(14), 2684.

Fokker, E., Ruigrok, E., Hawkins, R., & Trampert, J. (2022). Pore pressure monitoring in a chalk gas reservoir using surface-wave velocity variations. *1st EAGE/SBGf Workshop on Reservoir Monitoring and its Role in the Energy Transition*, *2022*(1), 1–5.

Fokker, E., Ruigrok, E., Hawkins, R., & Trampert, J. (2023). 4D physics-based pore pressure monitoring using passive image interferometry. *Geophysical Research Letters*, *50*(5).

Fokker, E., Ruigrok, E., & Trampert, J. (2024). On the temperature sensitivity of near-surface seismic wave speeds: Application to the Groningen region, the Netherlands. *Geophysical Journal International*, *in press*.

Fokker, E., Ruigrok, E., & Trampert, J. (in preparation). Monitoring anthropogenic fluctuations in reservoir pressure using surface-wave phase-velocity variations: A feasibility study. *In preparation for submission to Geophysical Prospecting*.

Fokker, P. A., & van Thienen-Visser, K. (2016). Inversion of double-difference measurements from optical leveling for the Groningen gas field. *International Journal of Applied Earth Observation and Geoinformation*, *49*, 1–9.

Grondwatertools. (2022). Groundwater head viewer. Grondwatertools.nl [Last accessed: 7 September 2022].

Hadziioannou, C., Larose, E., Coutant, O., Roux, P., & Campillo, M. (2009). Stability of monitoring weak changes in multiply scattering media with ambient noise correlation: Laboratory experiments. *The Journal of the Acoustical Society of America*, *125*(6), 3688–3695.

Hawkins, R. (2018). A spectral element method for surface wave dispersion and adjoints. *Geophysical Journal International*, *215*(1), 267–302.

Hettema, M. H., Jaarsma, B., Schroot, B. M., & van Yperen, G. C. (2017). An empirical relationship for the seismic activity rate of the Groningen gas field. *Netherlands Journal of Geosciences*, *96*(5), s149–s161.

Hillers, G., Campillo, M., & Ma, K.-F. (2014). Seismic velocity variations at TCDP are controlled by MJO driven precipitation pattern and high fluid discharge properties. *Earth and Planetary Science Letters*, *391*, 121–127.

Hofman, L., Ruigrok, E., Dost, B., & Paulssen, H. (2017). A shallow seismic velocity model for the Groningen area in the Netherlands. *Journal of Geophysical Research: Solid Earth*, *122*(10), 8035–8050.

Hussain, Y., Martinez-Carvajal, H., Condori, C., Uagoda, R., Cárdenas-Soto, M., Cavalcante, A. L. B., da Cunha, L. S., & Martino, S. (2019). Ambient seismic noise: A continuous source for the dynamic monitoring of landslides. *Terrae Didatica*, *15*, e019012–e019012.

Illien, L., Sens-Schönfelder, C., Andermann, C., Marc, O., Cook, K. L., Adhikari, L. B., & Hovius, N. (2022). Seismic velocity recovery in the subsurface: Transient damage and groundwater drainage following the 2015 Gorkha earthquake, Nepal. *Journal of Geophysical Research: Solid Earth*, e2021JB023402.

Jaeger, J. C., Cook, N. G., & Zimmerman, R. (2009). *Fundamentals of rock mechanics*. John Wiley & Sons.

James, S., Knox, H., Abbott, R., Panning, M., & Screaton, E. (2019). Insights into permafrost and seasonal active-layer dynamics from ambient seismic noise monitoring. *Journal of Geophysical Research: Earth Surface*.

James, S., Knox, H., Abbott, R., & Screaton, E. (2017). Improved moving window cross-spectral analysis for resolving large temporal seismic velocity changes in permafrost. *Geophysical Research Letters*, *44*(9), 4018–4026.

Jaya, M. S., Shapiro, S. A., Kristinsdóttir, L. H., Bruhn, D., Milsch, H., & Spangenberg, E. (2010). Temperature dependence of seismic properties in geothermal rocks at reservoir conditions. *Geothermics*, *39*(1), 115–123.

Juretzek, C., & Hadziioannou, C. (2016). Where do ocean microseisms come from? A study of Love-to-Rayleigh wave ratios. *Journal of Geophysical Research: Solid Earth*, *121*(9), 6741–6756.

Kern, H. (1978). The effect of high temperature and high confining pressure on compressional wave velocities in quartz-bearing and quartz-free igneous and metamorphic rocks. *Tectonophysics*, *44*(1-4), 185–203.

Kimman, W., Campman, X., & Trampert, J. (2012). Characteristics of seismic noise: Fundamental and higher mode energy observed in the northeast of the Netherlands. *Bulletin of the Seismological Society of America*, *102*(4), 1388–1399.

Knight, R., Dvorkin, J., & Nur, A. (1998). Acoustic signatures of partial saturation. *Geophysics*, *63*(1), 132–138.

KNMI. (1993). Netherlands seismic and acoustic network. Royal Netherlands Meteorological Institute (KNMI).

KNMI. (2023). Climatology: Hourly observations of the weather in the Netherlands [https://daggegevens.knmi.nl/klimatologie/uurgegevens; Last accessed: 17 August, 2023].

Kohnen, H. (1974). The temperature dependence of seismic waves in ice. *Journal of Glaciology*, *13*(67), 144–147.

Kole, P., Cannon, M., Tomic, J., & Bierman, S. (2020). *Analysis of and learnings from the first four years of in-situ strain data in Zeerijp-3A* (tech. rep.). Nederlandse Aardolie Maatschappij NV. Assen, the Netherlands.

Kooi, H. (2008). Spatial variability in subsurface warming over the last three decades; insight from repeated borehole temperature measurements in the Netherlands. *Earth and Planetary Science Letters*, *270*(1-2), 86–94.

Kruiver, P. P., van Dedem, E., Romijn, R., de Lange, G., Korff, M., Stafleu, J., Gunnink, J. L., Rodriguez-Marek, A., Bommer, J. J., van Elk, J., et al. (2017a). An integrated shear-wave velocity model for the Groningen gas field, the Netherlands. *Bulletin of Earthquake Engineering*, *15*(9), 3555–3580.

Kruiver, P. P., Wiersma, A., Kloosterman, F. H., de Lange, G., Korff, M., Stafleu, J., Busschers, F. S., Harting, R., Gunnink, J. L., Green, R. A., et al. (2017b). Characterisation of the Groningen subsurface for seismic hazard and risk modelling. *Netherlands Journal of Geosciences*, *96*(5), s215–s233.

Lakshtanov, D. L., Sinogeikin, S. V., & Bass, J. D. (2007). High-temperature phase transitions and elasticity of silica polymorphs. *Physics and Chemistry of Minerals*, *34*, 11–22.

Landrø, M., & Stammeijer, J. (2004). Quantitative estimation of compaction and velocity changes using 4D impedance and traveltime changes. *Geophysics*, *69*(4), 949–957.

Lecocq, T., Hicks, S. P., van Noten, K., van Wijk, K., Koelemeijer, P., de Plaen, R. S., Massin, F., Hillers, G., Anthony, R. E., Apoloner, M.-T., et al. (2020). Global quieting of high-frequency seismic noise due to COVID-19 pandemic lockdown measures. *Science*, *369*(6509), 1338–1343.

Lecocq, T., Longuevergne, L., Pedersen, H. A., Brenguier, F., & Stammler, K. (2017). Monitoring ground water storage at mesoscale using seismic noise: 30 years of continuous observation and thermo-elastic and hydrological modeling. *Scientific Reports*, *7*(1), 1–16.

Li, T., Gu, Y. J., Lawton, D. C., Gilbert, H., Macquet, M., Savard, G., Wang, J., Innanen, K. A., & Yu, N. (2022). Monitoring CO2 injection at the CaMI field research station using microseismic noise sources [e2022JB024719 2022JB024719]. *Journal of Geophysical Research: Solid Earth*, *127*(12), e2022JB024719.

Lindner, F., Wassermann, J., & Igel, H. (2021). Seasonal freeze-thaw cycles and permafrost degradation on Mt. Zugspitze (German/Austrian Alps) revealed by single-station seismic monitoring. *Geophysical Research Letters*, *48*(18), e2021GL094659.

Linneman, D. C., Strickland, C. E., & Mangel, A. R. (2021). Compressional wave velocity and effective stress in unsaturated soil: Potential application for monitoring moisture conditions in vadose zone sediments. *Vadose Zone Journal*, *20*(5), e20143.

Liu, C., Aslam, K., & Daub, E. (2020). Seismic velocity changes caused by water table fluctuation in the New Madrid seismic zone and Mississippi embayment. *Journal of Geophysical Research: Solid Earth*, *125*(8), e2020JB019524.

Liu, H., Liu, H., Xiao, Y., & McCartney, J. S. (2018). Effects of temperature on the shear strength of saturated sand. *Soils and Foundations*, *58*(6), 1326–1338.

Lobkis, O. I., & Weaver, R. L. (2003). Coda-wave interferometry in finite solids: Recovery of P-to-S conversion rates in an elastodynamic billiard. *Physical Review Letters*, *90*(25), 254302.

Madley, M., Yates, A., Savage, M., Wang, W., Okada, T., Matsumoto, S., Iio, Y., & Jacobs, K. (2022). Velocity changes around the Kaikōura earthquake ruptures from ambient noise cross-correlations. *Geophysical Journal International*, *229*(2), 1357–1371.

Mainsant, G., Larose, E., Brönnimann, C., Jongmans, D., Michoud, C., & Jaboyedoff, M. (2012). Ambient seismic noise monitoring of a clay landslide: Toward failure prediction. *Journal of Geophysical Research: Earth Surface*, *117*(F1).

Makus, P., Sens-Schönfelder, C., Illien, L., Walter, T. R., Yates, A., & Tilmann, F. (2023). Deciphering the whisper of volcanoes: Monitoring velocity changes at Kamchatka's Klyuchevskoy group with fluctuating noise fields. *Journal of Geophysical Research: Solid Earth*, *128*(4), e2022JB025738.

Mao, S., Campillo, M., van der Hilst, R. D., Brenguier, F., Stehly, L., & Hillers, G. (2019). High temporal resolution monitoring of small variations in crustal

strain by dense seismic arrays. *Geophysical Research Letters*, *46*(1), 128–137.

Mao, S., Lecointre, A., van der Hilst, R. D., & Campillo, M. (2022). Space-time monitoring of groundwater fluctuations with passive seismic interferometry. *Nature Communications*, *13*(1), 1–9.

Mao, S., Mordret, A., Campillo, M., Fang, H., & van der Hilst, R. D. (2020). On the measurement of seismic traveltime changes in the time–frequency domain with wavelet cross-spectrum analysis. *Geophysical Journal International*, *221*(1), 550–568.

Margerin, L., Planès, T., Mayor, J., & Calvet, M. (2016). Sensitivity kernels for coda-wave interferometry and scattering tomography: Theory and numerical evaluation in two-dimensional anisotropically scattering media. *Geophysical Journal International*, *204*(1), 650–666.

Martins, J. E., Weemstra, C., Ruigrok, E., Verdel, A., Jousset, P., & Hersir, G. (2020). 3D S-wave velocity imaging of Reykjanes Peninsula high-enthalpy geothermal fields with ambient-noise tomography. *Journal of Volcanology and Geothermal Research*, *391*, 106685.

Maxwell, S., & Urbancic, T. (2005). The potential role of passive seismic monitoring for real-time 4D reservoir characterization. *SPE Reservoir Evaluation & Engineering*, *8*(01), 70–76.

McKinstry, H. A. (1965). Thermal expansion of clay minerals. *American Mineralogist*, *50*(1-2), 212–222.

Mikesell, T. D., Malcolm, A. E., Yang, D., & Haney, M. M. (2015). A comparison of methods to estimate seismic phase delays: Numerical examples for coda wave interferometry. *Geophysical Journal International*, *202*(1), 347–360.

Minato, S., Tsuji, T., Ohmi, S., & Matsuoka, T. (2012). Monitoring seismic velocity change caused by the 2011 Tohoku-oki earthquake using ambient noise records. *Geophysical Research Letters*, *39*(9).

Mordret, A., Jolly, A., Duputel, Z., & Fournier, N. (2010). Monitoring of phreatic eruptions using interferometry on retrieved cross-correlation function from ambient seismic noise: Results from Mt. Ruapehu, New Zealand. *Journal of Volcanology and Geothermal Research*, *191*(1-2), 46–59.

Mordret, A., Landès, M., Shapiro, N., Singh, S., Roux, P., & Barkved, O. (2013). Near-surface study at the Valhall oil field from ambient noise surface wave tomography. *Geophysical Journal International*, *193*(3), 1627–1643.

Mordret, A., Gradon, C., & Brenguier, F. (2022). Seismic monitoring of the vadose zone in arid environments. *AGU Fall Meeting*, *2022*.

Mordret, A., Courbis, R., Brenguier, F., Chmiel, M., Garambois, S., Mao, S., Boué, P., Campman, X., Lecocq, T., van der Veen, W., et al. (2020). Noise-based ballistic wave passive seismic monitoring – Part 2: Surface waves. *Geophysical Journal International*, *221*(1), 692–705.

Nakata, N., & Snieder, R. (2012). Estimating near-surface shear wave velocities in Japan by applying seismic interferometry to KiK-net data. *Journal of Geophysical Research: Solid Earth*, *117*(B1).

Nakata, N., Snieder, R., Tsuji, T., Larner, K., & Matsuoka, T. (2011). Shear wave imaging from traffic noise using seismic interferometry by cross-coherence. *Geophysics*, *76*(6), SA97–SA106.

Nepveu, M., van Thienen-Visser, K., & Sijacic, D. (2016). Statistics of seismic events at the Groningen field. *Bulletin of Earthquake Engineering*, *14*(12), 3343–3362.

Nowacek, D. P., Clark, C. W., Mann, D., Miller, P. J., Rosenbaum, H. C., Golden, J. S., Jasny, M., Kraska, J., & Southall, B. L. (2015). Marine seismic surveys and ocean noise: Time for coordinated and prudent planning. *Frontiers in Ecology and the Environment*, *13*(7), 378–386.

Ntinalexis, M., Kruiver, P. P., Bommer, J. J., Ruigrok, E., Rodriguez-Marek, A., Edwards, B., Pinho, R., Spetzler, J., Hernandez, E. O., Pefkos, M., et al. (2023). A database of ground motion recordings, site profiles, and amplification factors from the Groningen gas field in the Netherlands. *Earthquake Spectra*, *39*(1), 687–701.

Nye, J. F. (1985). *Physical properties of crystals: Their representation by tensors and matrices*. Oxford University Press.

Obermann, A., Planès, T., Larose, E., & Campillo, M. (2013a). Imaging preeruptive and coeruptive structural and mechanical changes of a volcano with ambient seismic noise. *Journal of Geophysical Research: Solid Earth*, *118*(12), 6285–6294.

Obermann, A., Planès, T., Larose, E., Sens-Schönfelder, C., & Campillo, M. (2013b). Depth sensitivity of seismic coda waves to velocity perturbations in an elastic heterogeneous medium. *Geophysical Journal International*, *194*(1), 372–382.

Ohno, I. (1995). Temperature variation of elastic properties of α-quartz up to the α-β transition. *Journal of Physics of the Earth*, *43*(2), 157–169.

Olivier, G., Brenguier, F., Carey, R., Okubo, P., & Donaldson, C. (2019). Decrease in seismic velocity observed prior to the 2018 eruption of Kīlauea volcano with ambient seismic noise interferometry. *Geophysical Research Letters*, *46*(7), 3734–3744.

Olivier, G., Brenguier, F., de Wit, T., & Lynch, R. (2017). Monitoring the stability of tailings dam walls with ambient seismic noise. *The Leading Edge*, *36*(4), 350a1–350a6.

Orlander, T., Andreassen, K. A., & Fabricius, I. L. (2021). Effect of temperature on stiffness of sandstones from the deep North Sea basin. *Rock Mechanics and Rock Engineering*, *54*(1), 255–288.

Ouellet, S. M., Dettmer, J., Olivier, G., DeWit, T., & Lato, M. (2022). Advanced monitoring of tailings dam performance using seismic noise and stress models. *Communications Earth & Environment*, *3*(1), 301.

Park, C. B., Miller, R. D., Xia, J., et al. (1998). Imaging dispersion curves of surface waves on multi-channel record. *1998 SEG Annual Meeting*.

Planès, T., Rittgers, J. B., Mooney, M. A., Kanning, W., & Draganov, D. (2017). Monitoring the tidal response of a sea levee with ambient seismic noise. *Journal of Applied Geophysics*, *138*, 255–263.

Pörtner, H.-O., Roberts, D. C., Adams, H., Adelekan, I., Adler, C., Adrian, R., Aldunce, P., Ali, E., Begum, R. A., Bednar-Friedl, B., et al. (2023). IPCC: Technical summary. *Climate Change 2022: Impacts, Adaptation and Vulnerability*, 37–118.

Radkovskỳ, F., Gawronová, M., Merta, V., Lichỳ, P., Kroupová, I., Nguyenová, I., Kielar, Š., Folta, M., Bradáč, J., & Kocich, R. (2022). Effect of the composition of hybrid sands on the change in thermal expansion. *Materials*, *15*(17), 6180.

Ratdomopurbo, A., & Poupinet, G. (1995). Monitoring a temporal change of seismic velocity in a volcano: Application to the 1992 eruption of Mt. Merapi (Indonesia). *Geophysical Research Letters*, *22*(7), 775–778.

Rawlinson, N., Fichtner, A., Sambridge, M., & Young, M. K. (2014). Seismic tomography and the assessment of uncertainty. *Advances in Geophysics*, *55*, 1–76.

Richter, T., Sens-Schönfelder, C., Kind, R., & Asch, G. (2014). Comprehensive observation and modeling of earthquake and temperature-related seismic velocity changes in northern Chile with passive image interferometry. *Journal of Geophysical Research: Solid Earth*, *119*(6), 4747–4765.

Rivet, D., Brenguier, F., & Cappa, F. (2015). Improved detection of preeruptive seismic velocity drops at the Piton de la Fournaise volcano. *Geophysical Research Letters*, *42*(15), 6332–6339.

Rodriguez-Marek, A., Kruiver, P. P., Meijers, P., Bommer, J. J., Dost, B., van Elk, J., & Doornhof, D. (2017). A regional site-response model for the Groningen gas field. *Bulletin of the Seismological Society of America*, *107*(5), 2067–2077.

Romijn, R. (2017). *Groningen velocity model 2017* (tech. rep.). Nederlandse Aardolie Maatschappij NV. Assen, the Netherlands.

Roumelioti, Z., Hollender, F., & Guéguen, P. (2020). Rainfall-induced variation of seismic waves velocity in soil and implications for soil response: What the ARGONET (Cephalonia, Greece) vertical array data reveal. *Bulletin of the Seismological Society of America*, *110*(2), 441–451.

Ruigrok, E., Rodriguez-Marek, A., Edwards, B., Kruiver, P., Dost, B., & Bommer, J. (2022). Derivation of a near-surface damping model for the Groningen gas field. *Geophysical Journal International*, *230*(2), 776–795.

Rutten, M. M., Steele-Dunne, S. C., Judge, J., & van de Giesen, N. (2010). Understanding heat transfer in the shallow subsurface using temperature observations. *Vadose Zone Journal*, *9*(4), 1034–1045.

Salvermoser, J., Hadziioannou, C., & Stähler, S. C. (2015). Structural monitoring of a highway bridge using passive noise recordings from street traffic. *The Journal of the Acoustical Society of America*, *138*(6), 3864–3872.

Sánchez-Pastor, P., Obermann, A., Reinsch, T., Ágústsdóttir, T., Gunnarsson, G., Tómasdóttir, S., Hjörleifsdóttir, V., Hersir, G., Ágústsson, K., & Wiemer, S. (2021). Imaging high-temperature geothermal reservoirs with ambient seismic noise tomography, a case study of the Hengill geothermal field, SW Iceland. *Geothermics*, *96*, 102207.

Sánchez-Pastor, P., Obermann, A., & Schimmel, M. (2018). Detecting and locating precursory signals during the 2011 El Hierro, Canary Islands, submarine eruption. *Geophysical Research Letters*, *45*(19), 10, 288–10, 297.

Sánchez-Pastor, P., Obermann, A., Schimmel, M., Weemstra, C., Verdel, A., & Jousset, P. (2019). Short-and long-term variations in the Reykjanes geothermal reservoir from seismic noise interferometry. *Geophysical Research Letters*, *46*(11), 5788–5798.

Schatz, B., & Bandiziol, D. (2014). *Harlingen subsidence study* (tech. rep.). Vermilion.

Sens-Schönfelder, C., & Wegler, U. (2006). Passive image interferometry and seasonal variations of seismic velocities at Merapi Volcano, Indonesia. *Geophysical Research Letters*, *33*(21).

Sens-Schönfelder, C., & Wegler, U. (2011). Passive image interferometry for monitoring crustal changes with ambient seismic noise. *Comptes Rendus Geoscience*, *343*(8-9), 639–651.

Sleeman, R., & de Zeeuw-van Dalfsen, E. (2020). Cross-correlation analysis of long-term ambient seismic-noise recordings in the Caribbean Netherlands to monitor the volcanoes on Saba and St. Eustatius. *Bulletin of the Seismological Society of America*, *110*(5), 2541–2558.

Smith, J. D., Avouac, J.-P., White, R. S., Copley, A., Gualandi, A., & Bourne, S. (2019). Reconciling the long-term relationship between reservoir pore pressure depletion and compaction in the Groningen region. *Journal of Geophysical Research: Solid Earth*, *124*(6), 6165–6178.

Snieder, R. (2006). The theory of coda wave interferometry. *Pure and Applied Geophysics*, *163*(2), 455–473.

Snieder, R., Grêt, A., Douma, H., & Scales, J. (2002). Coda wave interferometry for estimating nonlinear behavior in seismic velocity. *Science*, *295*(5563), 2253–2255.

Stehly, L., Campillo, M., Froment, B., & Weaver, R. L. (2008). Reconstructing Green's function by correlation of the coda of the correlation (C3) of ambient seismic noise. *Journal of Geophysical Research: Solid Earth (1978–2012)*, *113*(B11).

Stricker, K., Egert, R., Fokker, P., Vardon, P. J., van Wees, J. D., Schill, E., & Kohl, T. (2023). Risk assessment of high-temperature heat storage (HT-ATES) at the DeepStor demonstrator site. *EGU General Assembly*, *2023*.

Svidró, J., Diószegi, A., & Svidró, J. T. (2020). The origin of thermal expansion differences in various size fractions of silica sand. *International Journal of Cast Metals Research*, *33*(6), 242–249.

Tarantola, A. (2005). *Inverse problem theory and methods for model parameter estimation*. Society for Industrial Mathematics.

Ter Voorde, M., van Balen, R., Luijendijk, E., & Kooi, H. (2014). Weichselian and Holocene climate history reflected in temperatures in the upper crust of the Netherlands. *Netherlands Journal of Geosciences*, *93*(3), 107–117.

Toledo, T., Obermann, A., Verdel, A., Martins, J. E., Jousset, P., Mortensen, A. K., Erbas, K., & Krawczyk, C. M. (2022). Ambient seismic noise monitoring

and imaging at the Theistareykir geothermal field (Iceland). *Journal of Volcanology and Geothermal Research*, *429*, 107590.

Trampert, J., Benzi, R., & Toschi, F. (2022). Implications of the statistics of seismicity recorded within the Groningen gas field. *Netherlands Journal of Geosciences*, *101*.

Tromp, J., & Trampert, J. (2018). Effects of induced stress on seismic forward modelling and inversion. *Geophysical Journal International*, *213*(2), 851–867.

Tsai, V. C. (2011). A model for seasonal changes in GPS positions and seismic wave speeds due to thermoelastic and hydrologic variations. *Journal of Geophysical Research: Solid Earth*, *116*(B4).

van der Vleut, B. C. M. (2019). *Characterizing the seismic signal of individual wind turbines in the Borgsweer area* (Master's thesis). Utrecht University.

van der Wal, O., & van Eijs, R. (2016). *Subsidence inversion on Groningen using levelling data only. NAM report EP201612206045* (tech. rep.). Nederlandse Aardolie Maatschappij NV.

van Eijs, R. M., & van der Wal, O. (2017). Field-wide reservoir compressibility estimation through inversion of subsidence data above the Groningen gas field. *Netherlands Journal of Geosciences*, *96*(5), s117–s129.

van Ginkel, J., Ruigrok, E., & Herber, R. (2019). Assessing soil amplifications in Groningen, the Netherlands. *First Break*, *37*(10), 33–38.

van Ginkel, J., Ruigrok, E., & Herber, R. (2020). Using horizontal-to-vertical spectral ratios to construct shear-wave velocity profiles. *Solid Earth*, *11*(6), 2015–2030.

van Oeveren, H., Valvatne, P., Geurtsen, L., & van Elk, J. (2017). History match of the Groningen field dynamic reservoir model to subsidence data and conventional subsurface data. *Netherlands Journal of Geosciences*, *96*(5), s47–s54.

van Thienen-Visser, K., Pruiksma, J., & Breunese, J. (2015). Compaction and subsidence of the Groningen gas field in the Netherlands. *Proceedings of the International Association of Hydrological Sciences*, *372*, 367–373.

van Thienen-Visser, K., & Fokker, P. A. (2017). The future of subsidence modelling: Compaction and subsidence due to gas depletion of the Groningen gas field in the Netherlands. *Netherlands Journal of Geosciences*, *96*(5), s105–s116.

van Wees, J.-D., Pluymaekers, M., Osinga, S., Fokker, P., van Thienen-Visser, K., Orlic, B., Wassing, B., Hegen, D., & Candela, T. (2019). 3-D mechanical analysis of complex reservoirs: A novel mesh-free approach. *Geophysical Journal International*, *219*(2), 1118–1130.

Vereecken, H., Huisman, J., Bogena, H., Vanderborght, J., Vrugt, J., & Hopmans, J. (2008). On the value of soil moisture measurements in vadose zone hydrology: A review. *Water resources research*, *44*(4).

Voisin, C., Garambois, S., Massey, C., & Brossier, R. (2016). Seismic noise monitoring of the water table in a deep-seated, slow-moving landslide. *Interpretation*, *4*(3), SJ67–SJ76.

Voisin, C., Guzmán, M. A. R., Réfloch, A., Taruselli, M., & Garambois, S. (2017). Groundwater monitoring with passive seismic interferometry. *Journal of Water Resource and Protection*, *9*(12), 1414–1427.

Wang, Q.-Y., Brenguier, F., Campillo, M., Lecointre, A., Takeda, T., & Aoki, Y. (2017). Seasonal crustal seismic velocity changes throughout Japan. *Journal of Geophysical Research: Solid Earth*, *122*(10), 7987–8002.

Wang, Q.-Y., Campillo, M., Brenguier, F., Lecointre, A., Takeda, T., & Hashima, A. (2019). Evidence of changes of seismic properties in the entire crust beneath Japan after the Mw 9.0, 2011 Tohoku-oki earthquake. *Journal of Geophysical Research: Solid Earth*, *124*(8), 8924–8941.

Wang, Q.-Y., Campillo, M., Brenguier, F., Lecointre, A., Takeda, T., & Yoshida, K. (2021). Seismic evidence of fluid migration in northeastern Japan after the 2011 Tohoku-oki earthquake. *Earth and Planetary Science Letters*, *563*, 116894.

Wapenaar, K., Draganov, D., Snieder, R., Campman, X., & Verdel, A. (2010a). Tutorial on seismic interferometry: Part 1 – Basic principles and applications. *Geophysics*, *75*(5), 75A195–75A209.

Wapenaar, K., Slob, E., Snieder, R., & Curtis, A. (2010b). Tutorial on seismic interferometry: Part 2 – Underlying theory and new advances. *Geophysics*, *75*(5), 75A211–75A227.

Wegler, U., Nakahara, H., Sens-Schönfelder, C., Korn, M., & Shiomi, K. (2009). Sudden drop of seismic velocity after the 2004 Mw 6.6 mid-Niigata earthquake, Japan, observed with passive image interferometry. *Journal of Geophysical Research: Solid Earth*, *114*(B6).

Wegler, U., & Sens-Schönfelder, C. (2007). Fault zone monitoring with passive image interferometry. *Geophysical Journal International*, *168*(3), 1029–1033.

Yang, W., Wang, B., Yuan, S., & Ge, H. (2018). Temporal variation of seismic-wave velocity associated with groundwater level observed by a downhole airgun near the Xiaojiang fault zone. *Seismological Research Letters*, *89*(3), 1014–1022.

Yates, A., Savage, M., Jolly, A., Caudron, C., & Hamling, I. (2019). Volcanic, coseismic, and seasonal changes detected at White Island (Whakaari) volcano, New Zealand, using seismic ambient noise. *Geophysical Research Letters*, *46*(1), 99–108.

Zhan, Z., Tsai, V. C., & Clayton, R. W. (2013). Spurious velocity changes caused by temporal variations in ambient noise frequency content. *Geophysical Journal International*, *194*(3), 1574–1581.

Zhou, W., & Paulssen, H. (2017). P and S velocity structure in the Groningen gas reservoir from noise interferometry. *Geophysical Research Letters*, *44*(23), 11–785.

Zhou, W., & Paulssen, H. (2020). Compaction of the Groningen gas reservoir investigated with train noise. *Geophysical Journal International*, *223*(2), 1327–1337.

Zhou, W., & Paulssen, H. (2022). Seismic velocity changes in the Groningen reservoir associated with distant drilling. *Scientific Reports*, *12*(1), 1–9.

Acknowledgements

Although only one name appears on the cover of this thesis, this research would not have been possible without the help, presence and distractions of colleagues, family and friends. I would like to explicitly thank a few people who have helped me undertake this project.

First and foremost, I would like to express my sincere gratitude to my supervisors **Elmer** and **Jeannot** for their guidance and support. **Elmer**, ever since we met in 2016 you have inspired me. Thank you, for encouraging me to envision new research ideas and applications, and for just being there, being a good listener and motivator throughout this journey. Without your invaluable support my research would have been far less successful. Thank you, **Jeannot**, for being there whenever I needed a discussion, your thoughts and advice were consistently spot on. Thank you for editing my written work to boost the level of quality. I particularly love the educational elements you brought into our papers. I feel truly blessed to have had such wise and experienced advisors. I am going to miss working with the both of you, but I hope we can keep collaborating in some way. Practically, that should not be too difficult, since UU and TNO share the same entrance and we run into each other anyway.

Thank you, professors **Andrew Curtis**, **Läslo Evers**, **Laura Socco**, **Jan-Diederik van Wees** and **Ulrich Wegler**, for being part of the dissertation committee and for taking the time to assess this thesis. I am looking forward to the discussion with you at the defence.

Thank you, **Hanneke**, for your reflections on my research ideas, sometimes in a really premature state, and for letting me think out loud. Your thoughts and experience have been really helpful. Thank you, **Rhys**, for a great collaboration and answering all my questions. Without you I still wouldn't understand the basic concept of a sensitivity kernel. Thank you, **Thomas**, for your programming suggestions and insights. You managed to quadruple the computation speed of cross-correlations.

Thank you, **Hen** and **Rûna**, for your support as paranymphs. As you both recently defended your theses, I am really happy to have you on my team. **Hen**, I look forward to future collaborations in TNO projects, and **Rûna**, I wish you all the best with your postdoc in Münster.

I thoroughly enjoyed all the nice coffee moments in my office. I appreciate all colleagues who co-conspired to maintain the prohibited presence of the Nespresso machine in my office as a collective secret. Thank you, **Ashim**, for tolerating the coffee smell in our office throughout the day and for the nice mostly work-unrelated discussions about artificial intelligence, the philosophy of physical measurements, etc. I would like to thank all other PhDs for really fun times at lunches, conferences, courses and summer schools and barbecues: thanks, **Ashim**, **Brechtje**, **David**, **Haorui**, **Hen**, **Janneke**, **Leon**, **Lisanne**, **Rens**, **Rûna**, **Simon**, **Su**,

Thomas and **Wen**. I also appreciate the reflections from different perspectives as exploration geophysics and mantle geophysics and I am grateful for IT support: thanks **Arie**, **Arwen**, **Ivan**, **Laura** and **Theo**.

I appreciate my KNMI colleagues for welcoming me in the RDSA team. Thanks for your support and all the nice discussions. I also very much enjoyed participating in the 'groepsuitjes'. It was a pleasure to be part-time at the KNMI and get to know all of you. I hope that we can continue collaborating in the future. Thanks, **Elmer**, **Läslo**, **Andreas**, **Bernard**, **Brigitta**, **Denise**, **Elske**, **Gert-Jan**, **Gil**, **Janneke**, **Jarek**, **Jelle**, **Jesper**, **João**, **Jordi**, **Kees**, **Luca**, **Madelon**, **Matthijs**, **Olivier**, **Pauline**, **Pieter**, **Reinoud**, **Shahar**, **Simon**, and **Wilma**.

I also want to thank my international friends and colleagues, **Charlotte**, **Luc**, **Marthe**, **Peter**, **Pilar**, **Sabrina**, **Tjeerd**, you made all the conferences, summerschools, etc. so much fun. I hope we will keep meeting and inspiring each other at conferences, and maybe collaborate in the future.

Thanks to the DeepNL community for organizing nice dinners, borrels, a summerschool in Groningen and visits to DeepNL stakeholders. I am especially grateful for the visit to TNO that eventually led to my next adventure in the department of Hydrology and Reservoir Engineering. I enjoyed being part of the Young DeepNL committee and collaborating with **Ajita**, **Aukje**, **Hamed**, **Hamza** and **Samantha**.

Also a great thanks to my parents **Peter** and **Eveline**. This journey would not have been possible without my family's love and support. Thank you, **Peter** for feeding my curiosity since I was very little. When I was a child you already interested me with how the universe works. I really enjoyed making waves interfere during our holidays, but also the discussions that now have reached another level. Let's soon write that Fokker & Fokker paper about a yet to be determined topic!

Last, I would like to express my deepest gratitude to my wife **Janine**. Thank you for listening to all the tiring meticulous details of my research. Thank you for distracting me, providing perspective, and adding nuance. You and our daughter **Mila** bring me more happiness than research or science ever could. Thanks for being my rock and making my life so much brighter!

Curriculum Vitæ

Eldert Fokker

20-11-1994	Born in Nieuwegein, the Netherlands.

Working Experience

2023–present	Geoscientist TNO Geological Survey of the Netherlands, Utrecht, the Netherlands
2019–2023	Doctoral Candidate Utrecht University, Utrecht, the Netherlands in close collaboration with KNMI, De Bilt, the Netherlands
2015–2017	Teaching Assistant Utrecht University, Utrecht, the Netherlands
2012–2019	Piano Teacher Self-employed, Houten, the Netherlands

Education

2019–2023	Ph.D. in Geophysics Utrecht University, the Netherlands
2017–2019	M.Sc. in Earth Structure and Dynamics Utrecht University, the Netherlands
2014–2017	B.Sc. in Physics and Astronomy Utrecht University, the Netherlands
2013–2017	B.Sc. in Earth Sciences Utrecht University, the Netherlands

Internships

2018–2019	M.Sc. Research Earth Structure and Dynamics TNO Geological Survey of the Netherlands, Utrecht, the Netherlands	
2016	Joint B.Sc. Research Earth Sciences and Physics and Astronomy KNMI, De Bilt, the Netherlands	

Scientific award

2022	Outstanding Student Presentation Award AGU Fall Meeting 2022	Chicago, US

Supervision

2022	B.Sc. Research Imme Wienk *Monitoring seismic velocity changes using passive image interferometry in the subsurface of Almelo*

Professional development

2023-04	EGU: General assembly 2023	Vienna, AT
2023-03	Nederlands aardwetenschappelijk congres 2023	Utrecht, NL
2022-12	AGU: Fall meeting 2022	Chicago, US
2022-11	First EAGE/SBGf workshop on reservoir monitoring and its role in the energy transition	Rio de Janeiro, BR
2022-09	Nederlands aardwetenschappelijk congres 2022	Utrecht, NL
2022-08	DeepNL summer school	Groningen, NL
2022-05	EGU: General assembly 2022	Online
2022-05	SPIN workshop 2: Time-dependent behaviour of earth's materials	Carcans, FR
2022-04	Passive imaging and monitoring in wave physics	Cargèse, FR
2021-12	AGU: Fall meeting 2021	Online
2021-11	First annual meeting of the Dutch inverse problems community	Lunteren, NL
2021-10	Presenting with impact	Utrecht, NL
2021-04	EGU: General assembly 2021	Online
2021-04	Nederlands aardwetenschappelijk congres 2021	Online
2020-10	Research writing for scientists	Online
2020-07	DeepNL webinar series on induced seismicity	Online
2020-03	Nederlands aardwetenschappelijk congres 2020	Utrecht, NL
2020-02	Winter school: Inverse problems in geophysics	Sudelfeld, DE
2019-10	Advanced geophysical imaging in complex media	Delft, NL

List of Publications

Journal articles

5. Fokker, E., Ruigrok, E., & Trampert, J. (in preparation). Monitoring anthropogenic fluctuations in reservoir pressure using surface-wave phase-velocity variations: A feasibility study. *In preparation for submission to Geophysical Prospecting.*

4. Fokker, E., Ruigrok, E., & Trampert, J. (2024). On the temperature sensitivity of near-surface seismic wave speeds: Application to the Groningen region, the Netherlands. *Geophysical Journal International*, *in press.*

3. Fokker, E., Ruigrok, E., Hawkins, R., & Trampert, J. (2023). 4D physics-based pore pressure monitoring using passive image interferometry. *Geophysical Research Letters*, *50*(5).

2. Fokker, E., Ruigrok, E., Hawkins, R., & Trampert, J. (2021). Physics-based relationship for pore pressure and vertical stress monitoring using seismic velocity variations. *Remote Sensing*, *13*(14), 2684.

1. Fokker, E. B., & Ruigrok, E. N. (2019). Quality parameters for passive image interferometry tested at the Groningen network. *Geophysical Journal International*, *218*(2), 1367–1378.

Extended abstracts

1. Fokker, E., Ruigrok, E., Hawkins, R., & Trampert, J. (2022). Pore pressure monitoring in a chalk gas reservoir using surface-wave velocity variations. *1st EAGE/SBGf Workshop on Reservoir Monitoring and its Role in the Energy Transition*, *2022*(1), 1–5.

Popularising articles

1. Fokker, E. (2023). Grondwatermetingen met seismische achtergrondruis. *KNMI webpage*.

Invited talks

1. Fokker, E. (2023-03). Pore pressure monitoring in a chalk gas reservoir. *Nederlands Aardwetenschappelijk Congres 2023*. Utrecht, the Netherlands.

Conference contributions

11. Fokker, E., Ruigrok, E., & Trampert, J. (2024-04). Do earthquakes cause more damage in the summer? *EGU General Assembly 2024*. Vienna, Austria.

10. Zaadnoordijk, W.J., & Fokker, E. (2024-04). Data driven assessment of quantitative status of groundwater in the Netherlands *EGU General Assembly 2024*. Vienna, Austria.

9. Fokker, E., Ruigrok, E., & Trampert, J. (2023-04). Temperature-induced disturbances of the stress-strain equilibrium and their effects on seismic velocities. *EGU General Assembly 2023*. Vienna, Austria.

8. Fokker, E., Ruigrok, E., & Trampert, J. (2023-03). Can subsurface temperature variations be derived from time-lapse seismic velocity measurements? *Nederlands Aardwetenschappelijk Congres 2023*. Utrecht, the Netherlands.

7. Fokker, E., Ruigrok, E., Hawkins, R., & Trampert, J. (2022-12). Monitoring tool for 4D hydrological pore pressure variation. *AGU Fall Meeting 2022*. Chicago, United States of America.

6. Fokker, E., Ruigrok, E., Hawkins, R., & Trampert, J. (2022-09). From seismic ambient noise to 4D pore pressure monitoring. *Nederlands Aardwetenschappelijk Congres 2022*. Utrecht, the Netherlands.

5. Fokker, E., Ruigrok, E., Hawkins, R., & Trampert, J. (2022-05). 4D physics-based pore pressure monitoring in the shallow subsurface of Groningen, the Netherlands. *EGU General Assembly 2022*. Online.

4. Fokker, E., Ruigrok, E., Hawkins, R., & Trampert, J. (2021-12). Spatial variation in seismic velocity change in the shallow subsurface of Groningen, the Netherlands. *AGU Fall Meeting 2021*. Online.

3. Fokker, E., Ruigrok, E., Hawkins, R., & Trampert, J. (2021-04). Physics-based model relating seismic velocity variation to groundwater and pore pressure fluctuation. *EGU General Assembly 2021*. Online.

2. Fokker, E., Ruigrok, E., Hawkins, R., & Trampert, J. (2021-04). Physics-based model relating seismic velocity variation to groundwater and pore pressure fluctuation. *Nederlands Aardwetenschappelijk Congres 2021*. Online.

1. Fokker, E., Ruigrok, E. & Trampert, J. (2020-03). Seismic time-lapse velocity variations in the Groningen subsurface. *Nederlands Aardwetenschappelijk Congres 2020*. Utrecht, the Netherlands.